5-22-2015 12:00 AM

Design and Fabrication of a Multifunctional Nano-on-micro Delivery System

Alexandra D. Bannerman
The University of Western Ontario

Supervisor
Dr. Wankei Wan
The University of Western Ontario

Graduate Program in Biomedical Engineering
A thesis submitted in partial fulfillment of the requirements for the degree in Master of Engineering Science

DESIGN AND FABRICATION OF A MULTIFUNCTIONAL NANO-ON-MICRO DELIVERY SYSTEM

(Thesis Format: Integrated article)

by

A. Dawn Bannerman

Graduate Program
In
Biomedical Engineering

A thesis submitted in partial fulfillment
of the requirements for the degree of
Master of Engineering Science

School of Graduate and Postdoctoral Studies
The University of Western Ontario
London, Ontario, Canada

ABSTRACT

The treatment of tumours using microbeads for embolization and drug delivery is a widely used, but often ineffective, technique. In this work, we aim to produce microbeads for this application with four main improvements: visibility, targetability, degradability, and an alternative route for drug loading. We accomplish this through the fabrication of ~100μm diameter microbeads composed of poly(vinyl alcohol) (PVA), iron oxide nanoparticles, and cellulose nanocrystals (CNC) using a custom-designed microchannel system. Characterization demonstrated that microbeads were magnetic, as well as visible under clinical CT. Separately, the dissolution of PVA iron oxide hydrogels exposed to different environmental conditions was studied. Iron release and mass loss was demonstrated, and the weakening of material was confirmed using mechanical testing. This shows the potential for microbeads composed of this material to 'degrade' over time. PVA iron oxide CNC microbeads are promising as a multifunctional visualization and delivery system.

Keywords

Multifunctional delivery system, microbeads, trans-arterial chemoembolization, localized delivery, computed tomography, microfluidics, poly(vinyl alcohol), iron oxide nanoparticles, cellulose nanocrystals, degradable hydrogel

ACKNOWLEDGEMENTS

This work has been possible with the help of many important people. I would like to start with sincere thanks to my supervisor, Dr. Wankei Wan. Without his guidance, support, and extensive experience and knowledge, this work would not have been accomplished. He dedicated significant time and energy in helping, challenging and encouraging me, not only on this project but also in many other aspects of my experience during this degree.

I would like to acknowledge all of the members of my lab and Western's Biomedical Engineering graduate program for providing a stimulating and friendly work environment. I would like to specifically recognize those who helped me with this project. Thank you to Jian Liu, who was instrumental in the fabrication of the microchannel device system, and Solmaz Karamdoust, who provided samples and assistance with the work involving cellulose. I would like to thank Justin Cook for advice at the early stages of this work, and Itai Malkin and Melessa Salem who contributed to the later stages. Thank you also to Helium Mak and Asha Parekh who provided guidance and assistance with the mechanical testing work.

I would like to extend my gratitude to my advisors, Dr. Elizabeth Gillies and Dr. Lisa Hoffman for their suggestions and advice. The work involving CT would not have been possible without Dr. Hoffman and her student, Andrew Bondoc, and I thank them for their kind help with this portion of the project.

Finally, I would like to acknowledge the support of my sisters, Heather and Jackie Bannerman, my friend and roommate, Emma Hobbs, my boyfriend, Nico Muñoz, and above all, my parents, Laurie Spence Bannerman and John Bannerman. I am so grateful for their love and encouragement.

TABLE OF CONTENTS

LIST OF FIGURES

LIST OF TABLES

LIST OF ABBREVIATIONS

Name	Abbreviation
2-acrylamido-2-methylpropanesulphonate sodium	AMPS
2,2,6,6-tetramethylpiperidine-1-oxyl	TEMPO
bacterial cellulose	BC
bovine serum albumin	BSA
cellulose nanocrystals	CNC
computed tomography	CT
computed tomography angiography	CTA
doxorubicin	Dox
drug-eluting bead	DEB
energy dispersive X-ray spectroscopy	EDX
ethylenediaminetetraacetic acid disodium salt	EDTA
iron (II) chloride tetrahydrate	$FeCl_2 \bullet 4H_2O$
iron (III) chloride	$FeCl_3$
iron oxide (magnetite)	Fe_3O_4
freeze-thaw	FT
freeze-thaw cycle	FTC
water	H_2O
hepatocellular carcinoma	HCC
hydrochloric acid	HCl
International Centre for Diffraction Data	ICCD
low temperature thermal cycling	LTTC
level	L
molecular weight	MW
magnetic resonance imaging	MRI
sodium hydroxide	NaOH
poly(dimethyldisiloxane)	PDMS
poly($_{D,L}$-lactic-co-glycolic acid)	PLGA
poly(methyl methacrylate)	PMMA
poly(vinyl alcohol)	PVA
scanning electron microscopy	SEM
transarterial chemoembolization	TACE
transmission electron microscopy	TEM
window width	W
X-ray diffraction	XRD

CHAPTER 1 – Overview and Objectives

1.1 Overview

The development of multifunctional drug delivery systems addresses many of the issues associated with current approaches to cancer treatment, such as the toxic and unspecific nature of chemotherapy. Microbeads are widely used as a drug-eluting embolization material in the treatment of hepatocellular carcinoma. However, there are specific areas of improvement that are needed. Namely, microbeads that can be visualized with the use of clinical imaging techniques, degraded following therapeutic use, and be better targeted to a specific location are extremely desirable. They must also have the ability to load and release drug molecules in a favourable way.

To achieve these goals, we investigate the production and use of a multifunctional system composed of a poly(vinyl alcohol) (PVA) matrix loaded with iron oxide nanoparticles and cellulose nanocystals (CNC). The iron oxide nanoparticles, which are biocompatible, non-toxic, and have magnetic properties, act as a contrast enhancement agent that allows visualization as well as magnetic targeting. Additionally, the incorporation of iron oxide changes the properties of a PVA hydrogel to allow for subsequent dissolution of the material. CNC, which are also biocompatible, can provide a high surface area for drug loading within the microbeads.

The first section of this thesis describes the design of a system for production of these microbeads, as well as bead fabrication. Microbeads are characterized in terms of size, structure and morphology, iron oxide presence in the form of magnetite, and iron oxide nanoparticle distribution. They are also imaged under computed tomography (CT) to demonstrate their visibility.

The second part of this work relates to the dissolution of this material. PVA is a biocompatible and biostable polymer that can be physically crosslinked, using a low temperature thermal cycling process (LTTC), to form nondegradable hydrogels, useful

in many biomedical applications. In addition to physical crosslinking, iron oxide nanoparticles have been shown to provide a certain level of crosslinking in PVA. We investigate the use of iron oxide as a crosslinking agent in conjugation with the LTTC process to form a dissolvable PVA hydrogel.

The focus of this work involves the production of multifunctional microbeads with many advantageous properties that make them a desirable candidate for use in cancer treatment. Through the production and investigation of PVA iron oxide CNC microbeads, we will demonstrate their unique and multifunctional properties, and the study of the PVA iron oxide hydrogel will explore the dissolution properties of this advantageous biomaterial.

1.2 Objectives

1. To develop a method of production for PVA iron oxide CNC microbeads of an appropriate size and successfully demonstrate their fabrication.
2. To characterize the microbeads and examine them under clinical imaging techniques to demonstrate visualization.
3. To study the use of iron oxide incorporation as well as the LTTC process to crosslink PVA hydrogels and study their dissolution as a function of changing environmental conditions.

CHAPTER 2 – Literature Review

2.1 Cancer and Hepatocellular Carcinoma

Worldwide each year, there are an estimated 12.7 million new cases of cancer and 7.6 million cancer deaths [1]. Even though there are numerous treatment options, more than 50 percent of patients eventually die from progressive metastasis because they either do not respond to therapy or they relapse afterward [2].

Specifically, primary liver cancer is the fifth most commonly diagnosed type of cancer in men and the seventh most common in women worldwide. In terms of deaths caused by cancer, liver cancer ranks second in men and sixth in women. In 2008, an estimated 748,300 new liver cancer cases were diagnosed worldwide. Hepatocellular carcinoma (HCC), a primary malignancy of the liver, makes up 70% to 85% of total global liver cancers [3]. The main contributors of HCC are the hepatitis B virus infection, hepatitis C virus infection, alcohol-related cirrhosis and possibly nonalcoholic fatty liver disease. In many parts of the world, incidence rates of liver cancer are increasing. In some developed regions, this could possibly be a result of the obesity epidemic and rise in hepatitis C virus infection [4-6].

2.2 Current Treatment Methods and Products

Treatment of HCC can be either curative or palliative. Curative treatment, which results in complete responses in a large percentage of patients, includes resection, liver transplantation, and percutaneous treatments such as ethanol injection, cryoablation or radiofrequency ablation. However, less than one third of patients, are eligible for these treatments [7] based on factors including the stage of the underlying disease, the cancer progression and the liver functional status [2,8]. The next options, for intermediate HCC, include chemotherapy, embolization, or a combination of the two – chemoembolization. The best candidates for chemoembolization are patients with preserved liver function and asymptomatic multinodular tumours that have not spread into vessels or outside of the liver [7,8].

Trans-arterial chemoembolization (TACE) is a technique that has been used clinically for over 30 years [9] as a loco-regional treatment, which is essentially the physical targeting of therapeutics to a particular site (eg. drug infusion into the organ bearing the tumour). TACE (Figure 2.1) is a minimally invasive procedure, performed by interventional radiologists, in which chemotherapy, followed by an embolization agent, is infused as close to the tumour site as possible, through a catheter. This is done by feeding a catheter through the femoral artery, into the hepatic artery and then to specific branches in attempt to limit delivery to tumour tissue. Gelfoam in 1mm cube preparations is a commonly used embolization agent, but poly(vinyl alcohol), alcohol, starch microspheres, metallic coils, or autologous blood clots have also been used [8,10-14]. Typically, Lipiodol®, an oily, radio-opaque contrast agent, is injected along with the chemotherapeutic agent [8].

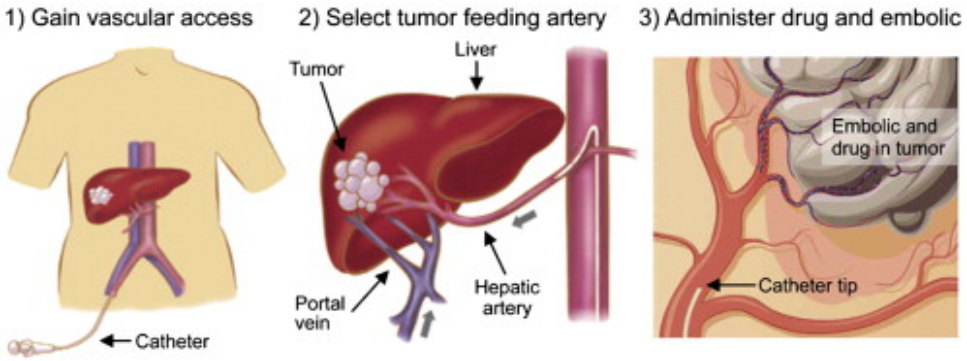

Figure 2.1 Schematic describing the principles of TACE. Access is gained in the femoral artery (left) and a hepatic artery is selected by use of a guidewire and a catheter (middle). A micro-catheter is then often positioned in a tumour feeding artery (right). From this location, TACE is performed by infusing a mixture of chemotherapeutics and embolic agents (right). Reprinted from [15] with permission. Copyright (2012) Elsevier

Because HCC is a primary liver cancer, TACE therapy is an appropriate treatment approach. Alternatively, metastatic liver cancer can occur, which results from metastasis of a primary tumour in another location in the body. Due to the differences in the vasculature of these two types, and the need for a more systemic treatment approach for metastatic cancers, treatment with TACE is typically used for primary

cancers [2]. Blood supply to the liver is provided by the hepatic artery (25%) and the portal vein (75%). Most liver tumours receive blood principally from the hepatic artery [2]. Therefore, for intermediate HCC tumours, prevention or limitation of blood flow through the hepatic artery to the tumour is a logical means of causing ischemia, which leads to tumour necrosis.

Chemotherapy is known to have very harmful side effects for patients due to the high toxicity of the drugs administered. Systemic delivery of these therapeutic agents results in the unwanted killing of non-cancerous tissue. Furthermore, rapid clearance of the drug molecules is an issue, and to overcome this, multiple doses of these toxic agents are required in order for the desired effect to take place on the tumour. Even loco-regional treatment, where the drug is infused directly into the organ containing the tumour, does not solve these problems. Controlled delivery devices offer a solution. Liposomes, hydrogels, polymer-based disks, rods, pellets and micro or nanoparticles are all systems that are used to encapsulate therapeutic agents and provide sustained release [16]. Drug-encapsulating polymer microspheres is one category of drug delivery system that has been studied extensively to release therapeutic agents in a controlled rate over a longer period of time compared to conventional approaches. Moreover, the ability to tune loading and release rates allows for better control and tailoring to a specific application. Additionally, drugs that are otherwise rapidly cleared by the body can be administered in fewer doses. The benefits provided by controlled delivery devices often result in an increase in patient comfort and compliance [16]. Polymer microspheres are a good option because they can be biocompatible, provide high bioavailability, and sustain release over a long period of time. However, disadvantages for polymeric microspheres include the difficulty of large-scale manufacturing, maintaining the stability of drug molecules, and difficulty in controlling the rates of drug release [16].

More specifically, hydrogels are a subcategory of polymers that possess properties that are highly advantageous for drug delivery purposes. Hydrogels are crosslinked polymer networks with high water content. They are highly porous, which allows drugs to diffuse into the structure during loading, and out during release. Furthermore, hydrogel

porosity can be controlled by altering the density of crosslinks in the matrix [17]. Finally, they are typically biocompatible due to their high water content and similarity of their chemical composition and mechanical properties to that of native extracellular matrix [17]. Advancements have been made toward the development of stimuli-responsive or "smart" hydrogels, which incorporate a triggering mechanism for drug release such as pH, temperature, pressure, electric field, chemicals, or ionic strength [18].

Doxorubicin (Dox) is one of the most common drugs used to treat cancer [19]. It is a useful therapeutic for HCC treatment and its cytotoxicity is a result of several mechanisms including intercalation in DNA leading to inhibition of DNA replication or RNA transcription, DNA damage or lipid peroxidation, disruption of DNA unwinding, strand separation or helicase activity, and topoisomerase II inhibition leading to apoptosis. Its high toxicity has actually hindered its effectiveness as a treatment option [20]. Negative effects of Dox include cardiotoxicity, nephrotoxicity, myelosuppresion, multiple drug resistance, nausea, vomiting, stomatitis, alopecia, vesicant reaction, radiation recall, and transient memory loss [20]. Many strategies have been explored to encapsulate Dox in a carrier. Some strategies include encapsulation of Dox within liposomes [19,21], polymeric micelles [22-24] and nanoparticles [25,26]. Commercialized products include Doxil®, a PEGylated (stealth) Dox liposome; Myocet®, a non-PEGylated liposomal Dox formulation; and the DC Bead®.

The DC Bead, the first commercially available embolic drug-eluting bead (DEB), was launched in 2004 in Europe by a company called Biocompatibles. The beads are made of poly(vinyl alcohol), modified with *N*-acryloyl-amino-acetaldehyde dimethylacetal and crosslinked with 2-acrylamido-2-methylpropanesulphonate sodium (AMPS) salt forming a spherical bead [2,27]. They are fabricated using an inverse suspension polymerization technique to produce beads in the range of 100 to 900μm in diameter [28], and are composed of ~95% water within the network of polymer chains. The sulphonic acid groups present on the AMPS chains allow for conjugation of drug molecules through ion exchange. In order for this to occur, the beads are suspended in solution containing the desired drug molecule. The DC bead is free of drug when given

to the physician, and is subsequently submerged in a solution containing the drug, like doxorubicin hydrochloride, for several hours. The positively charged Dox in solution is able to diffuse into the polymer network and displaces sodium ions bonded to the SO_3^- groups, with a drug uptake over 99% providing there are no additional ions competing for ion exchange. The maximum doxorubicin loading is 37.5mg/mL of beads. The doxorubicin drug-eluting bead is called DEBDOX™, with an alternative being DEBIRI™, containing Irinotecan, another anticaner drug [2].

DEBs have been shown to be effective in accomplishing tumour necrosis while reducing systemic chemotherapeutic levels. The release of doxorubicin from DEBs in DEB-TACE therapy compared to conventional TACE shows a dramatic decrease in the initial serum doxorubicin levels (Figure 2.2). This suggests that the amount of chemotherapeutic could be increased to tumour tissue while also reducing toxicity compared to conventional TACE [29].

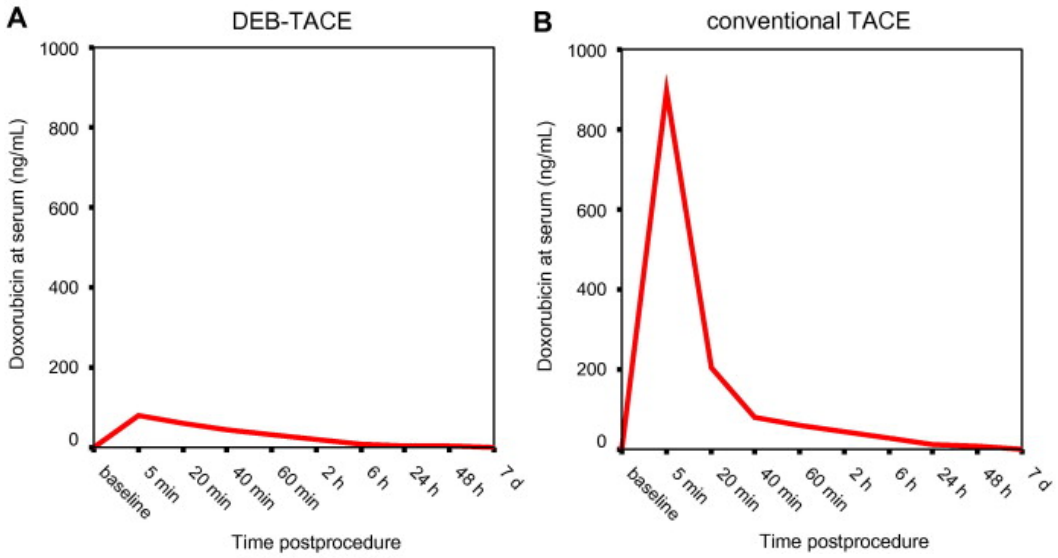

Figure 2.2 Dox serum levels of DEB-TACE and conventional TACE. Measurements of serum doxorubicin levels at different time points in DEB-TACE patients (A), and in the conventional TACE group (B). Reprinted from [29] with permission. Copyright (2007) Elsevier

DEBs are typically used in volumes of 1-4mL to provide therapeutic levels of drug to the site [2]. Recommendations for the use of DEBDOX include a loading dose of 25mg

Dox/mL beads usually with a locally administered dose of 100mg Dox (lower than recommended maximum of 150mg Dox for a given procedure) [27]. Other recommendations suggest that a total loading of 50-75mg doxorubicin in 2mL (25-37.5mg Dox/mL beads) is optimal [30]. A review of recent clinical results concluded that the optimal available bead size is the 100-300μm range as this size results in less complete stasis, which allows for repeat treatment, providing the potential for a greater cumulative dose. This small bead size resulted in fewer and less severe adverse event rates [31]. Dreher *et al.* found that even smaller DEBs (70-150μm versus 100-300μm) were able to penetrate further into the target tissue and had greater spatial frequency or density [32]. Lee *et al.* also found that the smaller diameter beads in their study (100-300μm versus 300-500μm) were able to reach the tumour, or get in close proximity to it, more effectively [33]. However, there is a limit to how small the beads can be. Particles greater than 10μm must be used as small capillary diameter is around 5-8μm [34]. Furthermore, work completed on embolization in rat models reported that particles of at least 40μm are required for embolization to prevent distribution to other organs such as the spleen or lung [35].

2.3 Necessary improvements to current approaches

As was described in a review by Kerr [36], the ideal drug delivery and embolic system for regional treatment of cancer should be deliverable by catheter, appropriate size for embolization of target vessels, biocompatible and non-immunogenic, have no drug-device incompatibility issues, carry a therapeutic dose of a drug, and provide controlled, local release in therapeutic levels [2]. These goals have been reasonably achieved with the currently administered DEBs. However, there are still many ways that this therapy can be improved.

A recent review by Lewis and Dreher discussed loco-regional drug delivery using image-guided intra-arterial drug-eluting beads. They presented some drawbacks to the currently available procedures and products and suggested the future directions for DEB-TACE. Some of these presented suggestions include the need for imageable

DEB-TACE, the tailoring of bead size to the arterial anatomy of the tumour, the development of degradable DEBs, and the use of DEB combination therapy [15].

Multifunctional systems, in which two or more materials are incorporated into one system, have certainly been noted as a beneficial system for cancer therapy because of the ability to accomplish multiple goals at once. Multifunctional materials are composite materials that either perform multiple structural functions, or combine non-structural and structural functions [37]. Polymer coated magnetic nanoparticles containing fluorescent molecules, tumour-targeting moieties, and chemotherapeutic agents have been developed and are able to target specific sites, provide imaging contrast enhancement, and treat the tumour simultaneously [38]. By adding additional material components that possess unique properties, it could be possible to enhance the functionality of DEBs. In the following paragraphs, we introduce some aspects that would be beneficial as added components for drug-eluting beads used for TACE therapy.

2.3.1 Visibility/ detectability

The current method of tracking the location of drug-eluting beads for TACE therapy involves infusing a soluble iodinated non-ionic contrast agent, such as the commonly used CT contrast agent Lipodiol made from iodinated poppy seed oil, with the drug-eluting embolization beads. This is done either by injecting beads followed by contrast agent [39], or mixing the contrast media with the microbead suspension and injecting them at once [40]. Unless another specific endpoint is desired, once reflux is detected, that is used as the endpoint for bead infusion [30]. The issues with this are that contrast media is rapidly cleared by the body [41], meaning that long-term detection of the beads is not possible. Also, loosely mixed contrast media does not necessarily demonstrate the presence or location of microbeads [42], and additionally, once the blood flow is limited due to embolization, it may be difficult for more contrast agent to reach the site. This lack of intraprocedural imaging feedback has been identified as a disadvantage of DEB-TACE compared to Lipiodol-based TACE [15,32]. A drug-eluting bead with inherent radiopaque or magnetic properties would be beneficial in

that it would have the ability to be imaged using clinical imaging techniques. This could be accomplished during the procedure, providing real-time intra-procedural feedback, as well as providing useful information in follow-up imaging.

A new class of embolic microspheres that are detectable through imaging has been recently introduced. It has been noted that the ability to image the distribution of DEBs in tissue in real-time would be useful for choosing particle size to further improve embolization procedures [33], to help adjust the procedure to specific patients, or to provide information for combination therapy such as the optimal position for ablation needles based on areas less concentrated with drug or beads [32]. Additionally, imaging the final location of DEBs would provide some information in terms of drug quantification and localization [32] of the dynamic drug levels in a tumour following DEB-TACE [43]. Namur *et al.* found that drug distribution after DEB-TACE was greatest around the beads and existed at 600μm away from the bead edge [44].

Detectable embolic particles that have recently been studied include modified commercial products such as Embozene® Microspheres with barium sulfate and iron oxide precipitated into the hydrogel for radiography, CT and magnetic resonance imaging (MRI) in porcine kidneys [45]; iron oxide-containing Embosphere® Microspheres made of tris-acryl gelatin for use with MRI [33]; Contour® Emboli PVA particles modified with gadolinium chelates to the surface for MR imaging [46]; and the LC Bead® (similar to the DC bead but without loaded drug) loaded with Lipiodol visualized with fluoroscopy and CT [40]. Additionally, chitosan microspheres embedded with superparamagnetic iron oxide have been developed for MRI traceable embolization [47,48].

Lee *et al.* imaged the distribution of iron-oxide containing tris-acryl gelatin microspheres after using MR imaging following injection into rabbit liver. Results displayed a difference in distribution and location of small embolization microspheres compared to larger ones, with the larger ones being undesirably located outside the tumour area. This suggests that detectable embolic microspheres could provide useful information that would help improve TACE therapy technique [33]. Sharma *et al.*

demonstrated that Lipiodol loaded LC beads could be detected *in vivo* in swine liver and kidney tissue with CT. The visibility was based on the iodine content of the Lipiodol-loaded microspheres, the distribution volume after embolization, and the imaging method and post-processing image analysis sensitivities. They showed that individual beads could be resolved using micro-CT but not clinical CT, and suggested that if at least 2-3 beads were packed in an artery, optimal visibility with clinical CT could be achieved. Approximately 0.2-0.25mL of beads could be detected with CT and approximately 0.4-0.5mL could be detected with fluoroscopy in the final arterial destination after embolization of the liver and kidney [40].

Following this work, Dreher *et al.* studied the doxorubicin levels around radiopaque DEBs. The LC/DC Beads, made radiopaque by the addition of Lipiodol into the bead, were also loaded with Dox and the beads were delivered to normal swine liver and kidney and were imaged *in vivo* with fluoroscopy and CT. It was observed that smaller beads (70-150μm compared to 100-300μm in diameter) penetrated the tissue more distally, with a more homogeneous distribution, and roughly 2-fold greater drug coverage. They also found that transcatheter computed tomography angiography (CTA) with liquid iodinated contrast shows different results than the eventual bead location using radiopaque beads, demonstrating that using transcatheter CTA with liquid contrast is not accurate in approximating the eventual bead location, and radiopaque beads would better determine this [32].

The development of multimodal embolization particles has also been recognized as a desirable goal because it would allow procedural imaging to be achieved using multiple clinical imaging techniques. Embolization particles of 40 to 200μm consisting of a long polymer with an iodine-containing core and an iron oxide coating were shown to be visible under fluoroscopy, CT, and MRI [42]. It is suggested that the combination of multiple modalities could provide the quantifiability of CT along with the sensitivity of MRI [49], and could be useful for not only intraprocedural imaging, but also follow-up examinations [42].

It is recommended that follow-up CT or MRI be completed two to four weeks following treatment with DEBs to monitor tumour response. If residual tumour is detected, further treatment is recommended and typically occurs four to eight weeks after the original treatment [30]. This indicates that detection of visible DEBs would be easy to incorporate into current practice and could provide beneficial information as to the amount and location of existing DEBs.

2.3.2 Degradability

The fate of many DEBs following therapy is currently unknown. When the loaded chemotherapeutic has been delivered, and treatment is not finished or the tumour recurs, further DEB-TACE is often needed. According to Lewis and Dreher, "the current materials are considered non-biodegradable which led to early objections to DEB therapy since it may not be possible to re-enter the feeding artery once this artery had been occluded" [15]. Multiple treatments are often needed [31] and a review of studies of HCC transarterial therapy found that the average number of sessions per patient was 2.5 ± 1.5 occurring 2 months apart [9]. It has been thought that non-biodegradable microparticles for TACE therapy should be used for single therapies and biodegradable versions should be used when repeated therapy is needed so ensure that the artery is not blocked [35]. In spite of this, non-biodegradable DEBs have been used clinically and multiple repeat DEB-TACE procedures in the same patient has been shown possible [50]. This does not, however, mean that there are no issues with the accumulation of DEBs at the tumour site without the ability to degrade, but that there is currently no option that properly addresses this. "There is an undercurrent of opinion that DEB evolution will eventually move in this biodegradable direction as an essential feature" [15].

Degradability of the carrier is an important aspect to consider for drug delivery. Polymeric microspheres composed of biodegradable material are one of the most commonly used drug delivery systems [16]. In terms of microspheres for drug delivery, the degradability is not only important because it limits accumulation and potentially toxic side effects, but it also alters the release of the drug molecules incorporated or

encapsulated within the microsphere. Release from a degradable polymer can follow any of the following mechanisms: release from the surface of the microsphere; release through the pores of the microsphere; diffusion through the polymer barrier; diffusion through a water swollen barrier; and release due to polymer erosion and bulk degradation [51]. The two main categories of polymer degradation are surface erosion and bulk erosion [52,53]. Drug carrier erosion may be beneficial because it may allow for release of drug molecules entrapped in the polymer matrix, resulting in additional or prolonged release, and also opens up the potential for delivery of more challenging drug molecules; this includes water-insoluble drugs, which cannot otherwise diffuse from a DEB, or molecules of high molecular weight [35].

Biodegradable polymers can be natural or synthetic, and break down either enzymatically or non-enzymatically into biocompatible, non-toxic byproducts [51]. Non-enzymatic degradation or dissolution can occur hydrolytically, or through change in environmental factors such as pH, temperature, or electric field [17]. Synthetic biodegradable polymers include polyorthoesters, polyanhydrides, polyamides, polyesters, polyphosphazenes, and natural polymers used for biodegradable drug delivery include proteins such as albumin, gelatin, and collagen, or polysaccharides such as starch, cellulose, and chitosan [51].

Poly(vinyl alcohol) is known to be non-biodegradable. (This will be discussed further in section 2.5.1). In a review on agents and drugs used for TACE therapy of HCC, Giunchedi *et al.* described the PVA microspheres, and specifically the DC bead, as belonging to the non-biodegradable category [35]. In terms of the DC bead, it has been reported that small beads may be favourable due to less complete stasis, allowing for repeat treatment [31]. Additionally, obstruction of tumour arteries could prevent contrast agent perfusion into the tumour, which may inhibit follow-up imaging to detect viable tumour [29]. It is reasonable to conclude that degradable DEBs would be beneficial because they would allow more effective repeat treatment and also better monitoring of tumour progression.

2.3.3 Targetability

Targeting of drug carriers has been identified as an important area of cancer therapy and localizing therapeutic agents to a specific area remains a constant challenge of chemotherapy. Because most chemotherapeutic agents affect any rapidly dividing cell, the unspecific nature can cause significant harm to surrounding tissue. In the case of intravenous administration, the drug circulates throughout the body. By directing drug carriers to a target organ, delivery has the potential to better treat the tumour tissue through the release of the full drug load to the specific site, as well as limiting toxicity to other organs or surrounding tissue. Targeting can either be active or passive. In terms of microsphere encapsulation of drug molecules, active targeting involves molecular interactions between microsphere surface groups and specific receptors on the cells of the target tissue. Alternatively, passive targeting occurs based on physical or chemical properties of the microsphere, for example size or charge [16]. Loco-regional treatment, as mentioned previously, is accomplished with DEBs by the physical localizing of drug carriers in close proximity to the target tumour tissue, and size dependent microbead accumulation in the vessels of the tumour. This is a form of passive targeting that relies on blood flow to carry microbeads to a general location.

An alternative method of passive targeting is magnetic targeting. Magnetic targeting of magnetically responsive particles carrying anticancer agents is a method of selectively localizing drug molecules. This approach has been studied since the 1970s with recent development of drug loaded ferrogels [54] and magnetic nanoparticles conjugated with drug molecules [55-57]. Substantial advancements have been made in this area because of the potential to focus drug carriers to very specific locations. This could be achieved by dynamically manipulating magnets to focus the magnetic drug carriers [58].

It has been suggested that magnetic carriers could be used to improve TACE therapy [35]. Pouponneau *et al.* described the need for better targeting of TACE therapy particles and four main problems associated with the lack of it: some drug reaches systemic circulation causing undesirable cytotoxicity; the drug can attack healthy cells; a painful procedure is experienced due to embolization of healthy blood vessels; and

damage to the hepatic artery occurs, limiting the ability to effectively perform additional treatments. The authors fabricated magnetic iron-cobalt nanoparticles encapsulated into poly($_{D,L}$-lactic-*co*-glycolic acid) (PLGA) microparticles that could be magnetically steered by an MRI system [59]. An additional method of targeting or localizing the DEBs used in TACE therapy could be beneficial in accumulating the microbeads at a more specific region within the liver.

2.3.4 Improved drug loading and release

It has been suggested that DEBs can pose a problem when there is incomplete killing of tumour tissue in combination with hypoxic conditions. This could cause cancerous cells to transform into a more malignant phenotype [15]. Work demonstrating that embolization-induced hypoxia actually leads to the expression of vascular endothelial growth factor and angiogenesis [60] supports the idea that additional therapeutics that block angiogenic pathways could be administered along with current therapeutics for DEB-TACE [15]. Combination therapy with other anti-cancer agents is also being studied and the ability to load multiple drugs into DEBs may prove beneficial [15].

Moreover, through the ion exchange drug conjugation currently used in some DEBs, a limit of drug loading exists. If the loading of the drug molecules into the microbeads can be enhanced, and the mechanism of drug release altered and tuned, the release can be sustained over a longer period of time. This would be beneficial in providing longer treatment without an increase in toxicity or the need for multiple doses of drug loaded embolic agents. Additionally, there are constraints on the types of drugs that can be loaded into the current DEBs that load and release drug based on ion exchange. Chief among these constraints is that the drug molecule must be ionizable [35].

A material that has the ability to increase drug loading and also enable the loading of multiple therapeutics could prove to be very advantageous for this type of system. In section 2.5.2.2, the use of cellulose nanocrystals, as an alternative approach to drug loading that is able to fulfill these requirements is described. Additionally, the control of drug release kinetics could be accomplished by means of a tunable polymer matrix.

This is described in section 2.5.1 with the use of a physical crosslinking method for a poly(vinyl alcohol) drug encapsulation matrix with variable diffusion properties.

2.4 Design Criteria

Based on recent developments in the field of drug delivery, we suggest the addition of the following criteria to the list of ideal characteristics of a drug carrying embolization material:

1. Visible/detectable with the use of clinical imaging techniques
2. Degradable following therapeutic treatment
3. Targetable (ie. with application of an external magnetic field)
4. Alternative drug loading and release mechanism

Other aspects that are considered important criteria for the design of new drug-eluting beads include the biocompatibility of all materials and the ability to achieve an ideal microbead size. In the next sections, the materials selected as matrix and the nano-elements to be incorporated will be discussed.

2.5 Materials

2.5.1 Poly(vinyl alcohol) as delivery matrix

Poly(vinyl alcohol) is a polymer that can be transformed into a hydrogel with unique properties that make it a desirable candidate for use in many biomedical applications. Hydrogels are three-dimensional networks of polymer chains that maintain a high water content. PVA is synthesized through the production of polyvinyl acetate via free radical polymerization, followed by a hydrolysis reaction [61]. This produces a carbon chain containing secondary alcohol groups, which allow for significant hydrogen bonding in the presence of water, forming a hydrogel with high water content. In order to stabilize the hydrogel, several crosslinking techniques are used. The use of chemical crosslinking agents is quite common. Examples of these agents are formaldehyde and gluteraldehyde [61,62]. Other methods of crosslinking include γ-irradiation, electron beam treatment, and physical crosslinking [63]. Physical crosslinking has been studied

extensively, especially for materials designed for medical device applications because of its unique ability to control mechanical and diffusion properties of the hydrogel without adding any additional harmful chemicals [63].

As mentioned in section 2.2, the DC bead is stabilized using chemical crosslinking. The use of chemical crosslinking techniques has been noted as only being useful if toxic reagents are completely removed following fabrication and before *in vivo* use [17]. However, this is often not possible as removal would result in instability or premature release of the drug. Physical crosslinking is a method of crosslinking that uses low temperature thermal cycling (LTTC) to induce physical changes within the structure of the hydrogel by altering hydrogen bonding interactions. The material is exposed to a low temperature, usually between -5 and -20°C, and then allowed to thaw to a higher temperature, typically room temperature. These freeze-thaw cycles (FTCs), which can be broken into several stages, result in phase separation, which forces the polymer chains to form domains of structured crystallites. The resulting structure of the PVA hydrogel is a matrix comprised of regions of crystallites – high polymer concentration, and pores – low polymer concentration [64-66]. The end product is a solid gel, also known as PVA cryogel [63]. Techniques including transmission electron microscopy (TEM) [66], small angle X-ray scattering [66], and small angle and ultrasmall angel neutron scattering [65,67] have been used to determine the micro and nanostructure of PVA cryogels.

Several parameters are important in controlling the PVA hydrogel properties. Molecular weight (MW) and PVA solution concentration are important in terms of the resulting hydrogel structure [62,68-71]. An increase in molecular weight, and therefore an increase in polymer chain length, results in an increase in the number and size of crystalline regions [72]. An increase in the PVA concentration has been shown to result in more stable gels with higher degrees of crystallinity and higher degrees of crosslinking [72]. It has also been shown that higher PVA concentrations produce a more rigid cryogel structure due to the increase in intermolecular hydrogel bonding from the presence of more hydroxyl groups [73].

In terms of processing, the number of FTCs, the upper and lower temperature limits, and the rate of freezing and thawing can also be controlled to form different products [62]. Through these methods, modifications can be easily made to control the diffusion properties, which is important for drug delivery applications. The number of FTCs has a significant effect on the structure and properties. It affects the dissolution of PVA cryogels [74] as well as the mechanical properties, with an increase in stiffness correlating to an increase in the number of FTCs [62], up to a maximum number of six FTCs [75,76].

In terms of diffusion, which is highly relevant for drug delivery applications, PVA cryogels have good diffusion characteristics that are highly tunable. The structure comprised of approximately 3nm crystalline regions and 19nm amorphous regions [65], which permit diffusion of certain molecules from the PVA matrix. Diffusion of solutes is related to mesh size, which is related to crystallinity, and a size exclusion phenomenon occurs [77]. The water diffusion coefficient can be adjusted as a function of number of FTCs [78], with a decrease in diffusion resulting from an increase of number of thermal cycles. This demonstrates the ability to tune the diffusion characteristics to achieve optimal delivery of a particular molecule for a specific application. These results are consistent with a study performed by our group. Using bovine serum albumin (BSA) inside of a PVA matrix to study the effect of processing parameters on protein release, it was found that the diffusion coefficients can be modified over a 20-fold range with an decrease in release rate resulting from an increase in the number of FTCs or an increase in the concentration of PVA [63]. The use of chemically crosslinked PVA in current DEBs limits the ability to control diffusion properties the way they can be controlled using physical crosslinking through low temperature thermal cycling. This highlights a benefit of crosslinking the PVA through freeze-thaw (FT) cycling.

Physically crosslinked PVA has been studied quite extensively as a biomaterial for use in drug delivery. A common method of production of these PVA microparticles is through the use of an emulsion technique. Ficek and Peppas prepared microparticles of PVA for controlled delivery of proteins, modeled with BSA, through an emulsion

technique and subsequent exposure to FT cycling. This novel work did not require the use of a crosslinking agent because of the stabilization of the particles using freeze-thaw cycling [79]. Many other studies were undertaken using PVA as the drug carrier for protein [80,81] or DNA encapsulation [82]. Work using a composite material with PVA, such as chitosan or cellulose, has also been completed for drug delivery purposes [83,84].

Poly(vinyl alcohol) treated through low temperature thermal cycling is known to be biostable and nondegradable, with very low dissolution. For many applications in medical devices, PVA hydrogels produced through physical crosslinking are advantageous in this way because they can remain stable in the body over time. In section 2.3.2 however, the degradability of microspheres was discussed in terms of its importance for drug delivery purposes. It is important to look at the dissolution potential of PVA hydrogels and how this can be enhanced in delivery systems.

Lozinsky *et al.* found initial swelling followed by shrinkage of PVA hydrogel beads prepared through one FTC and subjected to water flow in a packed bead column for two weeks. The overall result after two weeks was no net change in mass [85]. Hassan *et al.* modeled the dissolution of crystallites in PVA films prepared by FT cycling and showed that crystallite size was important for dissolution and smaller crystallites dissolved quickly while those with a lamellar thickness greater than 215Å remained stable over time [86]. Separately, they reported that PVA dissolution occurred for PVA chains that were not incorporated into the crystalline structure formed during FT cycling. It was found that the dissolving PVA was not from the crystalline regions and polymer dissolution decreased as the number of FTCs increased. 15% PVA films of low molecular weight (MW 35,740) were placed in 37°C water and a fractional dissolution was observed to plateau at roughly 6 days. Samples subjected to three, five and seven FTCs had dissolved fraction of approximately 0.48, 0.39 and 0.31 respectively. After six days, the polymer dissolution plateaued and the hydrogel was stable, with some changes in swelling [72]. A study producing a multilaminate PVA device for protein delivery also showed that an increase in the number of FTCs decreased the dissolution of PVA. A fractional dissolution for 15% PVA samples (MW

64,000) in water at 37°C over close to 100 hours showed a dissolved fraction of approximately 0.13 and 0.05 for samples prepared with three and five FTCs respectively [74].

Wong determined that after seven days in water or phosphate buffer saline (PBS), PVA samples produced with six FTCs decreased slightly in mass. 10% PVA samples (MW 146,000-186,000) decreased to approximately a 0.88 and 0.83 fraction of their initial mass in water and PBS respectively. It was reported that increases in PVA concentration and the addition of nanofillers to the hydrogel decreased the mass loss [87]. Willcox *et al.* found that aging increased the crystallinity of the hydrogel and during storage at room temperature, sealed physically crosslinked PVA hydrogel samples (19wt% PVA) lost between 8% of their mass (crosslinked using one FTC) or 12% of their mass (12 FTCs) through the expelling of water to the surface of the hydrogel over one year [66].

Finally, the presence of salts has an effect on PVA hydrogel dissolution. Patachia *et al.* reported mass loss of roughly 11% for PVA samples in 1M salt solutions with an increase in mass loss occurring for higher electrolyte concentrations. Mass loss occurs through the loss of water and was shown to reach equilibrium after roughly 25 hours in salt solution [88].

Although biostability is important for many applications such as articular cartilage replacement [89], or cardiovascular tissue replacement [62], it provides an interesting problem for drug delivery applications as undesirable accumulation of the microspheres could occur. This poses several problems, including potential toxicity. As well, it is expected that for use in TACE therapy, accumulation in the arteries close to the tumour, might actually inhibit further TACE administration, or would cause subsequent infusion of microbeads to aggregate at distances further from the site of the tumour, resulting in lower doses of chemotherapeutic agents to tumour cells and unwanted administration of these drugs to surrounding tissue. It is important to look at how degradability of DEBs can potentially be achieved, and specifically if we can

accomplish this using PVA treated through LTTC because of the advantages this material possesses for the application that we have presented.

2.5.2 Incorporated nano-elements

In this section, the nanoparticles that are incorporated into the poly(vinyl alcohol) matrix will be discussed in terms of selection, properties, fabrication, and purpose in the proposed drug delivery embolization system.

2.5.2.1 Iron oxide nanoparticles

Inorganic nanoparticles can be an excellent addition to materials for biomedical applications because they provide the chemical and functional properties of the inorganic component, while possessing the physical properties of the bulk material [90]. Iron oxide nanoparticles have many properties that make them extremely useful in biomedical applications such as cancer therapy and specifically, drug delivery. Magnetite, Fe_3O_4, has an inverse spinel structure with oxygen forming a face-centered cubic close packed arrangement. It is a specific form of iron oxide that is particularly useful in biomedical applications because magnetite particles are biocompatible and non-toxic, breaking down to eventually form blood hemoglobin [91,92]. Magnetite nanoparticles can also have superparamagnetic properties, meaning they respond to an external magnetic field, but do not hold magnetism once the magnetic field is removed.

The magnetic properties of iron oxide nanoparticles have made it useful for magnetic targeting for localized or targeted therapy, as well as for enhancing contrast in magnetic resonance imaging (MRI) [91]. They can be used as an MR contrast agent as they have a strong impact on the T1 and T2 relaxation. T2 relaxation depends on the size and coating of the particles [93]. They have also been studied for use as contrast agents for X-ray and CT imaging [94]. Finally, an additional use for biomedical applications is that they have also demonstrated the ability to induce hyperthermia in the presence of a magnetic field, which can enhance tumour killing [91].

Magnetite nanoparticles are easily produced in a co-precipitation method of ferric and ferrous aqueous salt solutions in a molar ratio of 2:1, in the presence of hydroxide ions [91,92,94]. The following is the overall reaction:

$$Fe^{2+} + 2Fe^{3+} + 8OH^- \rightarrow Fe_3O_4 + 4H_2O \quad (1)$$

The coating of these nanoparticles with a biocompatible polymer, such as poly(vinyl alcohol), has been shown to be useful in several ways. First of all, without coating, iron oxide particles tend to agglomerate to form clusters [91]. Polymer coating can achieve particle monodispersity and stable dispersions [95]. Finally, magnetite-loaded polymeric particles are shown to have low cytotoxicity [96]. The co-precipitation of aqueous ferric and ferrous iron salts in the presence of PVA was demonstrated by Zhou *et al.* to fabricate iron oxide nanoparticle-containing magnetic PVA gel beads for potential use as a drug carrier. The beads had excellent superparamagnetic property and uniform size of 2mm diameter. The precipitation of the iron oxide nanoparticles was described as forming a certain level of crosslinking within a PVA matrix [97].

Work on the interaction of PVA and iron oxide has been previously shown. Using atomic force microscopy, Uner *et al*. demonstrated that a decrease in hydroxyl content (increase in degree of acetylation) resulted in a significant drop in the adhesion force between PVA and the iron oxide. Infrared spectroscopy data supported the notion that increase in degree of acetylation resulted in increased intra and intermolecular hydrogen bonding, leaving hydroxyl groups less available for adhesion with the iron oxide surface [98]. Furthermore, Gonzalez *et al.* completed work on PVA ferrogels produced through co-precipitation of iron salts in PVA, followed by freeze-thaw cycling. They explained that the high affinity of PVA hydroxyl groups to oxide surfaces led to adsorption of PVA onto iron oxide surfaces. A decrease in degree of crystallinity and melting temperature was found in PVA ferrogels (containing magnetite nanoparticles) compared to PVA hydrogels. The authors stated that the decrease in crystallinity suggests that the formation of smaller crystalline regions as a result of the nanoparticles interfering with the ability of PVA chains to form crystallites. Additionally, a decrease in degree of swelling was found in PVA ferrogels.

To explain this, they proposed that the total number of crystallites may actually be increased with the presence of iron oxide nanoparticles, as the nanoparticles may be nucleation centers creating low-mobility regions. These low-mobility regions are essentially crosslinking points, and would therefore decrease swelling [99]. Alternatively, later work by Gonzalez *et al.* on PVA ferrogels prepared through initial freeze-thaw cycling followed by iron salt loading and subsequent co-precipitation into iron oxide showed an increase in degree of crystallinity and melting temperature. This was said to be a result of an additional postcrystallization process from a second drying step, as well as the presence of iron oxide nanoparticles creating a nucleating effect, thus producing larger crystals [100].

The difference in the order of iron oxide precipitation and freeze-thaw cycling may result in a slight difference in the material structure, but the notion that iron oxide nanoparticles form crosslinks in PVA is consistent. This begs the question of whether the subsequent removal of iron oxide nanoparticles from the PVA matrix would remove crosslinks, and therefore allow dissolution of the material. This could be regarded as a form of 'degradable' PVA iron oxide hydrogel. It will be further discussed in chapter 4.

Iron oxide has recently been incorporated into particles designed for embolization in order to enhance contrast for various imaging modalities. Iron oxide incorporated into tris-acryl microspheres [33,101] and chitosan microspheres [47,48,102] have been produced for use as embolization particles detectable using MRI. With the use of CT, iron oxide nanoparticle concentration of at least two orders of magnitude greater can be detected than with 1.5 T MR. Concentrations of 1-40 mg Fe/mL was detected with CT where 0.01-0.4 mg Fe/mL was detected with MRI. This has been suggested to be more useful for specific applications, including magnetic hyperthermia where concentrations of 1-10 mg Fe/mL are often used [103]. Based on the quantity of DEBs typically used in DEB-TACE therapy, and the fact that they accumulate together in the vasculature of tumour regions, it is worth investigating the use of CT to image iron-oxide containing beads fabricated for this application.

2.5.2.2 Bacterial cellulose nanocrystals

Bacterial cellulose (BC) is a biocompatible and non-toxic carbohydrate polymer [104]. It has been studied widely for use in biomedical applications such as wound dressings [105] and reinforcement material for biomedical implants such as cardiovascular tissue [76,106,107]. It is an ideal candidate due to its availability, biocompatibility, high specific strength and modulus, hydrophilicity, high water holding capacity, and ability to form a porous three-dimensional network. Furthermore, in its surface functionalized form, it is an excellent material for drug conjugation in biomedical applications [108].

Cellulose is the most abundant naturally occurring polymer [109], with sources including plant, algae, fungi and bacteria. Bacterial cellulose, synthesized by the bacterium *Gluconacetobacter xylinus* bacteria, is advantageous for biomedical applications because of its purity and high degree of crystallinity [110]. It is a high molecular weight polymer composed of repeating units of two anhydroglucose units with a reducing, and nonreducing end. Hydroxyl groups present in the equatorial ring positions provide the high hydrophilicity and allow for functionalization [111].

It has been demonstrated that through several different reaction routes, BC can be broken down quite effectively into cellulose nanocyrstals (CNC). This occurs as a result of chemical reactions which hydrolyze the disordered (amorphous) regions of the BC fibre, leaving the more ordered crystalline regions intact because they are better able to resist hydrolysis [112]. The end product of these reactions is highly crystalline cellulose in the nanoscale range. CNC has a very high surface to mass ratio [113], which makes it a particularly useful carrier of drug molecules in high loading.

Many studies have reported methods of producing CNC from BC. These include enzymatic hydrolysis, harsh acid hydrolysis, and ammonium persulfate oxidation. Functionalization of the primary alcohol group on the BC or CNC has been demonstrated through many reactions, producing both anionic and cationic surface groups [114-116], with different types of conjugations of therapeutics being demonstrated [117-119]. The well-established 2,2,6,6-tetramethylpiperidine-1-oxyl (TEMPO) mediated oxidation reactions [120] introduces carboxylic acid groups to the

surface, creating a negative surface charge, which allows positively charged drug molecules to be loaded [121]. Alternatively, reactions such as the use of epichlorohydrin and ammonium hydroxide [114], choline-based ionic liquid analogue [122] or epoxypropyltrimethyammonium chloride [123] introduce cationic surface charges to the cellulose fibres, providing means for the loading of negatively charged drug molecules.

Because numerous chemical reactions can be performed on the surface to allow different forms of drug conjugation, drug loading and release chemistry can be tailored to the needs of a specific application. This makes it a very versatile material for a wide range of drug molecules. The high potential drug loading, the ability to load different types of drug molecules, and the ability to tailor drug release make CNC a good candidate for improved drug loading and release in DEBs.

Of interest is the method using hydrogen peroxide to break the BC fibres down into CNC while also oxidizing the surface to produce carboxylic acid groups [124]. This is a facile method that provides a high surface area and high carboxyl functional group content for loading of positively charged drug molecules, such as doxorubicin.

2.6 Proposed system

The system this thesis covers is a microbead comprised of a poly(vinyl alcohol) matrix, loaded with iron oxide nanoparticles and drug-loaded cellulose nanocrystals. This system, illustrated below in Figure 2.3, is a “nano-on-micro” drug delivery system. The grey sphere illustrates the PVA matrix crosslinked through low temperature thermal cycling process in conjunction with iron oxide precipitation. The black dots represent the iron oxide nanoparticles distributed throughout the PVA matrix. The black curved lines illustrate the incorporation of CNC and the red ovals represent the potential to load therapeutic molecules onto CNC within the microbead.

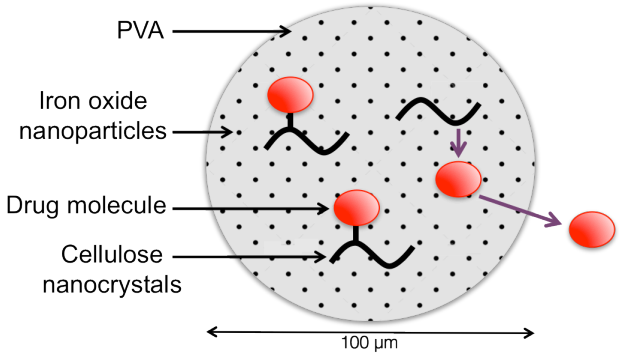

Figure 2.3 Proposed multifunctional nano-on-micro system

The system is hypothesized to be beneficial for use as a drug delivery embolization particle in TACE therapy based on the following reasons: the potential drug loading and release capabilities due to the presence of functionalized CNC; the ability to visualize it using clinical imaging techniques as a result of iron oxide nanoparticle incorporation; the potential for magnetic targeting to a specific location making use of the magnetic properties of iron oxide; and the potential for elimination due to dissolution of the polymer matrix resulting from the degradation of iron oxide nanoparticles.

2.7 System assembly

2.7.1 Microbead fabrication

This portion of the literature review section covers the topic of microbead production, as the fabrication of our microbead system is a significant part of the work described in this thesis.

Polymer microspheres or microparticles can be fabricated using many different techniques. These include interfacial polymerization methods such as suspension polymerization, emulsion polymerization and dispersion polymerization; emulsion-solvent extraction/evaporation; extrusion methods; photolithographic and micromolding methods; and spray drying techniques [16,125]. There are, however, downsides to each of these techniques, with the main problem being difficulty in size

control resulting in particle polydispersity. This has led us to an alternative approach – the use of microfluidic technology.

The ability to control bead size is of high importance. Not only are specific bead diameters more advantageous for the application described in this work, but is has also been suggested that further work should be done to tailor the DEB size to the arterial anatomy of the tumour site [15]. This requires a production method with a great degree of control over microbead size. The desirable size to be fabricated for this application is roughly 100-200μm in diameter. This range of beads have been fabricated using numerous microfluidic techniques and with various materials [126-128].

The use of microfluidics to form emulsions has been explored to produce complex and highly monodisperse particles. Particles of various structures, morphologies, and sizes ranging from nanometers to hundreds of micrometers can be fabricated [126]. Microfluidic devices consist of microchannels, usually around 10-100μm [129-131], through which, in many cases, immiscible phases flow and interact. At the junction between these channels, droplets of one phase are formed. This is called the dispersed phase, with the other liquid being the continuous phase. By controlling parameters such as flow rate, the size of the dispersed phase droplets can be modified [131-133].

Common microfluidic systems are either composed of glass capillary tubing, or microchannels etched into a polymer such as poly(dimethyldisiloxane) (PDMS). Channels can be set up into various configurations including cross-flow, co-flow or flow-focusing configurations in which the continuous and dispersed phases either flow alongside or against each other [134]. Other considerations in the design of a microfluidic system include the placement and location of channels, the interactions of the fluids with the wall, the size and shape of the desired particles, as well as the activity of the therapeutic molecule [131,133].

This approach will be used for the production of our multifunctional nano-on-micro system and will be described in detail in the following sections.

2.7.2 Drug loading and release

The incorporation of CNC within the microbead provides a good route for drug conjugation. CNC can be produced through hydrolysis, with oxidation of the alcohol groups of the cellulose surface occurring. At the proper conditions, oxidized cellulose has been shown to be able to load peptides or drugs containing a positive charge. Spaic demonstrated the loading of benzylamine, a model for doxorubicin, to the BC fibres [121].

With the proper investigation and analysis of CNC functionalization, we can achieve loading of drugs like doxorubicin onto the fibres. Dox contains a primary amine group, which when protonated, will conjugate to deproponated carboxylic acid groups of the CNC.

2.8 Conceptual application

The conceptual application of this system follows a similar procedure to the one currently used with DEBs. The therapeutic molecule, doxorubicin, would be loaded into the prepared microbeads. Microbeads would then be delivered by catheter into the tumour site. Visualization of the particles could be completed in real-time as well as following therapy. Drug release would occur and the microbead matrix would disassemble and be cleared from site, to allow repeat treatment.

References

[1] J. Ferlay, H. Shin, F. Bray, D. Forman, C. Mathers and D. M. Parkin. 2010. Estimates of worldwide burden of cancer in 2008: GLOBOCAN 2008. *Int. J. Cancer* **127**(12): 2893-2917.

[2] A. L. Lewis and R. R. Holden. 2011. DC bead embolic drug-eluting bead: Clinical application in the locoregional treatment of tumours. *Expert Opin. Drug Del.* **8**(2): 153-169.

[3] A. Jemal, F. Bray, M. M. Center, J. Ferlay, E. Ward and D. Forman. 2011. Global cancer statistics. *CA-Cancer J. Clin.* **61**(2): 69-90.

[4] H. B. El-Serag. 2007. Epidemiology of hepatocellular carcinoma in USA. *Hepatol. Res.* **37**(2): S88-S94.

[5] S. F. Altekruse, K. A. McGlynn and M. E. Reichman. 2009. Hepatocellular carcinoma incidence, mortality, and survival trends in the United States from 1975 to 2005. *J. Clin. Oncol.* **27**(9): 1485-1491.

[6] C. Bosetti, F. Levi, P. Boffetta, F. Lucchini, E. Negri and C. La Vecchia. 2008. Trends in mortality from hepatocellular carcinoma in europe, 1980-2004. *Hepatology* **48**(1): 137-145.

[7] J. Llovet, A. Burroughs and J. Bruix. 2003. Hepatocellular carcinoma. *Lancet* **362**(9399): 1907-1917.

[8] J. Bruix and M. Sherman. 2005. Management of hepatoceullular carcinoma. *Hepatology* **42**(5): 1208-1236.

[9] L. Marelli, R. Stigliano, C. Triantos, M. Senzolo, E. Cholongitas, N. Davies, J. Tibballs, T. Meyer, D. W. Patch and A. K. Burroughs. 2007. Transarterial therapy for hepatocellular carcinoma: Which technique is more effective? A systematic review of cohort and randomized studies. *Cardiovasc. Intervent. Radiol.* **30**(1): 6-25.

[10] C. Erichsen, M. Bolmsjö, A. Hugander and P. Jönsson. 1985. Blockage of the hepatic-artery blood flow by biodegradable microspheres (spherex®) combined with local hyperthermia in the treatment of experimental liver tumors in rats. *J. Cancer Res. Clin. Oncol.* **109**(1): 38-41.

[11] D. H. Lee, H. K. Yoon, H. Y. Song, G. C. Kim, J. C. Hwang and K. B. Sung. 1999. Embolization of severe arterioportal shunts in the patients with hepatocellular carcinoma: Safety and influence on patient survival. *J. Kor. Radiol. Soc.* **41**(6): 1117-1125.

[12] J. Furuse, M. Iwasaki, M. Yoshino, M. Konishi, N. Kawano, T. Kinoshita, M. Ryu, M. Satake and N. Moriyama. 1997. Hepatocellular carcinoma with portal vein tumor thrombus: Embolization of arterioportal shunts. *Radiology* **204**(3): 787-790.

[13] K. Ito, H. Kusunoki, E. Okamoto, M. Ozawa, A. Ishikawa, M. Matsuura and N. Nakajima. 1994. Intra-arterial alcoholization of advanced hepatocellular carcinoma. *Cancer Chemother. Pharmacol.* **33**(1): S42-S47.

[14] T. Gunji, N. Kawauchi, S. Ohnishi, T. Ishikawa, H. Nakagama, T. Kaneko, T. Moriyama, N. Matsuhashi, Y. Yazaki and M. Imawari. 1992. Treatment of hepatocellular carcinoma associated with advanced cirrhosis by transcatheter arterial chemoembolization using autologous blood clot: A preliminary report. *Hepatology* **15**(2): 252-257.

[15] A. L. Lewis and M. R. Dreher. 2012. Locoregional drug delivery using image-guided intra-arterial drug eluting bead therapy. *J. Controlled Release* **161**(2): 338-350.

[16] N. Varde and D. Pack. 2004. Microspheres for controlled release drug delivery. *Expert Opin. Biol. Ther.* **4**(1): 35-51.

[17] T. R. Hoare and D. S. Kohane. 2008. Hydrogels in drug delivery: Progress and challenges. *Polymer* **49**(8): 1993-2007.

[18] S. Chaterji, I. K. Kwon and K. Park. 2007. Smart polymeric gels: Redefining the limits of biomedical devices. *Prog. Polym. Sci.* **32**(8-9): 1083-1122.

[19] I. Lentacker, B. Geers, J. Demeester, S. C. De Smedt and N. N. Sanders. 2010. Design and evaluation of doxorubicin-containing microbubbles for ultrasound-triggered doxorubicin delivery: Cytotoxicity and mechanisms involved. *Mol. Ther.* **18**(1): 101-108.

[20] R. R. Patil, S. A. Guhagarkar and P. V. Devarajan. 2008. Engineered nanocarriers of doxorubicin: A current update. *Crit. Rev. Ther. Drug Carrier Syst.* **25**(1): 1-61.

[21] R. Eliaz and F. Szoka. 2001. Liposome-encapsulated doxorubicin targeted to CD44: A strategy to kill CD44-overexpressing tumor cells. *Cancer Res.* **61**(6): 2592-2601.

[22] H. Yoo and T. Park. 2004. Folate receptor targeted biodegradable polymeric doxorubicin micelles. *J. Controlled Release* **96**(2): 273-283.

[23] X. Shuai, H. Ai, N. Nasongkla, S. Kim and J. Gao. 2004. Micellar carriers based on block copolymers of poly(e-caprolactone) and poly(ethylene glycol) for doxorubicin delivery. *J. Controlled Release* **98**(3): 415-426.

[24] E. Piskin, X. Kaitian, E. Denkbas and Z. Kucukyavuz. 1995. Novel PDLLA/PEG copolymer micelles as drug carriers. *J. Biomater. Sci. Polym. Ed.* **7**(4): 359-373.

[25] A. Fundaro, R. Cavalli, A. Bargoni, D. Vighetto, G. Zara and M. Gasco. 2000. Non-stealth and stealth solid lipid nanoparticles (SLN) carrying doxorubicin: Pharmacokinetics and tissue distribution after i.v. administration to rats. *Pharmacol. Res.* **42**(4): 337-343.

[26] Y. Son, J. Jang, Y. Cho, H. Chung, R. Park, I. Kwon, I. Kim, J. Park, S. Seo, C. Park *et al*. 2003. Biodistribution and anti-tumor efficacy of doxorubicin loaded

glycol-chitosan nanoaggregates by EPR effect. *J. Controlled Release* **91**(1-2): 135-145.

[27] A. L. Lewis, M. V. Gonzalez, S. W. Leppard, J. E. Brown, P. W. Stratford, G. J. Phillips and A. W. Lloyd. 2007. Doxorubicin eluting beads-1: Effects of drug loading on bead characteristics and drug distribution. *J. Mat. Sci. Mater. M.* **18**(9): 1691-1699.

[28] M. V. Gonzalez, Y. Tang, G. J. Phillips, A. W. Lloyd, B. Hall, P. W. Stratford and A. L. Lewis. 2008. Doxorubicin eluting beads: Methods for evaluating drug elution and in-vitro: In-vivo correlation. *J. Mater. Sci. Mater. Med.* **19**(2): 767-775.

[29] M. Varela, M. I. Real, M. Burrel, A. Forner, M. Sala, M. Brunet, C. Ayuso, L. Castells, X. Montana, J. M. Llovet *et al*. 2007. Chemoembolization of hepatocellular carcinoma with drug eluting beads: Efficacy and doxorubicin pharmacokinetics. *J. Hepatol.* **46**(3): 474-481.

[30] R. Lencioni, T. de Baere, M. Burrel, J. G. Caridi, J. Lammer, K. Malagari, R. C. G. Martin, E. O'Grady, M. Isabel Real, T. J. Vogl *et al*. 2012. Transcatheter treatment of hepatocellular carcinoma with doxorubicin-loaded DC bead (DEBDOX): Technical recommendations. *Cardiovasc. Intervent. Radiol.* **35**(5): 980-985.

[31] R. Martin, J. Irurzun, J. Munchart, I. Trofimov, A. Scupchenko, C. Tatum and G. Narayanan. 2011. Optimal technique and response of doxorubicin beads in hepatocellular cancer: Bead size and dose. *Kor. J. Hepatol.* **17**(1): 51-60.

[32] M. R. Dreher, K. V. Sharma, D. L. Woods, G. Reddy, Y. Tang, W. F. Pritchard, O. A. Chiesa, J. W. Karanian, J. A. Esparza, D. Donahue *et al*. 2012. Radiopaque drug-eluting beads for transcatheter embolotherapy: Experimental study of drug penetration and coverage in swine. *J. Vasc. Intervent. Radiol.* **23**(2): 257-264.

[33] K. Lee, E. Liapi, J. A. Vossen, M. Buijs, V. P. Ventura, C. Georgiades, K. Hong, I. Kamel, M. S. Torbenson and J. H. Geschwind. 2008. Distribution of iron oxide-containing embosphere particles after transcatheter arterial embolization in an animal model of liver cancer: Evaluation with MR imaging and implication for therapy. *J. Vasc. Interv. Radiol.* **19**(10): 1490-1496.

[34] L. Illum and S. S. Davis. 1982. The targeting of drugs parenterally by use of microspheres. *J. Parenter. Sci. Technol.* **36**(6): 242-248.

[35] P. Giunchedi, M. Maestri, E. Gavini, P. Dionigi and G. Rassu. 2013. Transarterial chemoembolization of hepatocellular carcinoma agents and drugs: An overview. *Expert Opin. Drug Deliv.* **10**(6): 799-810.

[36] D. Kerr. 1987. Microparticulate drug delivery systems as an adjunct to cancer-treatment. *Cancer Drug Deliv.* **4**(1): 55-61.

[37] R. F. Gibson. 2010. A review of recent research on mechanics of multifunctional composite materials and structures. *Compos. Struct.* **92**(12): 2793-2810.

[38] M. Liong, J. Lu, M. Kovochich, T. Xia, S. G. Ruehm, A. E. Nel, F. Tamanoi and J. I. Zink. 2008. Multifunctional inorganic nanoparticles for imaging, targeting, and drug delivery. *ACS Nano* **2**(5): 889-896.

[39] R. E. Brown, K. M. Gibler, T. Metzger, I. Trofimov, H. Krebs, F. Diaz Romero, C. R. Scoggins, K. M. McMasters and C. G. Martin. 2011. Imaged guided transarterial chemoembolization with drug-eluting beads loaded with doxorubicin (DEBDOX) for hepatic metastases from melanoma: Early outcomes from a multi-institutional registry. *Am. Surg.* **77**(1): 93-98.

[40] K. V. Sharma, M. R. Dreher, Y. Tang, W. Pritchard, O. A. Chiesa, J. Karanian, J. Peregoy, B. Orandi, D. Woods, D. Donahue *et al*. 2010. Development of "imageable" beads for transcatheter embolotherapy. *J. Vasc. Interv. Radiol.* **21**(6): 865-876.

[41] G. Deray. 2006. Dialysis and iodinated contrast media. *Kidney Int.* **69**: S25-S29.

[42] S. H. Bartling, J. Budjan, H. Aviv, S. Haneder, B. Kraenzlin, H. Michaely, S. Margel, S. Diehl, W. Semmler, N. Gretz *et al*. 2011. First multimodal embolization particles visible on X-ray/computed tomography and magnetic resonance imaging. *Invest. Radiol.* **46**(3): 178-186.

[43] K. Hong, A. Khwaja, E. Liapi, M. S. Torbenson, C. S. Georgiades and J. F. H. Geschwind. 2006. New intra-arterial drug delivery system for the treatment of liver cancer: Preclinical assessment in a rabbit model of liver cancer. *Clin. Cancer Res.* **12**(8): 2563-2567.

[44] J. Namur, M. Wassef, J. Millot, A. L. Lewis, M. Manfait and A. Laurent. 2010. Drug-eluting beads for liver embolization: Concentration of doxorubicin in tissue and in beads in a pig model. *J. Vasc. Interv. Radiol.* **21**(2): 259-267.

[45] C. M. Sommer, U. Stampfl, N. Bellemann, M. Holzschuh, A. Kueller, J. Bluemmel, T. Gehrig, M. Shevchenko, H. G. Kenngott, H. U. Kauczor *et al*. 2013. Multimodal visibility (radiography, computed tomography, and magnetic resonance imaging) of microspheres for transarterial embolization tested in porcine kidneys. *Invest. Radiol.* **48**(4): 213-222.

[46] R. Cilliers, Y. Song, E. K. Kohlmeir, A. C. Larson, R. A. Omary and T. J. Meade. 2008. Modification of embolic-PVA particles with MR contrast agents. *Magn. Reson. Med.* **59**(4): 898-902.

[47] S. Y. Choi, B. K. Kwak, H. J. Shim, J. Lee, S. U. Hong and K. A. Kim. 2015. MRI traceability of superparamagnetic iron oxide nanoparticle-embedded chitosan microspheres as an embolic material in rabbit uterus. *Diagn. Interv. Radiol.* **21**(1): 47-53.

[48] E. Chung, H. Kim, G. Lee, B. Kwak, J. Jung, H. Kuh and J. Lee. 2012. Design of deformable chitosan microspheres loaded with superparamagnetic iron oxide nanoparticles for embolotherapy detectable by magnetic resonance imaging. *Carbohydr. Polym.* **90**(4): 1725-1731.

[49] H. Bhat, Q. Yang, S. Zuehlsdorff, K. Li and D. Li. 2010. Contrast-enhanced whole-heart coronary magnetic resonance angiography at 3 T using interleaved echo planar imaging. *Invest. Radiol.* **45**(8): 458-464.

[50] E. Liapi and J. H. Geschwind. 2011. Transcatheter arterial chemoembolization for liver cancer: Is it time to distinguish conventional from drug-eluting chemoembolization? *Cardiovasc. Intervent. Radiol.* **34**(1): 37-49.

[51] V. Sinha and A. Trehan. 2003. Biodegradable microspheres for protein delivery. *J. Controlled Release* **90**(3): 261-280.

[52] N. Kumar, R. Langer and A. Domb. 2002. Polyanhydrides: An overview. *Adv. Drug Deliv. Rev.* **54**(7): 889-910.

[53] J. Tamada and R. Langer. 1993. Erosion kinetics of hydrolytically degradable polymers. *Proc. Natl. Acad. Sci. USA* **90**(2): 552-556.

[54] C. Alexiou, W. Arnold, R. Klein, F. Parak, P. Hulin, C. Bergemann, W. Erhardt, S. Wagenpfeil and A. Lubbe. 2000. Locoregional cancer treatment with magnetic drug targeting. *Cancer Res.* **60**(23): 6641-6648.

[55] A. Akbarzadeh, M. Samiei and S. Davaran. 2012. Magnetic nanoparticles: Preparation, physical properties, and applications in biomedicine. *Nanoscale Res. Lett.* **7**(144): 1-13.

[56] S. Singamaneni, V. N. Bliznyuk, C. Binek and E. Y. Tsymbal. 2011. Magnetic nanoparticles: Recent advances in synthesis, self-assembly and applications. *J. Mater. Chem.* **21**(42): 16819-16845.

[57] M. Mahmoudi, S. Sant, B. Wang, S. Laurent and T. Sen. 2011. Superparamagnetic iron oxide nanoparticles (SPIONs): Development, surface modification and applications in chemotherapy. *Adv. Drug Deliv. Rev.* **63**(1-2): 24-46.

[58] B. Shapiro. 2009. Towards dynamic control of magnetic fields to focus magnetic carriers to targets deep inside the body. *J. Magn. Magn. Mater.* **321**(10): 1594-1599.

[59] P. Pouponneau, J. Leroux and S. Martel. 2009. Magnetic nanoparticles encapsulated into biodegradable microparticles steered with an upgraded magnetic resonance imaging system for tumor chemoembolization. *Biomaterials* **30**(31): 6327-6332.

[60] B. Liang, C. Zheng, G. Feng, H. Wu, Y. Wang, H. Zhao, J. Qian and H. Liang. 2010. Correlation of hypoxia-inducible factor 1 alpha with angiogenesis in liver tumors after transcatheter arterial embolization in an animal model. *Cardiovasc. Intervent. Radiol.* **33**(4): 806-812.

[61] C. Hassan and N. Peppas. 2000. Structure and applications of poly(vinyl alcohol) hydrogels produced by conventional crosslinking or by freezing/thawing methods. *Adv. Polym. Sci.* **153**(1): 37-65.

[62] W. Wan, G. Campbell, Z. Zhang, A. Hui and D. Boughner. 2002. Optimizing the tensile properties of polyvinyl alcohol hydrogel for the construction of a bioprosthetic heart valve stent. *J. Biomed. Mater. Res.* **63**(6): 854-861.

[63] W. Wan, A. D. Bannerman, L. Yang and H. Mak. 2014. Poly(vinyl alcohol) cryogels for biomedical applications. *Polymeric Cryogels* **263**: 283-321.

[64] F. Yokoyama, I. Masada, K. Shimamura, T. Ikawa and K. Monobe. 1986. Morphology and structure of highly elastic poly (vinyl alcohol) hydrogel prepared by repeated freezing-and-melting. *Colloid Polym. Sci.* **264**(7): 595-601.

[65] L. E. Millon, M. Nieh, J. L. Hutter and W. Wan. 2007. SANS characterization of an anisotropic poly(vinyl alcohol) hydrogel with vascular applications. *Macromolecules* **40**(10): 3655-3662.

[66] P. Willcox, D. Howie, K. Schmidt-Rohr, D. Hoagland, S. Gido, S. Pudjijanto, L. Kleiner and S. Venkatraman. 1999. Microstructure of poly(vinyl alcohol) hydrogels produced by freeze/thaw cycling. *J. Polym. Sci. Pol. Phys.* **37**(24): 3438-3454.

[67] S. D. Hudson, J. L. Hutter, M. Nieh, J. Pencer, L. E. Millon and W. Wan. 2009. Characterization of anisotropic poly(vinyl alcohol) hydrogel by small- and ultra-small-angle neutron scattering. *J. Chem. Phys.* **130**(3): 034903.

[68] T. Kanaya, M. Ohkura, K. Kaji, M. Furusaka and M. Misawa. 1994. Structure of poly(vinyl alcohol) gels studied by wide-angle and small-angle neutron-scattering. *Macromolecules* **27**(20): 5609-5615.

[69] T. Kanaya, M. Ohkura, H. Takeshita, K. Kaji, M. Furusaka, H. Yamaoka and G. Wignall. 1995. Gelation process of poly(vinyl alcohol) as studied by small-angle neutron and light-scattering. *Macromolecules* **28**(9): 3168-3174.

[70] B. J. Ficek and N. A. Peppas. 1993. Novel preparation of poly(vinyl alcohol) microparticles without cross-linking agent for controlled drug-delivery of proteins. *J. Controlled Release* **27**(3): 259-264.

[71] N. A. Peppas and J. E. Scott. 1992. Controlled release from poly(vinyl alcohol) gels prepared by freezing-thawing processes. *J. Controlled Release* **18**(2): 95-100.

[72] C. Hassan and N. Peppas. 2000. Structure and morphology of freeze/thawed PVA hydrogels. *Macromolecules* **33**(7): 2472-2479.

[73] V. Lozinsky, L. Damshkaln, B. Shaskol'skii, T. Babushkina, I. Kurochkin and I. Kurochkin. 2007. Study of cryostructuring of polymer systems: 27. Physicochemical properties of poly(vinyl alcohol) cryogels and specific features of their macroporous morphology. *Colloid J.* **69**(6): 747-764.

[74] C. Hassan, J. Stewart and N. Peppas. 2000. Diffusional characteristics of freeze/thawed poly(vinyl alcohol) hydrogels: Applications to protein controlled release from multilaminate devices. *Eur. J. Pharm. Biopharm.* **49**(2): 161-165.

[75] J. L. Holloway, K. L. Spiller, A. M. Lowman and G. R. Palmese. 2011. Analysis of the in vitro swelling behavior of poly(vinyl alcohol) hydrogels in osmotic pressure solution for soft tissue replacement. *Acta Biomater.* **7**(6): 2477-2482.

[76] L. E. Millon and W. K. Wan. 2006. The polyvinyl alcohol-bacterial cellulose system as a new nanocomposite for biomedical applications. *J. Biomed. Mater. Res. B* **79**(2): 245-253.

[77] A. S. Hickey and N. A. Peppas. 1995. Mesh size and diffusive characteristics of semicrystalline poly (vinyl alcohol) membranes prepared by freezing/thawing techniques. *J. Membr. Sci.* **107**(3): 229-237.

[78] S. R. Stauffer and N. A. Peppas. 1992. Poly(vinyl alcohol) hydrogels prepared by freezing-thawing cyclic processing. *Polymer* **33**(18): 3932-3936.

[79] B. Ficek and N. Peppas. 1993. Novel preparation of poly(vinyl alcohol) microparticles without cross-linking agent for controlled drug-delivery of proteins. *J. Controlled Release* **27**(3): 259-264.

[80] W. Lyoo, D. Shin, S. Han, S. Noh, J. Kim, H. Choi, C. Yong, J. Kim and J. Kim. 2006. Release behaviour of bovine serum albumin in syndiotactic poly(vinyl alcohol) hydrogel, prepared by freezing-thawing. *Polym. Polym. Compos.* **14**(1): 39-46.

[81] J. K. Li, N. Wang, and X. S. Wu. 1998. Poly(vinyl alcohol) nanoparticles prepared by freezing-thawing process for protein/peptide drug delivery. *J. Control. Release.* **56**: 117-126.

[82] A. J. M. Valente, S. M. A. Cruz, M. C. Moran, D. B. Murtinho, E. C. Muniz and M. G. Miguel. 2010. Release of DNA from cryogel PVA-DNA membranes. *Express Polym. Lett.* **4**(8): 480-487.

[83] A. M. Abdel-Mohsen, A. S. Aly, R. Hrdina, A. S. Montaser and A. Hebeish. 2011. Eco-synthesis of PVA/chitosan hydrogels for biomedical application. *J. Polym. Environ.* **19**(4): 1005-1012.

[84] Y. Li, Y. Du, Y. Tang, and X. Wang. 2009. A novel pH-sensitive and freeze-thawed carboxymethyl chitosan/poly(vinyl alcohol) blended hydrogel for protein delivery. *Polym, Int.* **58**(10): 1120-1125.

[85] V. I. Lozinsky, A. L. Zubov, I. N. Savina and F. M. Plieva. 2000. Study of cryostructuration of polymer systems. XIV poly(vinyl alcohol) cryogels: Apparent yield of the freeze–thaw-induced gelation of concentrated aqueous solutions of the polymer. *J. Appl. Polym. Sci.* **77**(8): 1822-1831.

[86] C. Hassan, J. Ward and N. Peppas. 2000. Modeling of crystal dissolution of poly(vinyl alcohol) gels produced by freezing/thawing processes. *Polymer* **41**(18): 6729-6739.

[87] E. Y. L. Wong. 2012. *Poly(vinyl alcohol) nanocomposite hydrogels for intervertebral disc prostheses*. Dissertation/Thesis: The University of Western Ontario.

[88] S. Patachia, A. J. M. Valente and C. Baciu. 2007. Effect of non-associated electrolyte solutions on the behaviour of poly(vinyl alcohol)-based hydrogels. *Eur. Polym. J.* **43**(2): 460-467.

[89] C. E. Macias, H. Bodugoz-Senturk and O. K. Muratoglu. 2013. Quantification of PVA hydrogel dissolution in water and bovine serum. *Polymer* **54**(2): 724-729.

[90] R. W. Siegel. 1999. *Nanostructure Science and Technology.* World Technology Division: Loyola College.

[91] A. Gupta and M. Gupta. 2005. Synthesis and surface engineering of iron oxide nanoparticles for biomedical applications. *Biomaterials* **26**(18): 3995-4021.

[92] U. Schwertmann and R. M. Cornell. 2000. *Iron Oxides in the Laboratory: Preparation and Characterization*. Wiley.

[93] C. M. Sorensen. 2001. *Magnetism*. In *Nanoscale materials in chemistry*, K. J. Klabunde, Ed. Wiley, pp. 169.

[94] S. Laurent, D. Forge, M. Port, A. Roch, C. Robic, L. V. Elst and R. N. Muller. 2008. Magnetic iron oxide nanoparticles: Synthesis, stabilization, vectorization, physicochemical characterizations, and biological applications. *Chem. Rev.* **108**(6): 2064-2110.

[95] J. Lee, T. Isobe and M. Senna. 1996. Preparation of ultrafine Fe_3O_4 particles by precipitation in the presence of PVA at high pH. *J. Colloid Interface Sci.* **177**(2): 490-494.

[96] I. Bouhon, M. Shinkai, K. Honda and T. Kobayashi. 1997. Enhancement of cytokine expression in transiently transfected cells by magnetoliposome mediated hyperthermia. *Cytotechnology* **25**(1-3): 231-234.

[97] L. Zhou, B. He and F. Zhang. 2012. Facile one-pot synthesis of iron oxide nanoparticles cross-linked magnetic poly(vinyl alcohol) gel beads for drug delivery. *ACS Appl. Mater. Interfaces* **4**(1): 192-199.

[98] B. Uner, M. K. Ramasubramanian, S. Zauscher and J. F. Kadla. 2006. Adhesion interactions between poly(vinyl alcohol) and iron-oxide surfaces: The effect of acetylation. *J. Appl. Polym. Sci.* **99**(6): 3528-3534.

[99] J. S. Gonzalez, C. E. Hoppe, D. Muraca, F. H. Sanchez and V. A. Alvarez. 2011. Synthesis and characterization of PVA ferrogels obtained through a one-pot freezing-thawing procedure. *Colloid Polym. Sci.* **289**(17-18): 1839-1846.

[100] J. S. Gonzalez, C. E. Hoppe, P. M. Zelis, L. Arciniegas, G. A. Pasquevich, F. H. Sanchez and V. A. Alvarez. 2014. Simple and efficient procedure for the synthesis of ferrogels based on physically cross-linked PVA. *Ind. Eng. Chem. Res.* **53**(1): 214-221.

[101] J. Namur, R. Chapot, J. Pelage, M. Wassef, F. Langevin, D. Labarre and A. Laurent. 2007. MR imaging detection of superparamagnetic iron oxide-loaded tris-acryl embolization microspheres. *J. Vasc. Interv. Radiol.* **18**(10): 1287-1295.

[102] M. J. Kang, I. Y. Oh, B. Choi, B. K. Kwak, J. Lee and Y. W. Choi. 2009. Development of superparamagnetic iron oxide nanoparticles (SPIOs)-embedded chitosan microspheres for magnetic resonance (MR)-traceable embolotherapy. *Biomol. Ther.* **17**(1): 98-103.

[103] V. S. Kalambur, S. Hui and J. C. Bischof. 2007. Multifunctional magnetic nanoparticles for biomedical applications. *P. Soc. Photo-Opt. Ins.* **6440**: V4380-V4400.

[104] S. I. Jeong, S. E. Lee, H. Yang, Y. Jin, C. Park and Y. S. Park. 2010. Toxicologic evaluation of bacterial synthesized cellulose in endothelial cells and animals. *Mol. Cell. Toxicol.* **6**(4): 373-380.

[105] W. Czaja, A. Krystynowicz, S. Bielecki and R. Brown. 2006. Microbial cellulose: The natural power to heal wounds. *Biomaterials* **27**(2): 145-151.

[106] L. E. Millon, G. Guhados and W. Wan. 2008. Anisotropic polyvinyl alcohol-bacterial cellulose nanocomposite for biomedical applications. *J. Biomed. Mater. Res. B* **86**(2): 444-452.

[107] H. Mohammadi, D. Boughner, L. E. Millon and W. K. Wan. 2009. Design and simulation of a poly(vinyl alcohol)-bacterial cellulose nanocomposite mechanical aortic heart valve prosthesis. *Proc. Inst. Mech. Eng. H.* **223**(6): 697-711.

[108] M. Spaic, D. P. Small, J. R. Cook and W. Wan. 2014. Characterization of anionic and cationic functionalized bacterial cellulose nanofibres for controlled release applications. *Cellulose* **21**(3): 1529-1540.

[109] R. Cannon and S. Anderson. 1991. Biogenesis of bacterial cellulose. *Crit. Rev. Microbiol.* **17**(6): 435-447.

[110] D. Klemm, B. Heublein, H. Fink and A. Bohn. 2005. Cellulose: Fascinating biopolymer and sustainable raw material. *Angew. Chem. Int. Edit.* **44**(22): 3358-3393.

[111] M. Samir, F. Alloin and A. Dufresne. 2005. Review of recent research into cellulosic whiskers, their properties and their application in nanocomposite field. *Biomacromolecules* **6**(2): 612-626.

[112] A. C. Correa, E. d. M. Teixeira, L. A. Pessan and L. H. Capparelli Mattoso. 2010. Cellulose nanofibers from curaua fibers. *Cellulose* **17**(6): 1183-1192.

[113] Y. Habibi, L. A. Lucia and O. J. Rojas. 2010. Cellulose nanocrystals: Chemistry, self-assembly, and applications. *Chem. Rev.* **110**(6): 3479-3500.

[114] S. Dong and M. Roman. 2007. Fluorescently labeled cellulose nanocrystals for bioimaging applications. *J. Am. Chem. Soc.* **129**(45): 13810-13811.

[115] T. Saito, Y. Okita, T. T. Nge, J. Sugiyama and A. Isogai. 2006. TEMPO-mediated oxidation of native cellulose: Microscopic analysis of fibrous fractions in the oxidized products. *Carbohydr. Polym.* **65**(4): 435-440.

[116] S. Montanari, M. Rountani, L. Heux and M. Vignon. 2005. Topochemistry of carboxylated cellulose nanocrystals resulting from TEMPO-mediated oxidation. *Macromolecules* **38**(5): 1665-1671.

[117] B. L. Peng, N. Dhar, H. L. Liu and K. C. Tam. 2011. Chemistry and applications of nanocrystalline cellulose and its derivatives: A nanotechnology perspective. *Can. J. Chem. Eng.* **89**(5): 1191-1206.

[118] L. Zhu, V. Kumar and G. Banker. 2004. Examination of aqueous oxidized cellulose dispersions as a potential drug carrier. I. preparation and characterization of oxidized cellulose-phenylpropanolamine complexes. *Aaps Pharmscitech* **5**(4): 69.

[119] D. P. Small, J. R. Cook, M. Spaic and W. Wan. 2012. *Nanocrystalline cellulose for protein and nucleic acid delivery*. In *9th World Biomaterials Congress,* Chengdu China.

[120] A. Denooy, A. Besemer and H. Vanbekkum. 1995. Highly selective nitroxyl radical-mediated oxidation of primary alcohol groups in water-soluble glucans. *Carbohydr. Res.* **269**(1): 89-98.

[121] M. Spaic. 2011. *Functionalized bacterial cellulose for controlled release and delivery*. Dissertation/Thesis: The University of Western Ontario.

[122] A. P. Abbott, T. J. Bell, S. Handa and B. Stoddart. 2006. Cationic functionalisation of cellulose using a choline based ionic liquid analogue. *Green Chem.* **8**(9): 784-786.

[123] M. Hasani, E. D. Cranston, G. Westman and D. G. Gray. 2008. Cationic surface functionalization of cellulose nanocrystals. *Soft Matter* **4**(11): 2238-2244.

[124] J. Cook. 2013. *Amine Functionalization of Bacterial Cellulose for Targeted Delivery Applications*. Dissertation/Thesis: The University of Western Ontario.

[125] J. K. Oh, R. Drumright, D. J. Siegwart and K. Matyjaszewski. 2008. The development of microgels/nanogels for drug delivery applications. *Prog. Polym. Sci.* **33**(4): 448-477.

[126] J. Wang, J. Wang and J. Han. 2011. Fabrication of advanced particles and particle-based materials assisted by droplet-based microfluidics. *Small* **7**(13): 1728-1754.

[127] J. Zhang, R. J. Coulston, S. T. Jones, J. Geng, O. A. Scherman and C. Abell. 2012. One-step fabrication of supramolecular microcapsules from microfluidic droplets. *Science* **335**(6069): 690-694.

[128] M. Windbergs, Y. Zhao, J. Heyman and D. A. Weitz. 2013. Biodegradable core-shell carriers for simultaneous encapsulation of synergistic actives. *J. Am. Chem. Soc.* **135**(21): 7933-7937.

[129] G. M. Whitesides. 2006. The origins and the future of microfluidics. *Nature* **442**(7101): 368-373.

[130] A. J. DeMello. 2006. Control and detection of chemical reactions in microfluidic systems. *Nature* **442**(7101): 394-402.

[131] S. Teh, R. Lin, L. Hung and A. P. Lee. 2008. Droplet microfluidics. *Lab Chip* **8**(2): 198-220.

[132] T. Nisisako, T. Torii and T. Higuchi. 2002. Droplet formation in a microchannel network. *Lab Chip* **2**(1): 24-26.

[133] B. Hallmark, C. Parmar, D. Walker, C. H. Hornung, M. R. Mackley and J. F. Davidson. 2009. The experimental observation and modelling of microdroplet formation within a plastic microcapillary array. *Chem. Eng. Sci.* **64**(22): 4758-4764.

[134] S. Yeom and S. Y. Lee. 2011. Size prediction of drops formed by dripping at a micro T-junction in liquid-liquid mixing. *Exp. Therm. Fluid Sci.* **35**(2): 387-394.

CHAPTER 3 – Multifunctional Microbeads

3.1 Introduction

This chapter describes the design and fabrication of a microfluidic device for the production of microbeads, followed by microbead fabrication and characterization. A flow-focusing configuration was selected for the microfluidic device, optimization of conditions used for microfluidic microbead production was performed, and microbeads composed of PVA, iron oxide nanoparticles, and CNC were produced. Microbead characterization was undertaken to determine size, structure, and composition. In this work, we also briefly investigate the magnetic properties and visualization capabilities of the microbeads produced.

3.2 Materials and methods

All chemicals used were ACS reagent grade and purchased from Sigma-Aldrich. Distilled water was used for all experiments. Bacterial cellulose was synthesized in the laboratory according to the procedure outlined in Appendix I. Bacterial cellulose samples were converted into CNC using a hydrogen peroxide hydrolysis reaction procedure developed by another member in our research group and were provided to me for implementation in my work. CNC with a width of approximately 20nm and length ranging between 100 and 2000nm were used.

3.2.1 Solution preparation

Four different solution compositions have been used throughout this study to produce microbeads, and are outlined in Table 3.1.

Table 3.1 Dispersed phase solution composition

Solution	Identification	Composition
1	**Low iron PVA**	5wt% PVA + 1wt% $FeCl_3$ + 0.6wt% $FeCl_2$•$4H_20$wt% in water
2	**High iron PVA**	5wt% PVA + 3.1wt% $FeCl_3$ + 1.9wt% $FeCl_2$•$4H_20$wt% in water
3	**High iron PVA CNC**	5wt% PVA + 3.1wt% $FeCl_3$ + 1.9wt% $FeCl_2$•$4H_20$wt%+ 1wt% CNC in water
4	**High iron PVA CNC-10**	5wt% PVA + 3.1wt% $FeCl_3$ + 1.9wt% $FeCl_2$•$4H_20$wt%+ 10wt% CNC in water

To produce these solutions, poly(vinyl alcohol), MW 146,000-186,000, 99+% hydrolyzed, was dissolved into a quantity of water making up 80wt% of the total final solution. This was heated to 90°C for approximately 3 hours, or until complete dissolution. Separately, iron (III) chloride ($FeCl_3$) and iron (II) chloride tetrahydrate ($FeCl_2$•$4H_20$) (in a 2:1 molar ratio of Fe^{3+} to Fe^{2+}) were weighed out and added to water (comprising the remaining water quantity required for final solution composition outlined in Table 3.1). This was mixed with a magnetic stirrer for several hours. The PVA solution, after cooling, was added to the iron chlorides solution and mixed with magnetic stirring. The final solution was filtered through a 5µm filter (Acrodisc syringe filter with Versapor Membranes) to ensure any suspended impurities were removed.

For solutions 3 and 4 in Table 3.1, cellulose nanocrystals (CNC) were incorporated. To do this, wet CNC was weighed out to the desired amount and added to the prepared solution of PVA and iron chlorides in water. The resulting solution was sonicated with an ultrasonic probe (Q Sonica Sonicator ultrasonic processor) for 1 minute at 120W. The solution was mixed with a magnetic stirrer prior to use.

The solution compositions that were determined to be best were the high iron PVA solution (Table 3.1 solution 2) and the high iron PVA CNC solution (Table 3.1 solution 3). These were used as the microbead compositions for the following experiments. The exception to this are those used for scanning electron microscopy (SEM) images, energy dispersive X-ray spectroscopy (EDX), and part of the CT experiment, which

were performed on microbeads fabricated using the low iron PVA solution (Table 3.1 solution 1).

3.2.2 Microchannel device fabrication

The design and fabrication of a custom-designed microchannel device was necessary for microbead production. Microchannels were milled out of poly(methyl methacrylate) (PMMA), assembled with another slab of PMMA and connected with screws. 0.038" outer diameter tubing (Intramedic polyethylene tubing, BD) was connected to the outlet hole. 20 gauge stainless steel needles (Hamilton Company) were connected to the inlets, and attached to syringes using 0.125" outer diameter silicone tubing (Cole Parmer) and standard luer lock (Cadence Science). A 10mL syringe was filled with the continuous (oil) phase solution and a 1mL syringe was filled with the dispersed (PVA iron) phase solution. These syringes were loaded onto micropumps (NE-1000, New Era Pump Systems Inc.) and the flow rates controlled. A microchannel device and the entire experimental set up is shown in Figure 3.1. Further details of the microchannel devices and the final design choice used for microbead production is described in section 3.3.

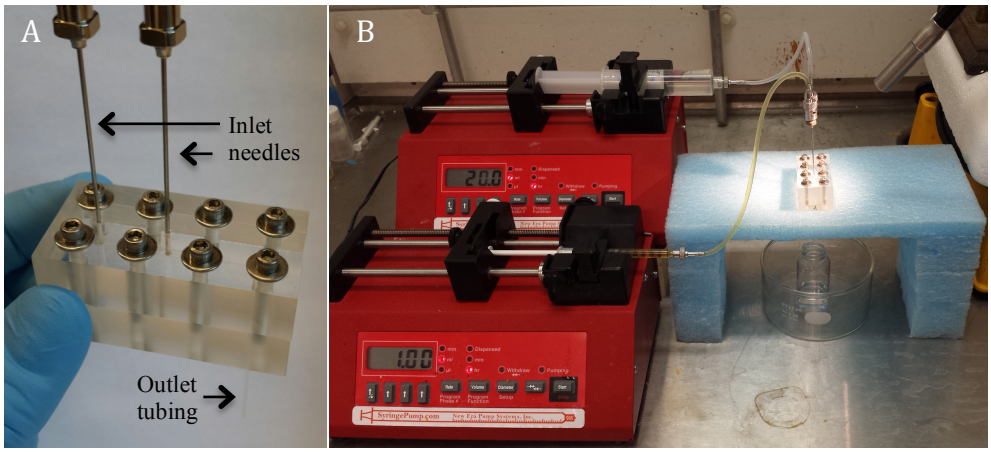

Figure 3.1 A) Custom-designed microchannel device. B) Microchannel production experimental set up.

3.2.3 Microbead production

The channel and system was set up as shown in Figure 3.1. The solutions listed in Table 3.1 were used to produce microbeads through the custom-designed microchannel device. The continuous and dispersed phases flowed through the device to form

dispersed phase solution drops. At the outlet, they fell into a sodium hydroxide (NaOH) solution whereby the PVA-containing dispersed phase solution droplet solidified, forming microbeads. Images of the beads flowing through the microchannel device were taken using a high-speed camera (Redlake MotionScope M with frame rate up to 1000frames/sec). Solution flow was maintained until steady state was reached (~5min) before sample collection. The beads were further washed with 50v/v% ethanol in water several times. These samples were then subjected to one FTC. This was completed either in a -20°C freezer overnight followed by thawing to room temperature or in a water bath with controlled temperature (0.1°C/min to -20°C, held for one hour at -20°C, 0.1°C/min to 20°C).

3.2.4 Optical microscopy

Images were taken for characterization and size analysis of the microbeads using optical microscopy (Olympus BX60). Images were taken with a OMRX A35100U camera attachment to the microscope and the area of the beads were measured using Image J software particle analyzer function for over 100 samples. This data was then converted into an equivalent spherical diameter. Statistical analysis was performed on the mean equivalent spherical diameters using an unpaired t test, and a p-value of < 0.05 was considered significant (GraphPad Prism).

3.2.5 Scanning electron microscopy

SEM was performed on the microbeads to characterize the structure and morphology of the surface. Microbeads beads were dehydrated through to 100% ethanol by incrementally increasing ethanol concentration. Critical point drying (Samdri PVT-3B) was performed on the microbeads suspended on filter paper. Microbeads were loaded onto a p type silicon wafer with 0-10 Ohm-cm resistivity and an orientation of 100 (University Wafers), and subsequently coated with osmium (OPC-60A Osmium Plasma Coater). Images were taken with a scanning electron microscope (LEO (Zeiss) 1540XB FIB/SEM).

3.2.6 Energy dispersive X-ray spectroscopy

EDX is a technique used for elemental analysis of a given sample. EDX (LEO (Zeiss) 1540XB FIB/SEM) was performed on the samples prepared for SEM described in section 3.2.5.

3.2.7 Transmission electron microscopy

To characterize the internal composition of the microbeads, transmission electron microscopy (TEM) was performed. Beads fabricated using the high iron PVA solution (Table 3.1 solution 2) were dehydrated in acetone and then embedded in an Epon-Alardite epoxy resin (3.5mL Araldite 502, 4.5mL Epon 812, 18mL DDSA, 0.67mL DMP). This was completed by the submergence of beads in incrementally increasing concentrations of acetone, acetone and epoxy resin, and finally, kept overnight in 100% epoxy. Following this, beads in epoxy were heated in an oven at 60°C overnight in plastic molds. Samples were ultramicrotomed (Reichert-Jung Ultracut E) with an ultrafine diamond knife to a thickness of 70nm and placed on Formvar carbon-coated 100 mesh copper grids (Electron Microscopy Specialists). The samples were examined under TEM using a Philips TEM (CM-10.s). Iron oxide nanoparticle size was measured using Image J software. Based on the images selected for measurement, an intensity threshold between 0 and 80 was selected to differentiate the particles from the background, and the particle analyzer function was then used to measure particle area. This was converted into an equivalent spherical diameter. (See Appendix IV for images used in this measurement).

3.2.8 X-ray diffraction

To identify the crystalline material present in the microbeads, X-ray diffraction (XRD) was performed. Beads fabricated with the high iron PVA CNC solution (Table 3.1 solution 3) were dried at 60°C overnight and placed on a glass slide with double sided tape. XRD analysis was performed using a Rigaku-Rotaflex Diffractometer (RU-200BH) with a Co-kα radiation (λ =1.79 Å) at 30kV and 44mA. Spectra with a 2θ diffraction angle were scanned from 0° to 82° with a 0.2° step size. A background scan

was performed on the blank slide with tape, and the relative peaks were subtracted from the sample peaks. Spectra were plotted for a 2θ of 10° to 82°.

3.2.9 Clinical computed tomography

Computed tomography of microbead samples was performed in order to determine the visibility of the multifunctional microbeads under clinical imaging techniques. Microbeads produced using the low iron PVA solution (Table 3.1 solution 1) and the high iron PVA CNC solutions (Table 3.1 solution 3) were used. Additionally, 5wt% PVA solution processed as a film using LTTC (see section 4.2.2 for preparation procedure) was imaged as a control. These control films were homogenized (Brinkmann Homogenizer Polytron PT 10/35) on high speed to produce small pieces.

Various quantities of microbeads and equivalent quantities of plain PVA samples were weighed out and suspended in phosphate buffer saline (PBS) solution and contained within 1.5mL microcentrifuge tubes. These tubes were held in a tube rack and placed within the scanner. Samples were imaged using clinical CT (GE Healthcare Discovery VCT). Axial scans were completed with a rotation time of 0.4 seconds using a bone reconstruction scan type. Conditions were set to 80 kV, 300 mA, and a slice thickness of 0.625mm. Two different window width (W) (Hounsfield units) and level (L) (Hounsfield number) settings were used to view the images: W/L of 426/183 and 650/100.

3.2.10 Acid/base titration of cellulose nanocrystals

To measure the carboxyl content on the CNC, an acid/base titration was performed. 0.1g wet CNC was weighed out and dispersed into 10mL 1mM hydrochloric acid (HCl) solution using an ultrasonic probe (Q Sonica Sonicater ultrasonic processor, Newton, CT) for 30 seconds at 120W. 1mM NaOH was titrated against the solution containing CNC and the curve was plotted. This was repeated in triplicate. The same procedure was performed on a sample of the BC used as the reactant for the conversion to CNC. Additional washes with dilute acid and water were performed on the BC sample before titration to ensure any residual NaOH from BC harvest and separation was neutralized

and removed. The carboxyl content of the CNC was calculated using Equation 2. The wet CNC contained 99% water and therefore, an equivalent dry mass of 1% of the wet mass was used. Finally, the pKa of the CNC was determined based on pH at the half-equivalence point according to the Henderson-Hasselbalch equation. For comparison, these results were plotted against a titration curve of 1mM NaOH against 1mM HCl.

$$Carboxyl\ content\ (mmol/gCNC) = \frac{volume\ of\ 1mM\ NaOH\ to\ neutralize\ (CNC-BC)}{equivalent\ dry\ mass\ of CNC} \quad (2)$$

3.3 Results and Discussions

3.3.1 Microchannel device design and microbead production

The overall design of the microbead production method is shown below in Figure 3.2. It consists of a continuous phase (oil phase) flowing against a dispersed phase (PVA iron phase) and meeting at a junction, which is the site of the formation of microbeads comprised of the dispersed phase solution. The microbeads are subsequently dropped into a high pH (sodium hydroxide) solution where iron oxide precipitation occurs within the PVA matrix. Following this, thermal cycling is performed to induce physical crosslinking in the PVA.

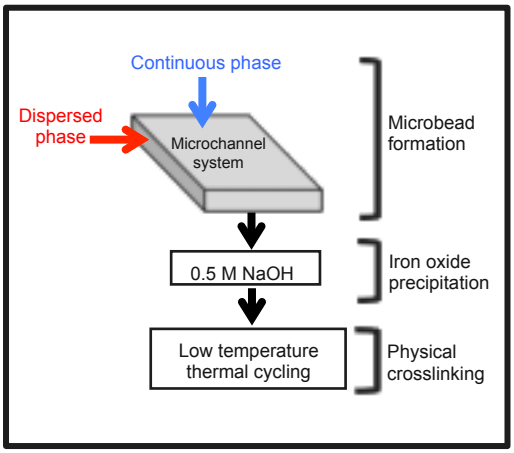

Figure 3.2 Production process for PVA iron oxide CNC microbeads.

Several designs were tested for the microchannel system used for production of 100-200µm diameter PVA iron oxide CNC microbeads. Initial designs using a T-junction microchannel configuration were used and results were unsatisfactory (details are collected in Appendix III). The final design selected made use of a flow-focusing

microchannel configuration (Figure 3.3). Dispersed phase (PVA iron phase) flow is directed through a channel by the continuous phase (oil phase) flowing from two directions. The two phases are forced through a small opening, causing a viscous stress action of the continuous phase on the dispersed phase [1]. This results in the pinch-off of the dispersed phase, forming droplets. Compared to a T-junction microchannel configuration, we found that the flow-focusing system minimized the interaction between the dispersed phase and the channel wall, thus preventing the formation of slugs – elongated droplets [2] – of the dispersed phase in the channel. Adherence of the dispersed phase to the wall inhibits bead production, and is a common issue [3]. The use of a flow-focusing system addresses this issue, with another option being the coating of channel walls to make it immiscible with the dispersed phase (ie. hydrophobic coating for an aqueous dispersed phase) [3].

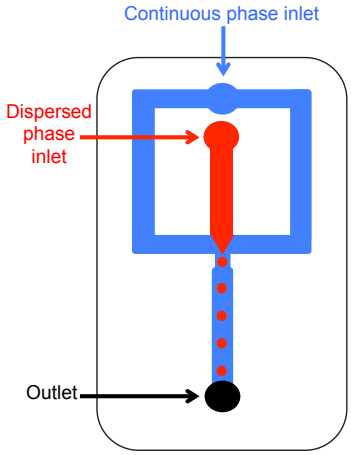

Figure 3.3 Flow focusing microchannel design. Red channel width is 200µm. Blue channels have a width of 500µm with a narrow section of 127µm.

Optimization of several key parameters was undertaken. Table 3.2 outlines the parameters and conditions that were varied. Under optimized conditions, the droplets of dispersed phase solution formed at the junction of the two phases was smaller than the width of the channel. This is consistent with reports that flow-focusing systems are advantageous in their ability to produce microparticles of smaller sizes relative to other channel configurations, such as the T-junction [4,5]. Images of the formation of a microbead at the junction of the PVA iron phase and the oil phase is shown in Figure

3.4. At the junction of the channels, the dispersed phase is constricted through the channel by the continuous phase, where droplets are formed.

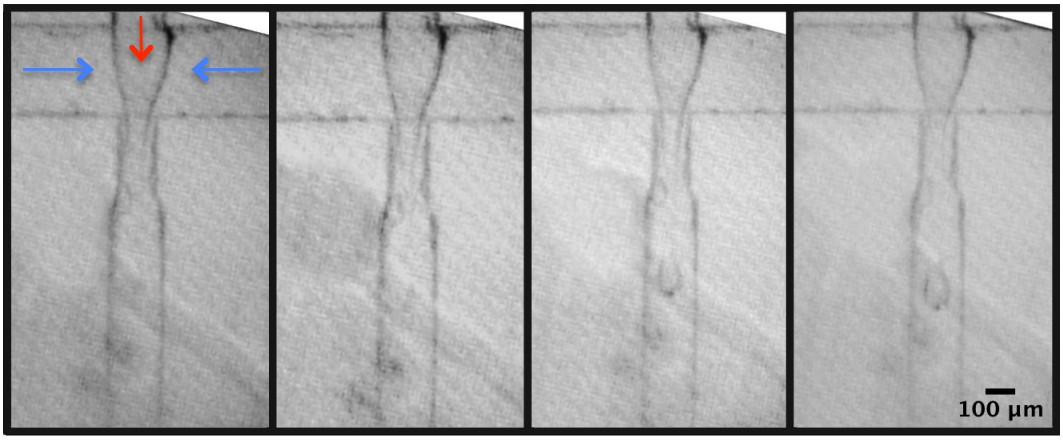

Figure 3.4 Microbead production using the flow-focusing microchannel design. The red arrow indicates flow of the dispersed phase (Table 3.1 solution 3) and the blue arrow indicates flow of the continuous phase (Table 3.2 continuous phase composition 5).

Table 3.2 Microbead production process variable parameters

Parameter	Conditions
Continuous phase composition	1. hexane 2. 1wt% Span80 in hexane 3. 1wt% Span80 + 49.5wt% mineral oil in hexane 4. undecane 5. 1wt% Span80 in undecane
Dispersed phase composition	See solutions 1-4 in Table 3.1
Flow rates	Continuous phase: 10-25mL/h Dispersed phase: 0.1-2mL/h
Collecting reservoir composition	1. 0.5M NaOH in water 2. 0.5M NaOH + 50v/v% ethanol in water
Collecting reservoir temperature	-20°C to room temperature

The most favourable conditions for reproducible production of 100-200µm diameter microbeads were found. A continuous phase composed of 1wt% Span80 in undecane (Table 3.2 continuous phase composition 5) was selected. This was chosen based on a

match in viscosity of the undecane. The interaction of the dispersed and continuous phases, based on viscosity and interfacial tension, is an important factor. It has been reported that selection of a more viscous continuous phase allows better droplet formation [3]. This is consistent with our findings, as continuous phases containing undecane were more effective than those containing hexane. The wetting property of the fluids with the microchannel wall is also an important parameter. We found that the use of Span80 surfactant allowed more effective bead production. Xu *et al.* used a similar microchannel system composed of PMMA, and found that with the addition of Span80 to the immiscible phase, the PMMA surface was converted from partially hydrophilic to completely hydrophobic. Based on this, they added 0.1-2wt% Span80 to a continuous oil phase to produce better droplets of a dispersed water phase using the microchannel system [6].

Optimal flow rates were also determined for our system. The continuous phase flow rate was maintained between 20 and 22mL/h and the flow rate of the dispersed phase was always kept at 1mL/h. These are similar flow rates to other work producing beads of a similar size range [6,7]. The collecting reservoir composition used was 0.5M NaOH in 50v/v% ethanol in water at room temperature.

3.3.2 Microbead characterization

Following iron oxide precipitation, bead collection, separation, and one FTC, images of the microbeads were taken, and an example is shown in Figure 3.5. It is clear that the shape of the microbeads is not spherical. This is suspected to result from the high viscosity of the solution used. The solidification process for the beads, involving iron oxide precipitation and reduced solubility of PVA in NaOH, is so fast that the beads retain a teardrop shape. Variations in the distance of the outlet tubing to the sodium hydroxide collecting reservoir as well as reservoir temperature did not result in a change in the microbead shape. The equivalent spherical diameter was calculated to be 111.4 ± 39.4μm.

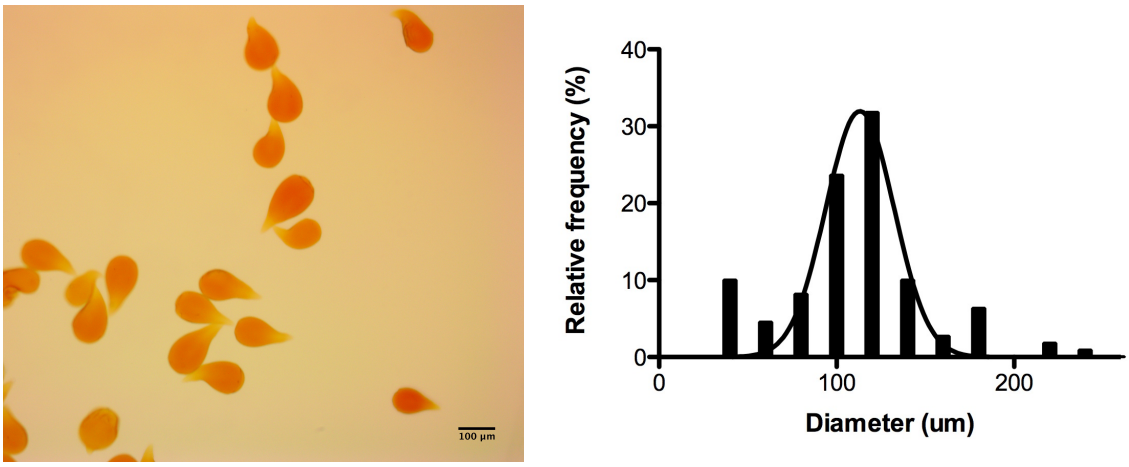

Figure 3.5 A) Optical image of microbeads fabricated using high iron PVA solution (Table 3.1 solution 2). B) Histogram of microbead equivalent spherical diameter fit to a Gaussian distribution.

The obtained microbead size is desirable for our application, as beads of around 100µm can be easily administered by catheter and microbeads in this size range have been shown to reach the distal portions of a tumour and adequately occlude the tumour vessels [8,9,10]. However, the uniformity of these particles could be improved. Although microfluidics is a favourable approach to accomplish the production of monodisperse particles, we see a range of the resulting microbead equivalent spherical diameters. This could be due to non-optimized materials comprising the microchannel device, which result in undesirable interactions with the dispersed or continuous phases. Alternatively, there may be need for further optimization of the solution used as the continuous phase.

The shape of the particles must also be considered. Some irregularly shaped embolization particles have been used, such as Contour™ PVA embolization particles [11], which indicates that the microbeads we have produced may be suitable. However, it has been suggested that spherical microparticles can reach more distal locations and result in a more complete blood vessel occlusion than irregular materials or material with irregular shape [12,13]. Nevertheless, the microbeads we have produced are uniformly shaped, as a droplet shape is consistently seen. These may perform better

than non-uniformly shaped particles. An additional argument for the use of uniformly shaped particles is a consistently calibrated drug loading [13]. We expect that drug loading consistency can be achieved for the microbeads produced here. Through the mechanism we propose for drug loading, which uses CNC to conjugate drug molecules, there exists the potential for highly uniform drug loading.

The successful production of microbeads comprised of PVA and iron oxide demonstrates the design, fabrication, and application of a flow-focusing microchannel system. To the best of our knowledge, this is the first report of microbeads of the current composition and dimension. Preparation of iron oxide containing PVA beads with a diameter of 2mm has been shown [14]. This was accomplished through the dropwise addition of iron salts and PVA solution into alkaline solution through the use of a syringe fitted with a needle. Although this method is simple and produces beads of uniform size, they are too large to be useful for most drug delivery applications and are significantly larger than DEBs. We attempted the approach described by Zhou *et al.* and were unable to reduce bead diameter to below 1mm. Even through the reduction of needle gauge size, beads of applicable dimension could not be produced as a result of the surface tension present in the solution dropping from the needle tip. Through this experience, we chose to pursue the use of a microchannel device for the preparation of 100-200μm diameter microbeads. Our approach using microfluidics is advantageous in its ability to produce small diameter microbeads.

CNC containing PVA iron oxide microbeads were also prepared using the flow-focusing microchannel. Conditions and procedure similar to that of the PVA iron oxide beads were used and the product microbeads are shown in Figure 3.6. With incorporation of CNC at 1wt% (Table 3.1 solution 3), we do not see a large difference in the morphology and size of the microbeads compared to microbeads without CNC. The average equivalent spherical diameter of the microbeads containing 1wt% CNC is 108.2 ± 41.4μm. There is no statistically significant difference in the equivalent spherical diameters of the beads without CNC compared to those containing 1wt% CNC. This suggests that at this loading of CNC, there are no major alterations in the preparation procedure, or disruption to the size and uniformity of the microbeads.

However, when a large increase in the CNC loading was attempted using a solution with 10wt% CNC (Table 3.1 solution 4), we saw a substantial increase in microbead size (~600μm) and there was difficulty in production. This suggests that there is an upper limit to the amount of CNC able to be incorporated using this approach for our desired size range. Increasing CNC loading is expected to increase the system viscosity, which may hinder formation of 100-200μm microbeads.

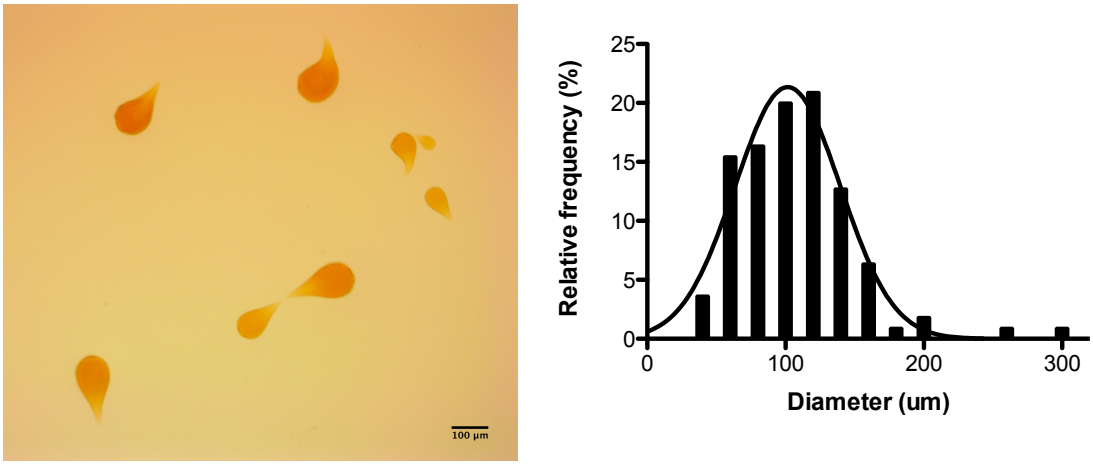

Figure 3.6 A) Optical image of microbeads fabricated using high iron PVA CNC solution (Table 3.1 solution 3). B) Histogram of microbead equivalent spherical diameter fit to a Gaussian distribution.

SEM was performed on microbeads and these images are shown below in Figure 3.7. Figures A and B display the whole collapsed beads, and Figures C and D illustrate the surface morphology of the microbeads. The difference in size compared to the measurements described above is a result of the dehydration process used prior to imaging. Shrinkage occurred due to the removal of water. EDX was performed on the microbead (Figure 3.8) and the results confirm the presence of iron as a component of the bead.

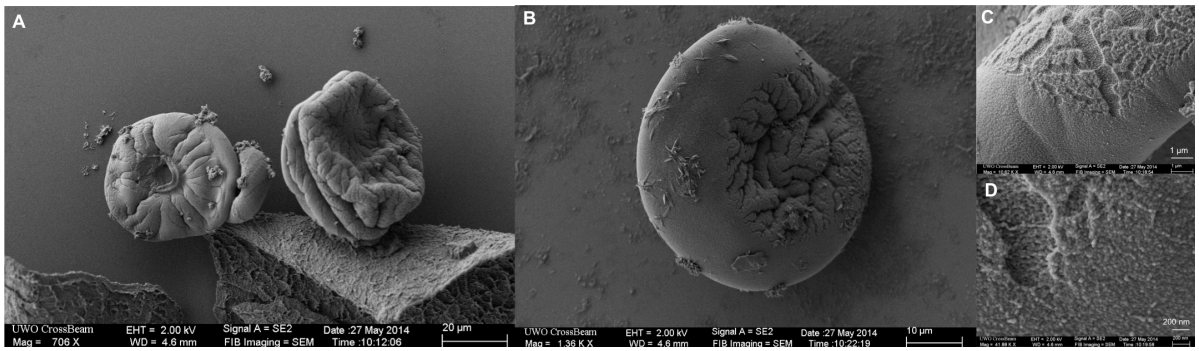

Figure 3.7 SEM images of PVA iron oxide microbeads of approximately 40µm diameter. Microbead size and shape is a result of the dehydration process. Figures A and B show whole beads and figures C and D display surface morphology.

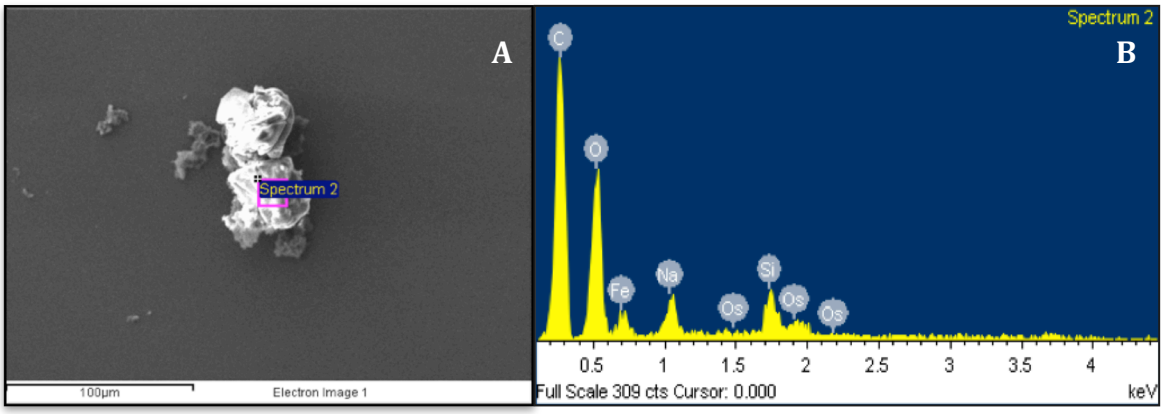

Figure 3.8 EDX spectrum of PVA iron oxide microbeads. A) Whole microbeads with a square specifying the location of EDX sampling. B) Spectrum indicating the presence of iron in the microbeads.

Transmission electron microscopy images were taken of microtomed microbead samples. The iron oxide nanoparticles are very clearly displayed (Figure 3.9). There are several important aspects to consider when interpreting this result. First of all, the size of the nanoparticles is important. For use as a magnetically targeted drug carrier or imaging contrast enhancement agent (MRI and CT), nanoparticles must have high magnetization values, size of less than 100nm, and a narrow particle size distribution [15]. The nanoparticles that we see in the PVA matrix were found have a mean diameter of 28.0 ± 20.6nm, which fit the size requirements (see Appendix IV for size

distribution). The large standard deviation is a result of some aggregates of two nanoparticles, and in rare cases, aggregates of more than two nanoparticles. Figure 3.10 shows examples of these aggregates. Although aggregation is minimal, the measured particle size and standard deviation is larger than it would be for only single nanoparticles due to the inclusion of aggregates in the size measurement.

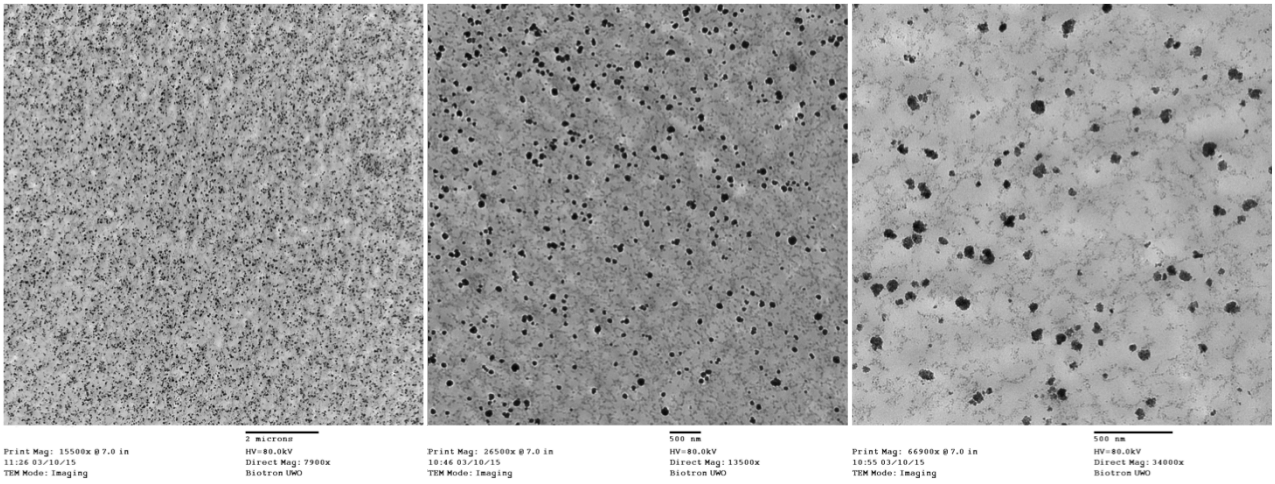

Figure 3.9 TEM of PVA iron oxide microbead interior.

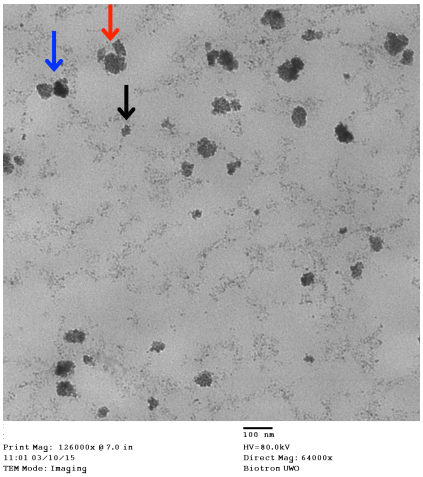

Figure 3.10 TEM of PVA iron oxide microbead interior. The black arrow indicates an individual iron oxide nanoparticle, the blue arrow indicates an aggregate of 2 nanoparticles, and the red arrow indicates an aggregate of multiple particles.

Secondly, and arguably of more importance, is the distribution of the iron oxide nanoparticles within the PVA matrix. Aggregation of iron oxide nanoparticles is a common problem that exists due to interactions between particles. When aggregates form, magnetic dipole-dipole attractions occur between them and ferromagnetic behavior results [16,17], which is less desirable than superparamagnetic behavior for biomedical applications. In our case, aggregation is not a serious problem.

The low level of iron oxide nanoparticle aggregation can be understood in terms of the particle formation process. In the current process, Fe^{2+} and Fe^{3+} are uniformly distributed in the matrix of the PVA microbeads. Iron oxide is formed by *in situ* precipitation within the liquid PVA hydrogel matrix by diffusion of NaOH into it. The viscosity of the PVA solution hinders the movement of the iron oxide nuclei and limits their growth. As the PVA beads are solidified using the LTTC process, the iron oxide nanoparticles are immobilized in space within the hydrogel matrix of the microbeads, leading to the small size and low level of aggregation observed. The clusters of multiple nanoparticles are most likely formed by nucleation independently, due to local concentration fluctuations of iron chlorides, rather than due to an aggregation process.

Coating of iron oxide nanoparticles with PVA has been reported in the literature to result in monodisperse particles without aggregation [15,18,19], and the PVA acts as a stabilizing agent in ferrofluids [20]. In one study where iron oxide precipitation was completed in aqueous PVA, it was suggested that PVA can bind irreversibly to the magnetite surface [21]. In work by Gonzalez *et al.*, magnetite nanoparticles of less than 50nm in size were produced in PVA films through a similar process – the co-precipitation of iron salts in PVA followed by physically crosslinking. Low levels of aggregation were also observed. It was hypothesized that adsorption of PVA to the magnetite surface through the interaction of the PVA hydroxyl groups with iron oxide controls the growth and aggregation of nanoparticles [22].

To characterize the nature of the iron oxide nanoparticles, XRD was performed on a dried microbead sample made form the high iron PVA CNC solution (Table 3.1 solution 3). The low signal to noise ratio of the XRD pattern shown in Figure 3.11A is

due to the limited sample size used. Since PVA is a polymer of limited degree of crystallinity, its XRD pattern is more ill defined and stretches over a broad 2θ range. This also limits the signal to noise ratio and identification of other Fe_3O_4 diffraction peaks. However, certain characteristic peaks are visible, which justifies the presence of PVA and iron oxide in the form of magnetite (Fe_3O_4). The diffraction peak corresponding to Fe_3O_4 can be identified by comparing to a standard XRD pattern for magnetite (International Centre for Diffraction Data (ICCD) card number 00-019-0629 from PDF-4+ software) (Figure 3.11B). Additional information is presented in Appendix II. The most intense peaks for magnetite occur at 2θ values of 35°, 41°, and 74°. In the XRD for the microbeads produced in this work (Figure 3.11A), we see a significant peak occurring at 22°, which corresponds to PVA, consistent with our data in section 4.3.1 (Figure 4.2) and literature reports [23,24]. There are also three main peaks at 33°, 41°, and 74°, consistent with characteristic magnetite peaks. There is slight shift in location and relative intensity of the first peak, at 33°, compared to the standard magnetite sample, at 35°. This is probably due to the small sample size, resulting in a highly noisy pattern. Alternatively, there may be slight change in the crystal structure of the iron oxide in the microbeads compared to a standard magnetite curve. However, we compared the microbead diffraction pattern to that of another possible resulting form of iron oxide – maghemite – and the peaks do not align. Given the proximity of the microbead diffraction peaks to a standard magnetite pattern, we can conclude that magnetite is likely the form of iron oxide present. Microbead production using a similar method is consistent with this result [14]. Furthermore, our results coming up in section 4.3.1 for a film of the same composition very clearly illustrate the presence of magnetite. No specific peak is detected for CNC because the relative composition is very low.

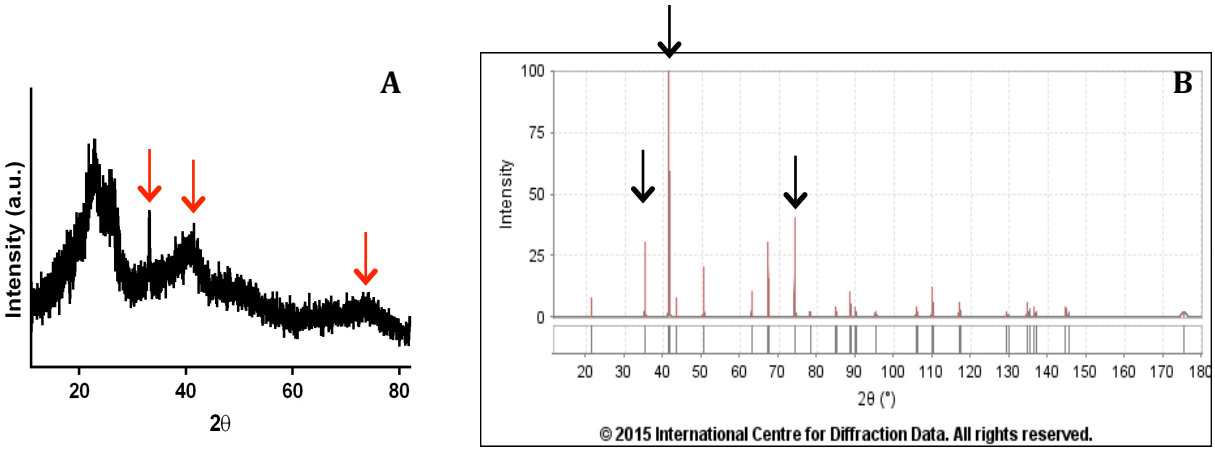

Figure 3.11 A) XRD pattern of PVA iron oxide CNC microbeads. B) ICCD card for magnetite (number 00-019-0629).

Magnetite occurs in an inverse spinal structure with both ferrous and ferric ions and oxygen. Magnetite, depending on nanoparticle size, is superparamagnetic, meaning that it does not retain magnetism after the magnetic field is removed. The presence of iron oxide nanoparticles in the form of magnetite is promising for future work in magnetic targeting of these microbeads or use in magnetic resonance imaging. Zhou *et al*. demonstrated that the 2mm PVA iron oxide beads they produced had superparamagnetic properties [14]. Vibrating sample magnetometer measurements were attempted on our microbead samples, but due to sample size limitations, reliable results could not be obtained. Instead, we investigated the effect of an external magnetic field on these microbeads.

In the presence of a strong magnet, we are able to visually demonstrate the magnetic properties of the beads. Microbeads composed of high iron PVA CNC solution (Table 3.1 solution 3) were suspended in PBS and an external magnetic field was applied using a strong permanent magnet. Images were taken of the microbeads movement towards the permanent magnet and their settling upon removal of the magnetic field as shown in Figure 3.12. Qualitatively, this demonstrates the ability to mobilize and locate the microbead using an external magnetic field. Further work in this area should be completed to better investigate magnetic properties as there could be great potential for this system to be used for magnetic localization.

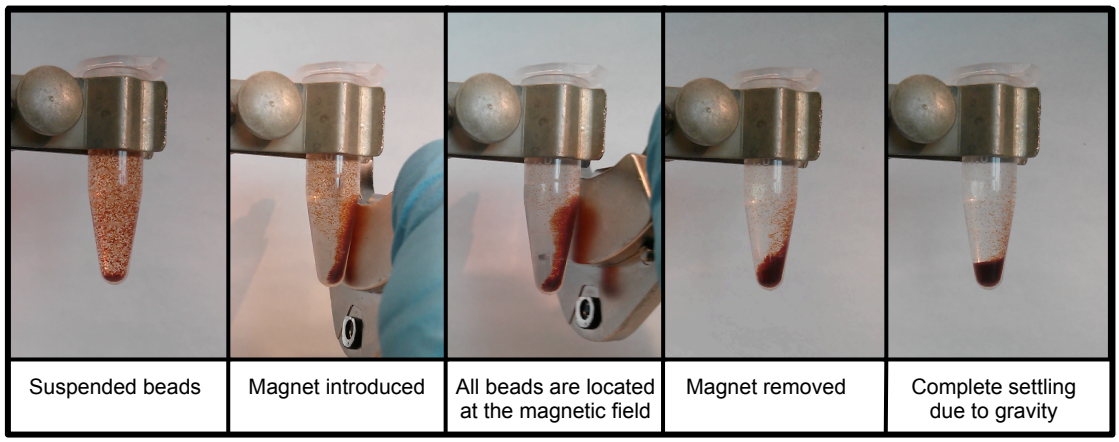

Figure 3.12 Movement of PVA iron oxide microbeads towards a permanent magnet.

3.3.3 Microbead visualization

The ability to visualize this class of microbead using clinical CT was demonstrated on beads of low iron oxide loading in PVA (Table 3.1 solution 1). Microbeads were placed in PBS solution in tubes and imaged. What can be seen in Figure 3.13A is suspension containing a small quantity of microbeads at the bottom of the tube. The 40mg quantity of beads is understandably more visible than 20mg of beads, due to the presence of a greater amount of Fe_3O_4-containing particles. However, it is difficult to detect the enhanced contrast in either sample. Figure 3.13B is the same image processed using different settings of the window width and level of the CT machine. At this contrast and sensitivity, we are better able to visualize the presence of the higher contrast microbeads at the bottom of the tubes. However, this contrast is weak, and unlikely to be sufficient for practical use, as the microbeads appear very similar to the PBS control, even when accumulated at the base of the tube. In order to enhance the contrast, a larger quantity of iron was added to the solution for microbead preparation.

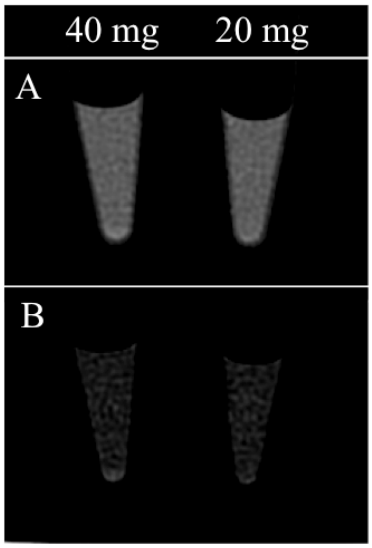

Figure 3.13 CT images of low iron PVA microbeads at quantities of 40 and 20 mg. A) and B) represent different window/level settings of the CT machine (W/L of 650/100 (A) and 426/183 (B)).

Subsequent CT experiments were performed using microbeads of the higher iron oxide loading and containing CNC (Table 3.1 solution 3). These beads, at loading levels of 11-50mg in PBS, were imaged using CT. Results are shown in Figure 3.14A. Since cellulose is of similar elemental composition as PVA, it is not expected to contribute to any CT contrast. At similar bead loadings, an enhanced contrast can clearly be seen compared to the microbeads shown in Figure 3.13. The amount of iron loading in microbeads is an important factor in the level of visibility, and at the higher concentration of iron, we are able to see increased contrast. The samples in Figure 3.14B contain the same quantities of sample, but are plain PVA samples containing no iron oxide, and used as a control. We are not able to visualize any contrast enhancement in these samples thus confirming the positive effect of iron oxide in CT imaging. It can be concluded that the PVA iron oxide CNC microbeads provide improved visualization compared to plain PVA samples and that greater amounts of iron result in greater contrast.

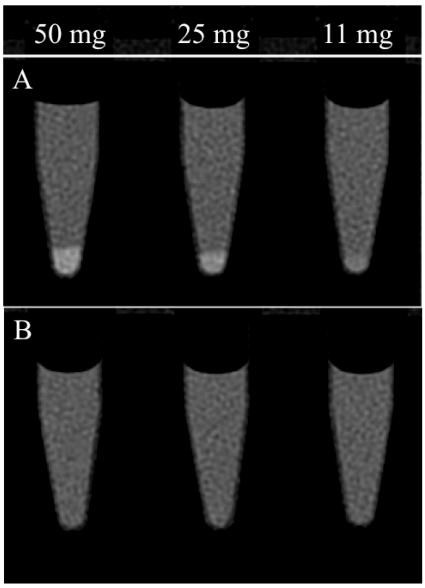

Figure 3.14 CT images of 50, 25 and 11mg quantities of sample. A) Tubes contain microbeads fabricated using the high iron PVA CNC. B) Tubes contains control samples of plain PVA. (W/L of 650/100).

Figure 3.14 illustrates the ability to detect the high iron PVA CNC microbeads relative to PBS under CT. The lowest quantity of beads does become harder to differentiate from the fluid, which leads to the conclusion that some accumulation of beads is necessary to result in a high enough contrast for adequate detection. For clinical applications in TACE therapy, 1-4mL of microbeads is typically used [11]. For volumes such as this, and given that accumulation of beads does occur, the level of contrast enhancement we are seeing from small quantities of beads may be appropriate. Of course, work demonstrating the use of these microbeads *in vivo* would need to be completed to properly assess this. Not only is PBS not equivalent to tissue, but also, the level of accumulation of beads in the vasculature is an important factor in determining whether these microbeads would be visible. Nevertheless, the ability to detect these microbeads in PBS using CT has been demonstrated, and this preliminary work encourages further studies using this system.

In the imaging of Lipodiol-loaded PVA microspheres with CT, the researchers were able to demonstrate the ability to visualize beads in the terminal location of swine liver after injection of 0.2mL of packed beads, with increased visualization after additional 0.2mL increments up to 1mL [25]. These quantities are comparable to the amounts we have imaged. However, *in vivo* detection is very different than *in vitro* detection and we expect to require a much greater amount of beads to provide enough contrast to visualize microbeads within tumour tissue due to the higher X-ray attenuation of tissue [26].

An important note about the microbeads we have fabricated is that they are also expected to be visible in MRI, as superparamagnetic nanoparticles provide high contrast due to enhanced proton relaxation [27]. It would be useful to image the beads under MR and compare this to CT results. Depending on the quantity of accumulated microbeads in tissue vasculature, one of these imaging modalities might prove to be more useful. Alternatively, the ability to image these microbeads using multiple imaging modalities may make them desirable candidates for use in investigation of microbead distribution in tumour sites, or for the visualization of the therapeutic delivery process.

3.3.4 Cellulose nanocrystal characterization

The proposed multifunctional microbead system outlined in this thesis involves the use of CNC as a nanocarrier for therapeutic molecules. A necessary step in the use of CNC for drug conjugation is its functionalization and the quantification of the functionalized group. Through a hydrolysis reaction using hydrogen peroxide to break down bacterial cellulose into cellulose nanocrystals, the conversion of the hydroxyl groups to carboxylic acid groups has been demonstrated [28]. The carboxylic acid group will serve as the site for drug conjugation through ionic association for a chemotherapeutic molecule such as Dox. Conditions for and amount of drug conjugation is dependent on the concentrations of carboxylic acid groups and its pKa. These were determined for the CNC samples we used by titration.

The titration curve for CNC (Figure 3.15) illustrates a right-shifted curve relative to the control sample and the BC sample. The carboxyl content calculated using Equation 2 was found to be 8.36 ± 0.56mmol/g CNC, which is substantially higher than similar previous work. Spaic reported a carboxyl content of 1.13 ± 0.02mmol/g BC following a TEMPO-mediated oxidation, and Cook reported a carboxyl content of 0.97 ± 0.18mmol/g CNC using a hydrogen peroxide reaction similar to our work [28]. Other work, on oxidized cotton derived cellulose, demonstrated an even lower carboxyl content of 0.7mmol/g [29]. The level of carboxylic group we determined is one of the highest reported, which is beneficial for maximum drug loading.

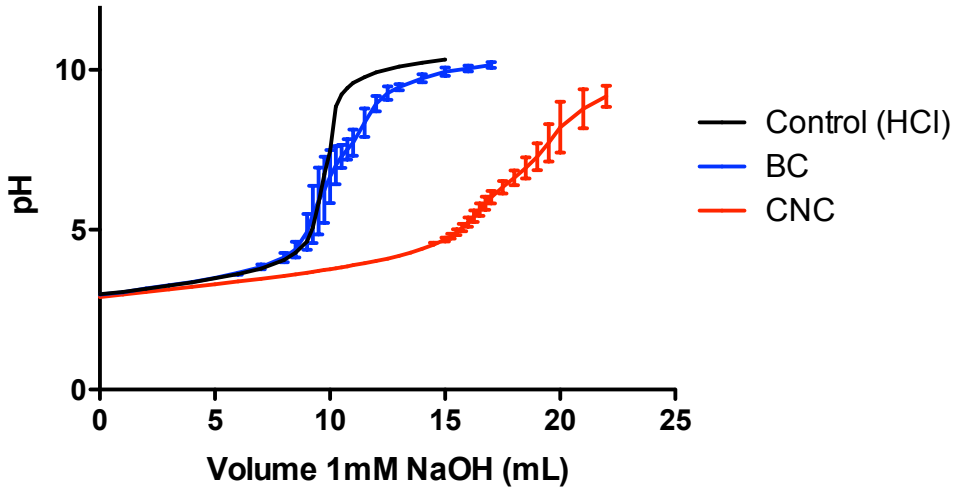

Figure 3.15 Titration of 0.1g BC and CNC in 1mM HCl with 1mM NaOH.

The pKa of CNC was found to be 3.71, which is comparable to that of other carboxylic acid groups (formic acid has a pKa of 3.76, and acetic acid has a pKa of 4.74 [30]). Similar work completed on the oxidation of cellulose report pKa values at 3.90 for BC [31], and 2.96 for CNC [28]. At appropriate loading conditions, CNC with a pKa in this range will be able to able to ionically conjugate drug molecules such as as Dox, with a pKa of 8.3 [32].

We have developed a system that under appropriate conditions, will be able to load drug molecules such as doxorubicin to the CNC surface. The release mechanism of drug molecules from the microbead would not only rely on ionic dissociation of the drug from the CNC, but also diffusion out of the microbead. Based on what has been

described in section 2.5.1, the diffusion of drug molecules from the PVA matrix can be controlled through alterations in the processing conditions. For example, if a slow drug release is desired, additional FTCs can be performed to the microbeads after drug loading. Release rate and profile from this system can thus be tailored for specific applications.

3.4 Conclusions

In this chapter, we have demonstrated the ability to produce PVA iron oxide CNC microbeads through a microfluidic system consisting of a flow-focusing microchannel. Beads were produced in the desired size range of roughly 100μm equivalent spherical diameter. The microbead material has been characterized in terms of structure and morphology, and the presence of iron in the form of iron oxide, specifically magnetite, has been demonstrated. Microbeads have been shown to have monodisperse iron oxide nanoparticles embedded, which impart magnetic properties to the material and also allows for visualization with CT. Microbeads composed of CNC and a high iron oxide content in PVA are detectable under CT at microbead quantities between 11 and 50mg. Successful functionalization of CNC with a high carboxyl content has been demonstrated, showing the potential for drug delivery.

References

[1] J. Wang, J. Wang and J. Han. 2011. Fabrication of advanced particles and particle-based materials assisted by droplet-based microfluidics. *Small*. **7**(13): 1728-1754.

[2] B. Hallmark, C. Parmar, D. Walker, C. H. Hornung, M. R. Mackley and J. F. Davidson. 2009. The experimental observation and modelling of microdroplet formation within a plastic microcapillary array. *Chem. Eng. Sci.* **64**(22): 4758-4764.

[3] S. Teh, R. Lin, L. Hung and A. P. Lee. 2008. Droplet microfluidics. *Lab Chip*. **8**(2): 198-220.

[4] A. R. Abate, S. Seiffert, A. S. Utada, A. Shum, R. Shah, J. Thiele, W. J. Duncanson,A. Abbaspourad, M. H. A. Lee, I. D. Lee *et al*. 2007. Microfluidic techniques for synthesizing particles. Available at: http://weitzlab.seas.harvard.edu.proxy1.lib.uwo.ca/publications/Bookchapter_Microfluidic_techniques.pdf. Accessed March 3, 2013.

[5] R. K. Shah, H. C. Shum, A. C. Rowat, D. Lee, J. J. Agresti, A. S. Utada, L. Chu, J. Kim, A. Fernandez-Nieves, C. J. Martinez *et al*. 2008. Designer emulsions using microfluidics. *Mater. Today* **11**(4): 18-27.

[6] J. H. Xu, S. W. Li, J. Tan, Y. J. Wang and G. S. Luo, 2006. Controllable preparation of monodisperse O/W and W/O emulsions in the same microfluidic device. *Langmuir*. **22**(19): 7943-7946.

[7] T. Nisisako, T. Torii, and T. Higuchi. 2002. Droplet formation in a microchannel network. *Lab Chip*. **2**(1): 24-26.

[8] M. R. Dreher, K. V. Sharma, D. L. Woods, G. Reddy, Y. Tang, W. F. Pritchard, O. A. Chiesa, J. W. Karanian, J. A. Esparza, D. Donahue *et al*. 2012. Radiopaque drug-eluting beads for transcatheter embolotherapy: Experimental study of drug penetration and coverage in swine. *J. Vasc. Interv. Radiol.* **23**(2): 257-264.

[9] K. Lee, E. Liapi, J. A. Vossen, M. Buijs, V. P. Ventura, C. Georgiades, K. Hong, I. Kamel, M. S. Torbenson and J. H. Geschwind. 2008. Distribution of iron oxide-containing embosphere particles after transcatheter arterial embolization in an animal model of liver cancer: Evaluation with MR imaging and implication for therapy. *J. Vasc. Interv. Radiol.* **19**(10): 1490-1496.

[10] R. Martin, J. Irurzun, J. Munchart, I. Trofimov, A. Scupchenko, C. Tatum and G. Narayanan. 2011. Optimal technique and response of doxorubicin beads in hepatocellular cancer: Bead size and dose. *Kor. J. Hepatol.* **17**(1): 51-60.

[11] A. L. Lewis and R. R. Holdon, 2011. DC Bead embolic drug-eluting bead: clinical application in the locoregional treatment of tumours. *Expert Opin Drug Del*. **8**(2): 153-169.

[12] P. Flandroy, C. Grandfils, J. Collignon, A. Thibaut, N. Nihant, S. Barbette, R. Jerome and P. Teyssie. 1990. Polylactide microspheres as embolic agent: A preliminary-study. *Neuroradiology* **32**(4): 311-315.

[13] P. Giunchedi, M. Maestri, E. Gavini, P. Dionigi and G. Rassu. 2013. Transarterial chemoembolization of hepatocellular carcinoma agents and drugs: An overview, part two. *Expert Opin. Drug Deliv.* **10**(6): 799-810.

[14] L. Zhou, B. He and F. Zhang. 2012. Facile one-pot synthesis of iron oxide nanoparticles cross-linked magnetic poly(vinyl alcohol) gel beads for drug delivery. *ACS Appl. Mater. Interfaces* **4**(1): 192-199.

[15] S. Laurent, D. Forge, M. Port, A. Roch, C. Robic, L. V. Elst and R. N. Muller. 2008. Magnetic iron oxide nanoparticles: Synthesis, stabilization, vectorization, physicochemical characterizations, and biological applications. *Chem. Rev.* **108**(6): 2064-2110.

[16] A. Gupta and M. Gupta. 2005. Synthesis and surface engineering of iron oxide nanoparticles for biomedical applications. *Biomaterials* **26**(18): 3995-4021.

[17] S. Singamaneni, V. N. Bliznyuk, C. Binek and E. Y. Tsymbal. 2011. Magnetic nanoparticles: Recent advances in synthesis, self-assembly and applications. *J. Mater. Chem.* **21**(42): 16819-16845.

[18] M. Mahmoudi, A. Simchi and M. Imani. 2009. Cytotoxicity of uncoated and polyvinyl alcohol coated superparamagnetic iron oxide nanoparticles. *J. Phys. Chem. C* **113**(22): 9573-9580.

[19] M. Mahmoudi, S. Sant, B. Wang, S. Laurent and T. Sen. 2011. Superparamagnetic iron oxide nanoparticles (SPIONs): Development, surface modification and applications in chemotherapy. *Adv. Drug Deliv. Rev.* **63**(1): 24-46.

[20] X. Qiu and F. Winnik. 2000. Preparation and characterization of PVA coated magnetic nanoparticles. *Chin. J. Polym. Sci.* **18**(6): 535-539.

[21] J. Lee, T. Isobe and M. Senna. 1996. Preparation of ultrafine Fe3O4 particles by precipitation in the presence of PVA at high pH. *J. Colloid Interf. Sci.* **177**(2): 490-494.

[22] J. S. Gonzalez, C. E. Hoppe, D. Muraca, F. H. Sanchez and V. A. Alvarez. 2011. Synthesis and characterization of PVA ferrogels obtained through a one-pot freezing-thawing procedure. *Colloid Polym. Sci.* **289**(17): 1839-1846.

[23] R. Ricciardi, F. Auriemma, C. De Rosa and F. Laupretre. 2004. X-ray diffraction analysis of poly(vinyl alcohol) hydrogels, obtained by freezing and thawing techniques. *Macromolecules* **37**(5): 1921-1927.

[24] R. Ricciardi, F. Auriemma, C. Gaillet, C. De Rosa and F. Laupretre. 2004. Investigation of the crystallinity of freeze/thaw poly(vinyl alcohol) hydrogels by different techniques. *Macromolecules* **37**(25): 9510-9516.

[25] K. V. Sharma, M. R. Dreher, Y. Tang, W. Pritchard, O. A. Chiesa, J. Karanian, J. Peregoy, B. Orandi, D. Woods, D. Donahue, *et al*. 2010. Development of

"imageable" beads for transcatheter embolotherapy. *J. Vasc. Interv. Radiol.* **21**(6): 865-876.

[26] J. T. Bushberg. 2012. *The essential physics of medical imaging*. Wolters Kluuwer Health/Lippincot Williams and Wilkins.

[27] A. Akbarzadeh, M. Samiei and S. Davaran. 2012. Magnetic nanoparticles: Preparation, physical properties, and applications in biomedicine. *Nanoscale Res. Lett.* **7**(1): 1-13.

[28] J. Cook. 2013. *Amine functionalization of bacterial cellulose for targeted delivery applications*. Dissertation/Thesis: The University of Western Ontario.

[29] T. Saito, S. Kimura, Y. Nishiyama, and A, Isogai. 2007. Cellulose nanofibres prepared by TEMPO-mediated oxidation of native cellulose. *Biomacromolecules*. **8**(8): 2485-2491.

[30] L. G. Wade. 2011. *Organic Chemistry.* Prentice Hall.

[31] M. Spaic. 2011. *Functionalized bacterial cellulose for controlled release and delivery*. Dissertation/Thesis: The University of Western Ontario.

[32] J. D. Adams. 2005. The impact of tumor physiology on camptothecin-based drug development. *Curr. Med. Chem.* **5**(1): 1-13.

CHAPTER 4 – 'Degradable' PVA Iron Oxide Hydrogel

4.1 Introduction

In this chapter, we explore the use of iron oxide nanoparticle formation in PVA as a crosslinking method in conjunction with physical crosslinking achieved using low temperature thermal cycling. Gonzalez *et al.*'s work on PVA iron oxide gels formed through low temperature thermal cycling of PVA, followed by the addition of iron ions and subsequent precipitation into iron oxide demonstrated that the PVA iron oxide gel had increased degree of crystallinity and melting point [1]. This provides evidence that iron oxide contributes to crosslinking within the PVA hydrogel. We hypothesized that the removal of iron from PVA iron oxide hydrogels will reduce the crosslinking, and therefore stability, of the material, allowing dissolution to occur. Dissolution studies were performed on bulk hydrogel material and the dissolution was compared for films in solutions of varying pH and in the presence of iron chelating agents. Iron release and mass loss data was collected, as well as mechanical testing data. This work demonstrates the ability of this biomaterial to 'degrade' over time, which may be very advantageous for drug delivery and embolization purposes. The importance of this work extends to other areas of research involving the use of stimulus-responsive hydrogels, such as tissue engineering.

4.2 Materials and methods

All chemicals used were ACS reagent grade and purchased from Sigma-Aldrich (St. Louis, MO, USA). Distilled water was used for all experiments.

4.2.1 Solution preparation

Composition of the solution used was the high iron PVA content (Table 3.1 solution 2) as listed in chapter 3. The preparation procedure was as detailed in the material and methods section in chapter 3 (section 3.2.1). A 5wt% PVA solution was used as a control.

4.2.2 Hydrogel film fabrication

The solution was poured into moulds (Buna-N rubber) with rectangular openings (10cm by 5cm by 0.2cm) sandwiched between sheets of Teflon. The Teflon sheets were held between aluminum sheets and screwed together to ensure the moulds were tightly sealed. The moulds were placed in a water bath for 6 thermal cycles from 20°C to -20°C to 20°C at 0.1C/min, with one holding hour at the temperature limits. Subsequently, films were removed from the moulds and submerged in a 0.5M NaOH solution for 24 hours. Films were removed and then submerged in water for a day with constant replacing of the water until the pH reached neutral. Films were then cut into 5mm by 5mm strips and wrapped in plastic wrap and sealed.

4.2.3 X-ray diffraction

Films were dried at 60°C overnight and crushed using mortar and pestle with liquid nitrogen. XRD was performed using a Rigaku-Rotaflex Diffractometer (RU-200BH) with a Co-kα radiation (λ =1.79 Å) at 30kV and 44mA. Spectra with a 2θ diffraction angle were scanned from 0° to 82° with a 0.2° step size. The PVA iron oxide film was loaded onto a glass slide and the PVA film was loaded onto a glass slide with double-sided tape. A background scan was performed on the blank slide with tape, and the relative peaks were subtracted from the sample peaks of the applicable sample. Spectra were plotted from a 2θ of 10° to 82°.

4.2.4 Iron release quantification

Films were removed from the plastic wrap and each sample was weighed. Samples were placed into 3mL of solutions of water at pH 6, hydrochloric acid (HCl) adjusted to a pH of 2, or a 0.05M ethylenediametetraacetic acid disodium salt (EDTA) solution, all at room temperature. After a given amount of time, the sample was removed from solution and put into new solution. Solutions were analyzed for iron content using atomic absorption spectroscopy (AAS) (Varian Spectra AA 55) with a multi-element lamp (Fe/Co/Ni/Mn/Cu/Cr Varian Spectra AA Lamp) at a wavelength of 248.3 nm. The absorbance was converted into a concentration using a calibration curve of iron

standard solution (Fluka, Sigma Aldrich) created at the time of each sampling. Concentration was converted into a mass by multiplying by the volume of the solution. This was plotted as a fraction of the initial sample mass. This was repeated at various time points over 101 days and iron release was plotted against time.

4.2.5 Mass loss quantification

At each time point, when the PVA iron oxide film sample was removed from solution, it was blotted to remove excess liquid, and weighed. The mass loss was plotted against time. Mass loss was calculated using the following equation.

$$Mass\ loss\ (\%) = \frac{m_i - m}{m_i} \times 100 \quad (3)$$

where m_i is the initial sample mass and m is the mass of the sample at a given time point. The first time point of the film mass loss in EDTA solution was excluded because an increase in mass occurred due to swelling. This is to be expected as a result of some initial rehydration after the film processing, and was not included in mass loss data.

4.2.6 Mechanical testing

Tensile testing was completed on film samples to analyze the effect of iron oxide precipitation in terms of crosslinking the PVA matrix, as well as the removal of iron oxide. Films both before and after submergence in sodium hydroxide were tested. Briefly, samples of film were cut into 10mm by 25mm strips. Four different types of materials were tested: 1) PVA with iron chlorides after 6 FTCs (before iron oxide precipitation); 2) PVA with iron oxide after 6 FTCs and iron oxide precipitation; 3) PVA with iron oxide after 6 FTCs and after being treated in EDTA for 2 days; and finally, 4) PVA with iron oxide after 6 FTCs and after being treated in EDTA for 4 days.

Tensile testing was performed using a hydraulically powered material testing system (MTS Bionix 858). A 1kg load cell and an attachment for sample loading was used. The sample thickness was measured using a custom-designed Mitutoyo gauge thickness tester with samples fit into grooves in aluminum block to prevent deformation.

Samples were held in a custom-designed tissue grip set with a distance of 20mm between the two grips. Uniaxial tensile tests were performed at a strain rate of 4mm/s using a 16mm ramp (constant strain) with a sampling rate of 5kHz. Samples were subjected to preconditioning prior to testing. This is standard procedure for the purpose of removing any residual stresses in the material. 10 cycles of preconditioning using a sine wave with 3.5mm amplitude was used.

Raw data was converted into stress and strain and subsequently plotted. Some negative stress values resulted and this could be due to several factors. First of all, the samples used in this work are weak, and because there is noise generated due to the dead weight of the load cell and sample attachment piece, the data at low strain values may be partially a result of this noise. This may also be due to the acceleration of the equipment from 0 to 4mm/s. Some time is required for the machine to respond and accelerate, and so initial points on the curve may not be accurate. Finally, due to the sample non-uniformity as a result of iron oxide incorporation and release, the stress experienced does not necessarily follow a predictable trend. For these reasons, negative stress values were not used in the fitted curves.

Stress-strain data was also converted into elastic modulus at given strain values by taking the derivative of the stress-strain function. Statistical analysis was performed using a one-way ANOVA with a Tukey's post hoc test, and a p-value of <0.05 was considered significant (GraphPad Prism).

4.3 Results and Discussion

In order to study the dissolution of this material, films were produced rather than microbeads, as adequate amounts of sample were better able to be produced, and more reliable measurements could be made. However, the trends seen in this section of the work are expected to be applicable to the material we have proposed as a multifunctional visualization and delivery system. One main difference in the processing of the material was implemented – the number of FTCs was increased to 6 and this was performed before iron oxide precipitation through exposure to a sodium hydroxide bath. This was due to the challenges in handling the material as some level

of physical crosslinking is necessary to maintain the dimensional stability of the hydrogel.

4.3.1 Film characterization

After 6 FTCs, 5% PVA solutions containing iron chlorides resulted in a yellow film (Figure 4.1A). Following the submergence in a sodium hydroxide bath, the film turned black in colour (Figure 4.1B).

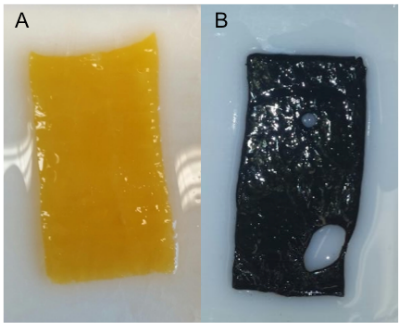

Figure 4.1 Films after 6 FTC. A) PVA iron chlorides film (prior to submergence in NaOH). B) PVA iron oxide film (after submergence in NaOH).
(Note: these films are from separate samples).

XRD of the PVA iron oxide film was performed and compared to a film of plain 5% PVA (Figure 4.2A). A peak occurring at a 2θ of 22° can be seen in the plain PVA sample. This is in agreement with other reported data [2,3]. In the PVA iron oxide sample, the same peak for PVA is displayed, as well as peaks for iron oxide in the form of magnetite (Fe_3O_4). Besides the same PVA peak at 22°, six characteristic peaks are evident, occurring at 35°, 41°, 50°, 63°, 67° and 74°. The peaks and their relative intensities are consistent with the standard XRD pattern of Fe_3O_4 shown in Figure 4.2B (ICCD card 00-019-0629 from PDF-4+ software).

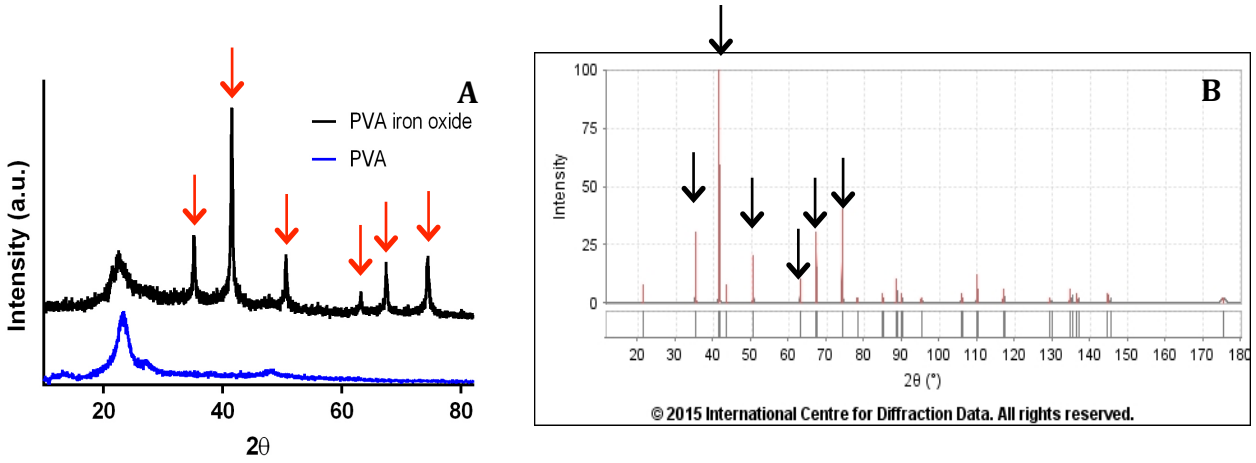

Figure 4.2 A) XRD pattern of PVA films and PVA iron oxide films. B) ICCD card for magnetite (number 00-019-0629),

4.3.2 Iron release

The release of iron from the PVA iron oxide hydrogel was studied in release media containing EDTA (0.05M), HCl (pH 2) and water (pH 6) at room temperature. The cumulative release of iron over time is displayed in Figure 4.3. It is evident that the environmental parameters, namely presence of iron chelators and the pH of the solution surrounding the material, has a significant effect on the rate and quantity of iron released. A lower pH resulted in a greater release of iron, which is to be expected as a result of iron oxide solubilization. Furthermore, in the presence of EDTA, a chelating agent, a much greater amount of iron is released. The low pH (4.43) of the 0.05M EDTA solution as well as the ability of EDTA to extract and solubilize iron oxide can explain our observation. In water at pH 6, we see very little release of iron with only a 0.02 ± 0.003wt% release occurring after just over 100 days.

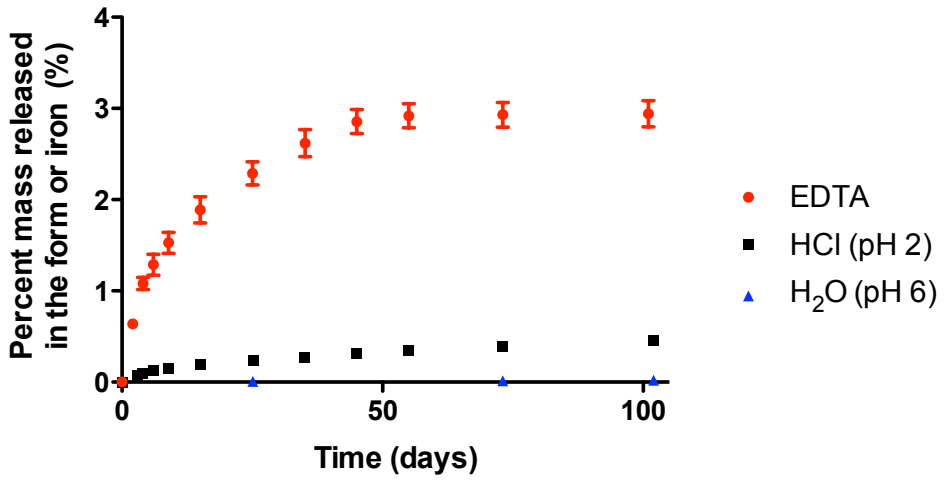

Figure 4.3 Cumulative iron released from PVA iron oxide films (as a percent of initial sample mass) over 100 days in solutions of EDTA solution, HCl solution, and H_2O.

To better understand the mechanism of iron release from the material, we investigate models studied for drug or solute release. A diffusion model for release of drug molecules or solutes from a thin film has been developed according to Fick's second law. Equation 4 is the early time approximation for diffusion-controlled release [4].

$$\frac{M_t}{M_\infty} = 4\left(\frac{Dt}{\pi l^2}\right)^{\frac{1}{2}} \; for \; 0 \leq \frac{M_t}{M_\infty} \leq 0.6 \tag{4}$$

M_t is amount of solute released at t, M_∞ is the total amount of solute loaded, t is time, D is the diffusion coefficient, and l is the thickness of the matrix.

The system studied in this work was prepared as a film, so the thin film model can be applied. Since the total amount of solute loaded (M_∞) is unknown, this model cannot be used to its full extent. We are not able to determine D, the diffusion coefficient. However, Equation 4 can be rearranged to the give Equation 5. It can be seen that the release amount over time (M_t) is proportional to the square root of time.

$$M_t = \left(\frac{4M_\infty D^{\frac{1}{2}}}{\pi^{\frac{1}{2}} l}\right) t^{\frac{1}{2}} \tag{5}$$

Accordingly, a plot of the cumulative release versus the square root of time was made for the release in all three media (Figure 4.4). In Figure 4.4, the data correlates linearly

for the iron release in HCl and H_2O solutions with R^2 values of 0.997 and 0.955 respectively. For the iron release in EDTA, only the initial section ($\frac{M_t}{M_\infty} \leq 0.6$) is included in the model. Based on this section, a line fits with an R^2 value of 0.991. This indicates that the cumulative iron release has a linear relationship with the square root of time when the iron release is less than 60% of the total iron loading. From this, we can conclude iron release follows the diffusion model, meaning that the release of iron from PVA iron oxide films is diffusion-controlled.

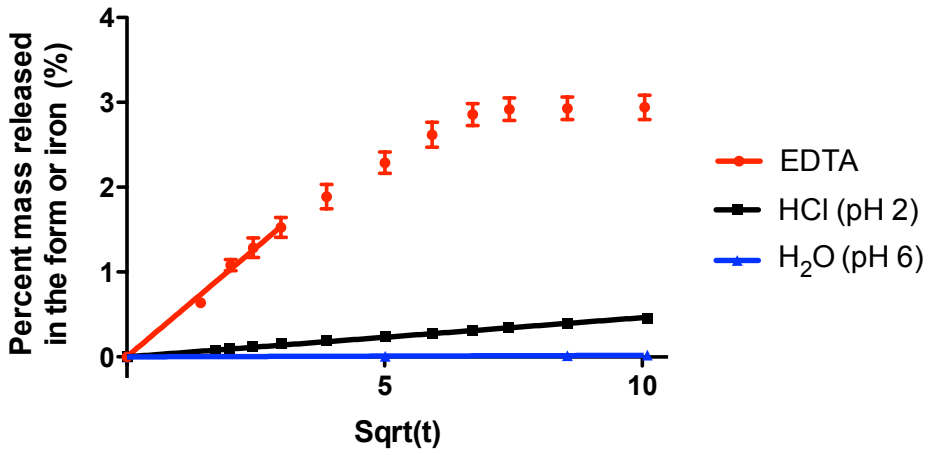

Figure 4.4 Cumulative iron released from PVA iron oxide films (as a percent of initial sample mass) versus the square root of time.

4.3.3 Total mass loss/ film dissolution

We hypothesized that the iron oxide nanoparticles provide some level of crosslinking within the PVA matrix, and the stability of the hydrogel material resulted from a combination of iron oxide crosslinking and crosslinking from the low temperature thermal cycling process. As iron is removed from the sample, the material will begin to fall apart. However, we are unable to determine if degradation, or rather erosion – a physical dissolution and diffusion of a polymer [5], of the material has occurred simply from the iron release results. Release from a degradable matrix can occur through one of three methods: release from physical entrapment as the polymer degrades, release as covalent bonds between the drug and polymer are broken, or diffusion controlled release from physical entrapment followed by delayed polymer degradation [6].

Because we have demonstrated the iron release follows a diffusion-controlled release mechanism, the most likely method of degradation, if it does indeed occur, is the third alternative.

The amount of total hydrogel mass lost in solution over time was measured and compared to plain PVA films containing no iron oxide as control (Figure 4.5). Samples placed in EDTA and HCl solutions were plotted. Both the PVA iron oxide film and plain PVA film samples submerged in water actually increased in mass, due to swelling as the sample rehydrated and reached equilibrium. Because of this, and the low release of iron, the samples in water are not shown. Data for the samples in water can be seen in Appendix V.

As shown in Figure 4.5, the rate of dissolution of the PVA iron oxide material is much greater than that of the control PVA samples. In fact, at 45 days, the total mass loss of PVA iron oxide films is 4.45 and 3.59 times greater than plain PVA films in HCl and EDTA respectively. Similarly, at 73 days, the total mass loss of PVA iron oxide films is 4.08 and 3.41 times greater than PVA films in HCl and EDTA respectively (raw data in Appendix V). The amount of film mass loss over time could be a result of any, or a combination of, the three following effects: iron extraction, osmotic effect, or PVA dissolution.

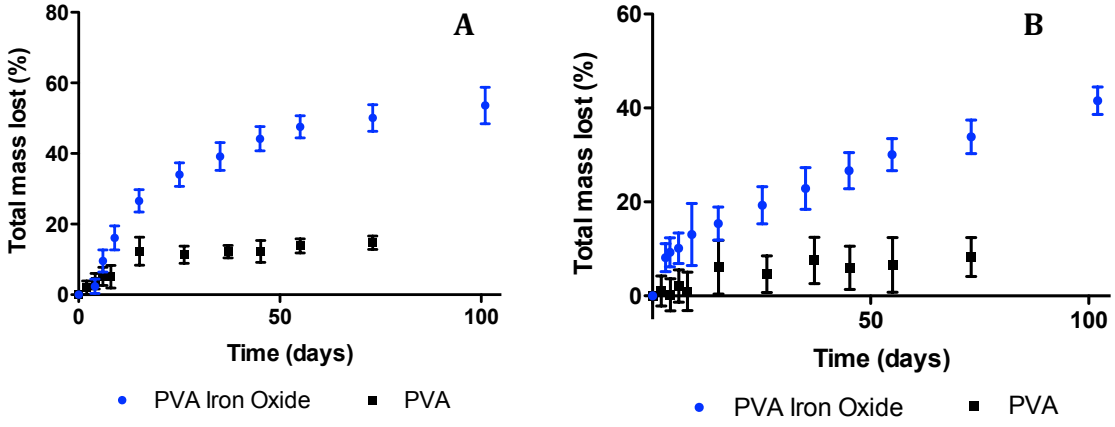

Figure 4.5 Total mass lost from PVA iron oxide films and PVA films (as a percent of initial sample mass) over 100 days in A) EDTA solution B) HCl solution.

First of all, we have demonstrated that the release of iron occurs in the PVA iron oxide films. This contributes to a mass loss of approximately 2.94wt% and 0.45wt% of the initial sample mass in EDTA and HCl respectively. Secondly, in the presence of salts, we expect an osmotic effect to occur and water to be driven out the hydrogel. Results reported by Patachia *et al.* demonstrated an approximate 10% mass loss of PVA hydrogels in 1M salt solutions, and this reached equilibrium after roughly 25 hours. In 3M salt solution, mass loss increased to roughly 40% [7]. This phenomenon likely contributes to some of the mass loss, especially in the initial time points as it reaches equilibrium. However, the concentration of ethylenediametetraacetic acid disodium salt (EDTA) used in our work was 0.05M, much lower than electrolyte concentrations used in work by Patachia *et al.*, and therefore mass loss due water loss through an osmotic effect is expected to be significantly lower. As well, the difference in mass loss shown for PVA iron oxide films relative to control PVA films support the claim that water loss through osmotic effect is not the only other contributing factor. PVA dissolution must account for the remaining mass loss.

Small amounts of PVA dissolution typically occur in PVA hydrogels produced through the LTTC process from the amorphous regions of the hydrogel [8-11]. In our experiment, there is likely to be some dissolution of PVA in both PVA iron oxide films and control PVA films. However, the difference in mass loss for the PVA iron oxide films and control PVA films is significant. The difference between these two samples is the presence of iron oxide, but the difference in mass loss cannot be attributed to solely through loss of iron or loss of water. This indicates that the presence, and subsequent removal, of iron oxide from the film actually affects the degree of PVA dissolution, resulting in much greater PVA dissolution.

4.3.4 Contribution of iron release to film dissolution

An additional comparison can be made by comparing the shape of the curves for iron release and total mass loss (Figure 4.6). When cumulative iron released and total mass lost are plotted together, very similar curves are observed over time. This occurs for films in both the EDTA and HCl solutions. The rates of iron release and total mass loss

are very similar, which clearly demonstrates the effect that iron release has on the dissolution of the entire hydrogel material.

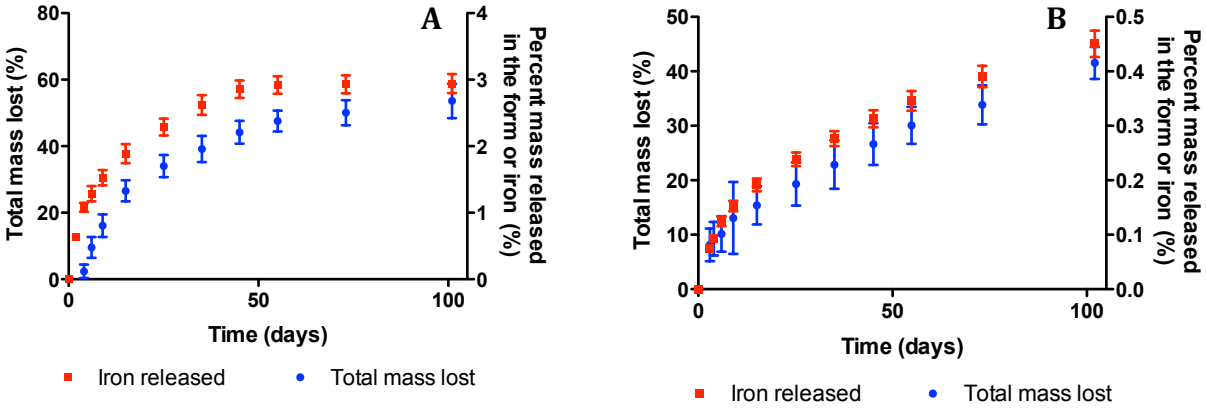

Figure 4.6 Total mass lost and cumulative iron released (both as a percent of initial sample mass) over 100 days in A) EDTA solution, and B) HCl solution. The left hand y-axis displays total mass lost (%) and the right hand y-axis displays cumulative iron released (%).

The total mass loss of PVA iron oxide films after over 100 days in EDTA and HCl are 53.6 ± 5.2%, 41.6 ± 2.9% (Figures 4.5 and 4.6). This is a substantial amount of dissolution, as roughly half of the original sample mass has disappeared. PVA iron oxide film results in a greater extent of dissolution compared to plain PVA film in the presence of low pH and chelating agents. It is difficult to make direct comparisons with work in the literature as samples were prepared using PVA of different molecular weights, solution concentrations, and types of dissolution media [7,9-11]. However, there do not seem to be any reports of PVA hydrogels reaching the extent of dissolution that we have found in this work on PVA containing iron oxide.

4.3.5 Mechanical testing

To confirm that iron oxide takes part in the crosslinking of the hydrogel matrix, and also that the release of iron aids in the material dissolution, mechanical testing was performed on the samples. Figure 4.7 shows stress-strain curves for four different materials: 1) PVA with iron chlorides after 6 FTCs (before iron oxide precipitation); 2)

PVA with iron oxide after 6 FTCs and iron oxide precipitation; 3) PVA with iron oxide after 6 FTCs and after being treated in EDTA for 2 days; and finally, 4) PVA with iron oxide fully after 6 FTCs and after being treated in EDTA for 4 days. Treatment in EDTA was completed because this solution had the most accelerated iron extraction, so would be able to accomplish iron release quickly and demonstrate the effect of iron release on material strength. PVA iron chlorides films (1) was crosslinked only through the low temperature thermal cycling process; PVA iron oxide films (2) was crosslinked through both the LTTC process as well as iron oxide precipitation; and the PVA iron oxide films after treatment in EDTA (3 and 4) were crosslinked through the LTTC process and iron oxide precipitation, and subsequently had iron released into solution for various amounts of time.

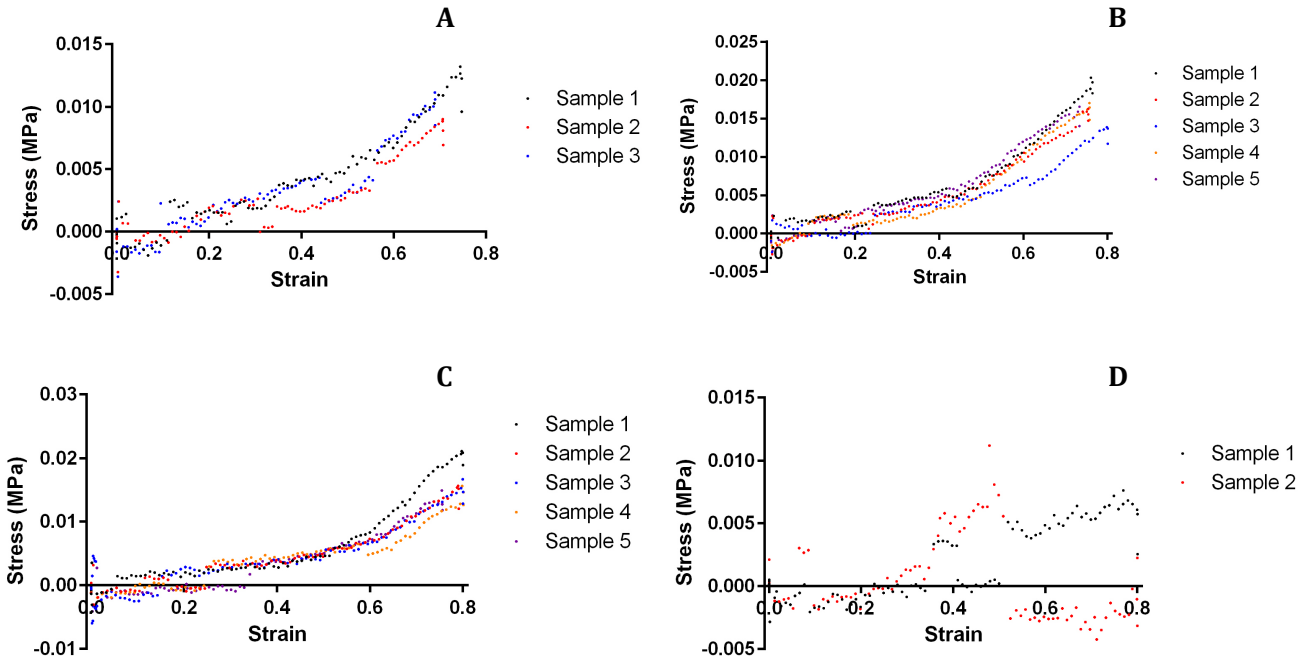

Figure 4.7 Stress-strain curves for four film samples. A) PVA iron chlorides film. B) PVA iron oxide film. C) PVA iron oxide film after EDTA treatment for 2 days. D) PVA iron oxide film after EDTA treatment for 4 days.

Stress-strain data for PVA based materials is non-linear, and several equations have been proposed to model this data [12]. After attempting several different models, a

commonly used exponential model with two fitting parameters (Equation 6) was found to be the best fit for the data present here.

$$\sigma = Aexp(B\varepsilon) \quad (6)$$

The material that was treated in EDTA for 4 days became so weak that three of the samples broke during testing. The two sets of sample data plotted in Figure 4.7D are extremely noisy and random. The material became so weak that it passed the limit that our equipment is accurately able to test. For these reasons, this data was not included in the following comparison.

Figure 4.8 shows the fitted curves for materials shown in Figures 4.7 A, B, and C. The PVA iron chlorides stress-strain curve is the lowest on the graph, meaning it is the weakest material (curve A). After iron oxide precipitation, the stress strain curve increases, indicating that there is a strengthening of the material after the iron chlorides are converted into iron oxide (curve B). This supports the notion that the precipitation of iron oxide within the PVA matrix provides a certain level of crosslinking. The film treated in EDTA for two days has a lower curve in between curves A and B, indicating weakening in the material after iron was released but it was still stronger than the sample with no iron oxide crosslinking (curve C). This confirms that iron removal weakens the material, and is consistent with the dissolution of the material.

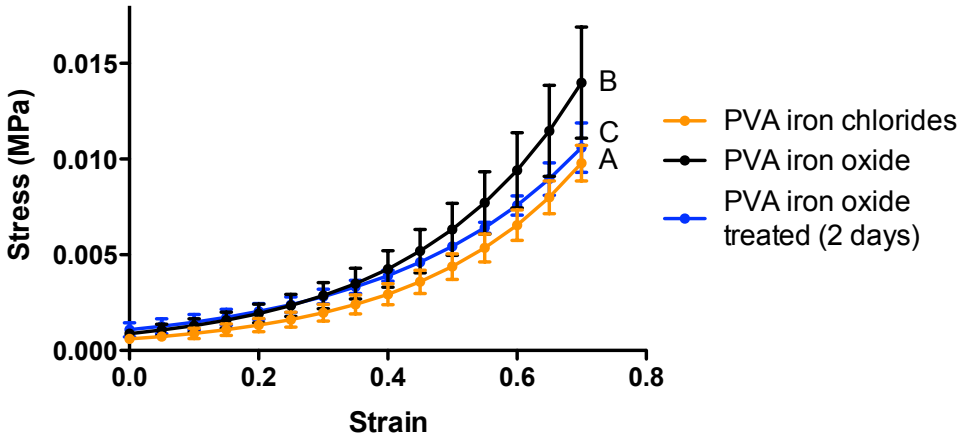

Figure 4.8 Fitted stress-strain curves for PVA iron chloride film, PVA iron oxide film, and PVA iron oxide film after EDTA treatment for 2 days.

A comparison of the elastic modulus of the three materials at a strain of 50% shows a similar trend (Figure 4.9) and there is a significant difference between the elastic modulus of the PVA iron oxide films compared to the PVA iron oxide films after 2 days of treatment in EDTA solution. This indicates that the release of iron into EDTA solution weakens the material significantly, providing further evidence that material dissolution occurs due to the reduction in crosslinking. It is important to note that the EDTA solution used does not represent tissue conditions, and we chose to treat the films in this solution mainly to accelerate the iron release for demonstration of material dissolution.

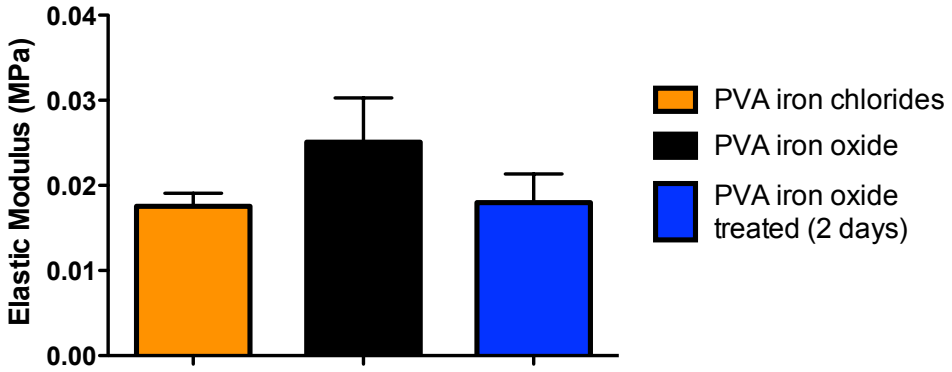

Figure 4.9 Elastic modulus at 50% strain for PVA iron chloride film, PVA iron oxide film, and PVA iron oxide film after EDTA treatment for 2 days.

In this work, 6 FTCs were used to stabilize the film prior to iron oxide precipitation. This is the maximum number of FTCs shown to cause a difference in plain PVA hydrogel crosslinking extent [13,14], although this may be different in PVA containing iron chlorides. We expect that if fewer FTCs were performed on this material, weakening with iron oxide removal would occur at a faster rate. This provides an approach to tune the rate of dissolution of the PVA hydrogels for specific applications.

When we relate the material studied in this section to the microbeads produced in chapter 3, there are a few notable differences. First of all, the geometry is different. Diffusion from a sphere is different from a thin film, so we expect that the rate of iron release, and subsequent material dissolution, would be different. Secondly, precipitation

of iron oxide occurs before low temperature thermal cycling for the microbeads. This provides enough bead stability that 6 FTCs are not required. If only one FTC is used on the beads after iron oxide precipitation, for example, we expect that the dissolution of a bead may occur much quicker, or to a fuller extent, than the film described here. This is promising for application as a 'degradable' multifunctional drug delivery system.

The media that we have performed dissolution in does not perfectly resemble that of physiological tissue. However, we have been able to determine the trends that affect the dissolution of this material. A low pH enhances iron release and material dissolution, as does the presence of chelating agents to extract iron. Tumour tissue has a pH that is slightly lower than that of healthy tissue, sitting at roughly at 6.5 [15]. There are also many natural chelating agents present in the body. Specifically, transferrin, mainly produced in the liver, is a binding protein in the blood that facilitates iron uptake [16]. These types of environmental conditions present in the body may assist in the dissolution of PVA iron oxide material.

4.4 Conclusions

In this chapter, we have produced films using a combination of low temperature thermal cycling and iron oxide precipitation and studied the effect of the two forms of crosslinking together. We were able to demonstrate that iron is released by a diffusion-controlled process from PVA Fe_3O_4 films over time, and this is highly dependent on environmental parameters. A lower pH and presence of chelating agents result in enhanced iron release. Additionally, we have shown that the release of iron from the film corresponds to a total mass loss of the material, and this total mass loss happens to a much greater extent for PVA Fe_3O_4 films compared to plain PVA films. Mechanical testing demonstrated that iron oxide precipitation does strengthen the material, and then subsequent iron release weakens it, resulting in eventual breakage. Overall, we have shown that this PVA iron oxide hydrogel material can 'degrade' over time by a dissolution mechanism in the presence of low pH or through the extraction of iron, which has not been shown for physically crosslinked PVA hydrogels otherwise. This ability to degrade is important for the application of multifunctional visualization and

drug delivery systems as they will degrade rather than accumulate in the body. Material with properties such as this could also find application in other areas, such as tissue engineering, as a dissolvable, magnetically stimulated scaffold material.

References

[1] J. S. Gonzalez, C. E. Hoppe, P. M. Zelis, L. Arciniegas, G. A. Pasquevich, F. H. Sanchez and V. A. Alvarez. 2014. Simple and efficient procedure for the synthesis of ferrogels based on physically cross-linked PVA. *Ind. Eng. Chem. Res.* **53**(1): 214-221.

[2] R. Ricciardi, F. Auriemma, C. Gaillet, C. De Rosa and F. Laupretre. 2004. Investigation of the crystallinity of freeze/thaw poly(vinyl alcohol) hydrogels by different techniques. *Macromolecules* **37**(25): 9510-9516.

[3] R. Ricciardi, F. Auriemma, C. De Rosa and F. Laupretre. 2004. X-ray diffraction analysis of poly(vinyl alcohol) hydrogels, obtained by freezing and thawing techniques. *Macromolecules* **37**(5): 1921-1927.

[4] R.W. Baker and H.K. Lonsdale. 1974. *Controlled release: mechanisms and rates.* Springer.

[5] K. Uhrich, S. Cannizzaro, R. Langer and K. Shakesheff. 1999. Polymeric systems for controlled drug release. *Chem. Rev.* **99**(11): 3181-3198.

[6] W. M. Saltzman. 2001. *Drug delivery: Engineering principles for drug therapy*. Oxford University Press

[7] S. Patachia, A. J. M. Valente and C. Baciu. 2007. Effect of non-associated electrolyte solutions on the behaviour of poly(vinyl alcohol)-based hydrogels. *Eur. Polym. J.* **43**(2): 460-467.

[8] C. Hassan, J. Ward and N. Peppas. 2000. Modeling of crystal dissolution of poly(vinyl alcohol) gels produced by freezing/thawing processes. *Polymer* **41**(18): 6729-6739.

[9] C. Hassan, J. Stewart and N. Peppas. 2000. Diffusional characteristics of freeze/thawed poly(vinyl alcohol) hydrogels: Applications to protein controlled release from multilaminate devices. *Eur. J. Pharm. Biopharm.* **49**(2): 161-165.

[10] C. Hassan and N. Peppas. 2000. Structure and morphology of freeze/thawed PVA hydrogels. *Macromolecules* **33**(7): 2472-2479.

[11] E. Y. L. Wong. 2012. *Poly(vinyl alcohol) nanocomposite hydrogels for intervertebral disc prostheses*. Dissertation/Thesis: The University of Western Ontario.

[12] L. E. Millon. 2006. *Isotropic and anisotropic polyvinyl alcohol based hydrogels for biomedical applications*. Dissertation/Thesis: The University of Western Ontario.

[13] J. L. Holloway, K. L. Spiller, A. M. Lowman and G. R. Palmese. 2011. Analysis of the in vitro swelling behavior of poly(vinyl alcohol) hydrogels in osmotic pressure solution for soft tissue replacement. *Acta Biomater.* **7**(6): 2477-2482.

[14] L. E. Millon and W. K. Wan. 2006. The polyvinyl alcohol-bacterial cellulose system as a new nanocomposite for biomedical applications. *J. Biomed. Mater. Res. B* **79**(2): 245-253.

[15] K. Zhou, Y. Wang, X. Huang, K. Luby-Phelps, B. D. Sumer and J. Gao. 2011. Tunable, ultrasensitive pH-responsive nanoparticles targeting specifc endocytic organelles in living cells. *Angew Chem Int Edit*. **50**(27): 6109-6114.

[16] K. Thorstensen and I. Romslo. 1990. The role of transferrin in the mechanism of cellular iron uptake. *Biochem. J.* **271**(1): 1-10.

CHAPTER 5 – Conclusions and Future Goals

There is a constant need to improve treatment of cancer as it remains a highly prevalent and deadly illness. For loco-regional treatment of liver cancer tumours, the use of drug-eluting embolization microbeads is a very promising treatment. However, areas of improvement have been identified, and work to enhance the products used for this treatment could translate into a better understanding of the treatment as well as improved patient outcomes. We have identified several main design criteria for a novel multifunctional 'nano-on-micro' visualization and delivery system that incorporates improvements to current systems, and we attempted to address these through the work presented in this thesis.

We have demonstrated the production of PVA iron oxide CNC microbeads that can be visualized with CT, have magnetic properties which could allow magnetic localization, have the potential to be loaded with therapeutics, and are composed of a material that we have shown to 'degrade' over time. This multifunctional system has many desirable properties that make it a good candidate for use in TACE or other contrast enhancement and drug delivery applications.

There are several directions that this work can follow moving into the future. We would like to see these microbeads visualized with MRI, as the presence of magnetite nanoparticles lends itself well to this type of imaging. As well, we would like to explore, in detail, the drug loading and release mechanisms of this system with doxorubicin. It would also be interesting and valuable to explore the magnetic localization capability of these microbeads. Additionally, the dissolution study performed on the bulk hydrogel material should be compared to dissolution of the microbeads themselves. Finally, in terms of application, researching the use of these microbeads in animal models would be a logical step to determine their viability as a visible drug-eluting embolization system.

Indeed, the work that we have completed here demonstrates the production of a promising system that should be further studied for use as a multifunctional visualization and drug delivery system.

APPENDICES

Appendix I – Bacterial Cellulose Growth and Harvest Procedure

The bacterial cellulose (BC) was grown in a static culture with media consisting of 0.22M fructose, 26.63mM ammonium sulphate, 7.34mM monobasic potassium phosphate, 1.01mM magnesium sulphate heptahydrate, 14.28mM tri-sodium citrate, 45.80mM citric acid and 5g/L yeast extract. 200mL of media were placed in 500mL Erlenmeyer flasks, autoclaved for 30 minutes, inoculated with *G. xylinus* (BPR 2001) bacteria that was cultivated in our lab, and sealed with glass wool and tinfoil. The flasks were stored in an incubator at room temperature for 3 weeks before extracting the cellulose. The cellulose pellicles that formed were removed from the flasks and blended with water using a Commercial Laboratory Blender (51BL30). The mixture was centrifuged at room temperature at 15,000 rpm for 5 minutes (Sorvall Refrigerated Superspeed Centrifuge; model RC-5B & RC-5C), and the collected sample was re-suspended in a 1w/v% NaOH solution for 3 hours at 80°C to remove any remaining bacterial cells. The mixture was again centrifuged, collected and re-suspended in water and this was repeated three times for adequate washing. The resulting cellulose was stored at 4°C.

Appendix II – Standard XRD Pattern for Magnetite

Corresponding to ICCD card number 00-019-0629

00-019-0629 Apr 16, 2015 2:07 PM (Owner)

Status Primary **QM:** Star **Pressure/Temperature:** Ambient **Chemical Formula:** Fe +2 Fe2 +3 O4
Empirical Formula: Fe3 O4 **Weight %:** Fe72.36 O27.64 **Atomic %:** Fe42.86 O57.14
Compound Name: Iron Oxide **Mineral Name:** Magnetite, syn

Radiation: CuKá1 : 1.5406 Å **Filter:** Ni Beta **Intensity:** Diffractometer **I/Ic:** 4.9

SYS: Cubic **SPGR:** Fd-3m (227)
Author's Cell [AuthCell a: 8.396 Å **AuthCell Vol:** 591.86 Å³ **AuthCell Z:** 8.00 **AuthCell MolVol:** 73.98]
Density [Dcalc: 5.197 g/cm³ **Dmeas:** 5.176 g/cm³] **SS/FOM:** F(26) = 59.2(0.0129, 34)
Temp: 298.000 K (Author provided temperature) **Color:** Black

Space Group: Fd-3m (227) **Molecular Weight:** 231.54
Crystal Data [XtlCell a: 8.396 Å **XtlCell b:** 8.396 Å **XtlCell c:** 8.396 Å **XtlCell :** 90.00° **XtlCell :** 90.00°
XtlCell : 90.00° **XtlCell Vol:** 591.86 Å³ **XtlCell Z:** 8.00]
Crystal Data Axial Ratio [a/b: 1.000 **c/b:** 1.000]
Reduced Cell [RedCell a: 5.937 Å **RedCell b:** 5.937 Å **RedCell c:** 5.937 Å **RedCell :** 60.00°
RedCell : 60.00° **RedCell :** 60.00° **RedCell Vol:** 147.96 Å³]

: =2.42

Atomic parameters are cross-referenced from PDF entry 04-008-8145 **ADP Type:** B **Origin:** O2
Crystal (Symmetry Allowed): Centrosymmetric

SG Symmetry Operators:

Seq	Operator	Seq	Operator	Seq	Operator	Seq	Operator	Seq	Operator
1	x,y,z	11	z,-x+1/4,-y+1/4	21	-y+1/4,z,-x+1/4	31	-x+1/4,-z+1/4,y	41	z,y,x
2	-x,-y,-z	12	-z,x+3/4,y+3/4	22	y+3/4,-z,x+3/4	32	x+3/4,z+3/4,-y	42	-z,-y,-x
3	x,-y+1/4,-z+1/4	13	-z+1/4,x,-y+1/4	23	-y+1/4,-z+1/4,x	33	y,x,z	43	z,-y+1/4,-x+1/4
4	-x,y+3/4,z+3/4	14	z+3/4,-x,y+3/4	24	y+3/4,z+3/4,-x	34	-y,-x,-z	44	-z,y+3/4,x+3/4
5	-x+1/4,y,-z+1/4	15	-z+1/4,-x+1/4,y	25	x,z,y	35	y,-x+1/4,-z+1/4	45	-z+1/4,y,-x+1/4
6	x+3/4,-y,z+3/4	16	z+3/4,x+3/4,-y	26	-x,-z,-y	36	-y,x+3/4,z+3/4	46	z+3/4,-y,x+3/4
7	-x+1/4,-y+1/4,z	17	y,z,x	27	x,-z+1/4,-y+1/4	37	-y+1/4,x,-z+1/4	47	-z+1/4,-y+1/4,x
8	x+3/4,y+3/4,-z	18	-y,-z,-x	28	-x,z+3/4,y+3/4	38	y+3/4,-x,z+3/4	48	z+3/4,y+3/4,-x
9	z,x,y	19	y,-z+1/4,-x+1/4	29	-x+1/4,z,-y+1/4	39	-y+1/4,-x+1/4,z		
10	-z,-x,-y	20	-y,z+3/4,x+3/4	30	x+3/4,-z,y+3/4	40	y+3/4,x+3/4,-z		

Atomic Coordinates:

Atom	Num	Wyckoff	Symmetry	x	y	z	SOF	Biso	AET
Fe	1	8a	-43m	0.125	0.125	0.125	1.0	0.61765	4-a
Fe	2	16d	.-3m	0.5	0.5	0.5	1.0	0.70188	6-a
O	3	32e	.3m	0.255	0.255	0.255	1.0	0.72995	4-a

Anisotropic Displacement Parameters:

Atom	Num	Bani11	Bani22	Bani33	Bani12	Bani13	Bani23
Fe	1	0.617656	0.617656	0.617656	0.0	0.0	0.0
Fe	2	0.701882	0.701882	0.701882	0.0280753	0.0280753	0.0280753
O	3	0.729958	0.729958	0.729958	0.0280753	0.0280753	0.0280753

Subfile(s): Common Phase, Educational Pattern, Forensic, Inorganic, Metals & Alloys, Micro & Mesoporous, Mineral Related (Mineral , Synthetic), NBS Pattern, Pigment/Dye

Prototype Structure: Mg Al2 O4 **Prototype Structure [Alpha Order]:** Al2 Mg O4
Mineral Classification: Spinel (Supergroup), 1C-oxide (Group) **Pearson:** cF56.00

00-019-0629 Apr 16, 2015 2:07 PM (Owner)

Cross-Ref PDF #'s: 00-011-0614 (Deleted), 00-026-1136 (Primary), 01-072-2303 (Alternate), 01-074-1909 (Alternate), 01-075-0449 (Alternate), 01-075-1610 (Alternate), 01-076-1849 (Alternate), 04-001-7822 (Alternate), 04-001-7909 (Alternate), 04-001-9000 (Alternate), 04-001-9326 (Alternate), 04-002-0264 (Alternate), 04-002-0618 (Alternate), 04-002-0643 (Alternate), 04-002-1855 (Alternate), 04-002-2487 (Alternate), 04-002-2707 (Alternate), 04-002-2709 (Alternate), 04-002-2981 (Alternate), 04-002-3194 (Alternate), 04-002-3668 (Alternate), 04-002-5310 (Alternate), 04-002-5448 (Alternate), 04-002-5632 (Alternate), 04-002-5683 (Alternate), 04-002-5903 (Alternate), 04-002-6866 (Alternate), 04-002-6955 (Alternate), 04-002-8141 (Alternate), 04-002-8629 (Alternate), 04-002-9019 (Alternate), 04-002-9635 (Alternate), 04-003-1446 (Alternate), 04-004-2838 (Alternate), 04-005-4307 (Alternate), 04-005-4319 (Primary), 04-005-4551 (Alternate), 04-005-5733 (Alternate), 04-005-6268 (Alternate), 04-005-9786 (Alternate), 04-005-9788 (Alternate), 04-005-9815 (Alternate), 04-006-0225 (Alternate), 04-006-0425 (Alternate), 04-006-1668 (Alternate), 04-006-2406 (Alternate), 04-006-2467 (Alternate), 04-006-2752 (Alternate), 04-006-6497 (Alternate), 04-006-6550 (Alternate), 04-006-6692 (Alternate), 04-006-8076 (Alternate), 04-007-1427 (Alternate), 04-007-2718 (Alternate), 04-007-6010 (Alternate), 04-007-8567 (Alternate), 04-007-8976 (Alternate), 04-007-9093 (Alternate), 04-008-0315 (Alternate), 04-008-0777 (Alternate), 04-008-4423 (Alternate), 04-008-4511 (Alternate), 04-008-4512 (Alternate), 04-008-8145 (Alternate), 04-009-4225 (Alternate), 04-009-8417 (Alternate), 04-009-8418 (Alternate), 04-009-8419 (Alternate), 04-009-8420 (Alternate), 04-009-8421 (Alternate), 04-009-8422 (Alternate), 04-009-8423 (Alternate), 04-009-8424 (Alternate), 04-009-8425 (Alternate), 04-009-8426 (Alternate), 04-009-8427 (Alternate), 04-009-8428 (Alternate), 04-009-8429 (Alternate), 04-009-8430 (Alternate), 04-009-8431 (Alternate), 04-009-8435 (Alternate), 04-009-8436 (Alternate), 04-009-8437 (Alternate), 04-009-8438 (Alternate), 04-009-8439 (Alternate), 04-009-8440 (Alternate), 04-011-5952 (Alternate)

Entry Date: 09/01/1969

References:

Type	DOI	Reference
Primary Reference		Natl. Bur. Stand. (U. S.) Monogr. 25 5, 31 (1967).
Crystal Structure		Crystal Structure Source: LPF.
Optical Data		Dana's System of Mineralogy, 7th Ed. I, 698.

Database Comments: Additional Patterns: To replace 00-011-0614. See 00-026-1136. See 20596 (PDF 01-072-2303); 27898 (PDF 01-074-1909); 29129 (PDF 01-075-0449); 31157 (PDF 01-075-1610); 36314 (PDF 01-076-1849); 30860 (PDF 01-075-1372); 65338 (PDF 01-079-0416); 65339 (PDF 01-079-0417); 65340 (PDF 01-079-0418); 65341 (PDF 01-079-0419); 68181 (PDF 01-080-0389); 68182 (PDF 01-080-0390) and 75627 (PDF 01-082-1533). Analysis: Spectrographic analysis showed the following major impurities: 0.01 to 0.1% Co, 0.001 to 0.01% Ag, Al, Mg, Mn, Mo, Ni, Si, Ti and Zn. Color: Black. General Comments: Other data 00-025-1376. Opaque Optical Data: Opaque mineral optical data on specimen from Braastad, Norway: RR2Re=20.1, Disp.=16, VHN100=592, Color values=.311, .314,. Sample Source or Locality: Sample obtained from the Columbian Carbon Co., New York, NY, USA. Temperature of Data Collection: Pattern taken at 298 K. Unit Cell: a=8.3967 refined in 1975. Unit Cell Data Source: Powder Diffraction.

d-Spacings (21) - 00-019-0629 (Fixed Slit Intensity) - Co K1 1.78896 Å

2 (°)	d (Å)	I	h	k	l	*	2 (°)	d (Å)	I	h	k	l	*	2 (°)	d (Å)	I	h	k	l	*
21.2468	4.852000	8	1	1	1		74.1050	**1.484500**	40	4	4	0		109.8442	1.093000	12	7	3	1	
35.0926	**2.967000**	30	2	2	0		78.1402	1.419200	2	5	3	1		116.9058	1.049600	6	8	0	0	
41.3749	**2.532000**	100	3	1	1		84.7076	1.327700	4	6	2	0		129.3458	0.989600	2	6	6	0	
43.3035	2.424300	8	2	2	2		88.6024	1.280700	10	5	3	3		134.6243	0.969500	6	7	5	1	
50.4387	2.099300	20	4	0	0		89.9173	1.265900	4	6	2	2		136.4521	0.963200	4	6	6	2	
62.8906	1.714600	10	4	2	2		95.1364	1.211900	2	4	4	4		144.6488	0.938800	4	8	4	0	
67.2264	1.615800	30	5	1	1		105.7173	1.122100	4	6	4	2		175.4038	0.895200	2	6	6	4	

Appendix III – Alternative Microfluidic Device Designs

Three designs that tested for microbead production are shown in Table 1.

Table 1. Microchannel device designs for production of PVA iron oxide CNC microbeads

Design	1. T-junction	2. Modified T-junction	3. Flow-focusing
Figure	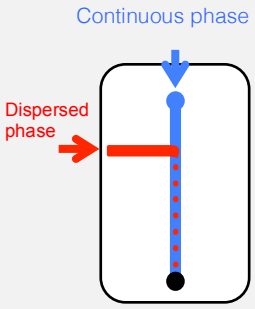 Red channel width is 127µm. Blue channel width is 500µm.	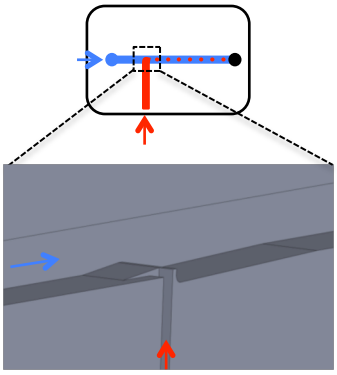 Red channel width is 127µm. Blue channel width is 500µm.	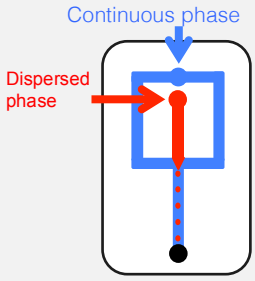 Red channel width is 200µm with a narrow section of 127µm. Blue channels have a width of 500µm.
Description	Dispersed phase (PVA iron phase) flows perpendicular to the continuous phase (oil phase), meeting at a T-junction.	Dispersed phase (PVA iron phase) flows perpendicular to the continuous phase (oil phase), meeting at a T-junction with a raised notch to improve shearing of the microbead from the wall.	Dispersed phase (PVA iron phase) flow is directed through a channel by the continuous phase (oil phase) flowing from two directions.

The initial T-junction design resulted in the formation of slugs – elongated droplets – of the dispersed phase. Quite rapidly, this transformed into a stream of the dispersed phase flowing along the side of the microchannel, parallel to the oil phase. Beads could not be produced this way, but instead a constant stream of the dispersed phase solution resulted. The modified T-junction design allowed for production of microbeads. Images of the dispersed phase flowing against a continuous phase in the modified T-junction design are shown in Figure 1 and 2. Initially, fully formed beads were

produced (Figure 1), followed quickly by bead slugging (Figure 2). An additional issue associated with the use of this design was the size limit that existed. The large channel was 500µm in width, and even with a change in the flow rates, beads filled the entire channel (Figure 3.4). This was not able to produce beads of the desired particle size. The flow-focusing design was successful for microbead production.

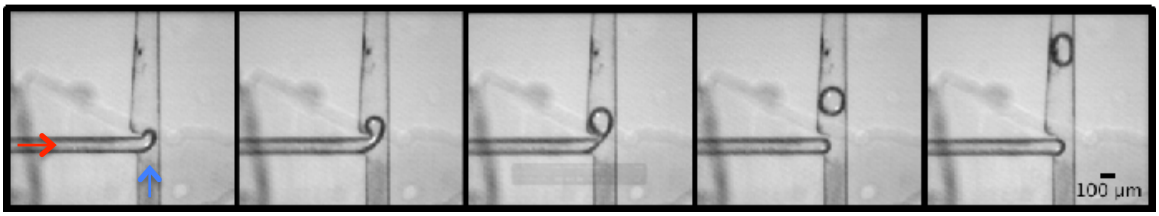

Figure 1. Microbead production using modified T-junction microchannel. The red arrow indicates the PVA iron phase flow and the blue arrow indicates the oil phase flow.

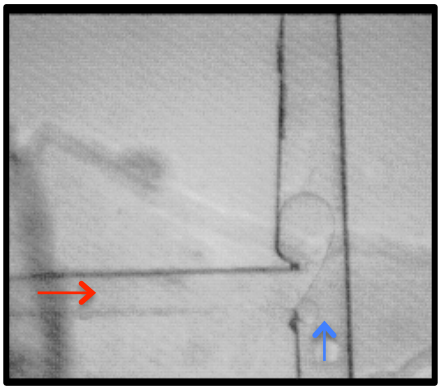

Figure 2. Microbead slugging in modified T-junction microchannel. The red arrow indicates the PVA iron phase flow and the blue arrow indicates the oil phase flow.

Appendix IV – Iron oxide nanoparticle size measurement

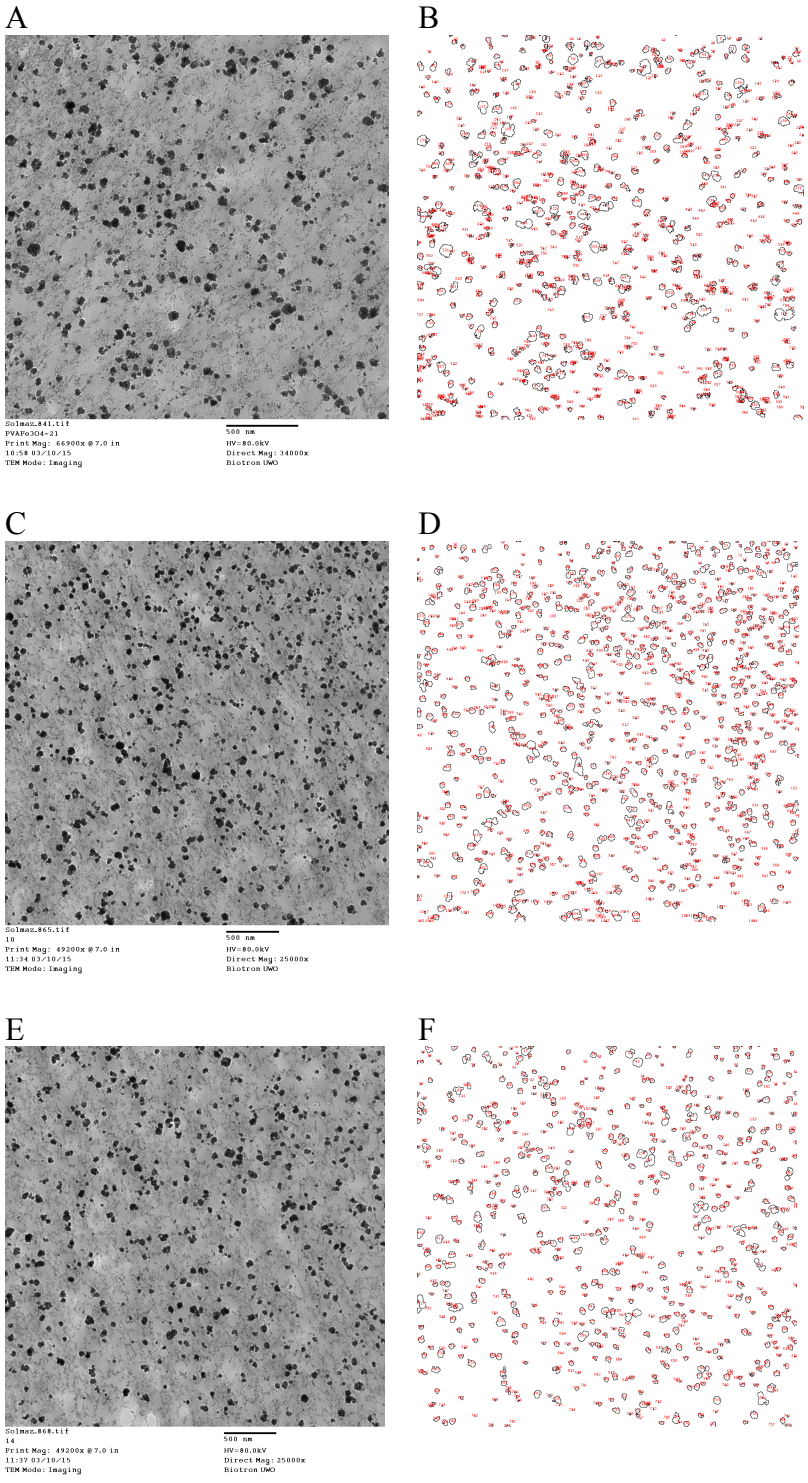

Figure 1. A,C,E) TEM images of iron oxide nanoparticles in PVA matrix. B,D,F) Corresponding outlines of particles analyzed by Image J particle analyzer with threshold set between 0-80.

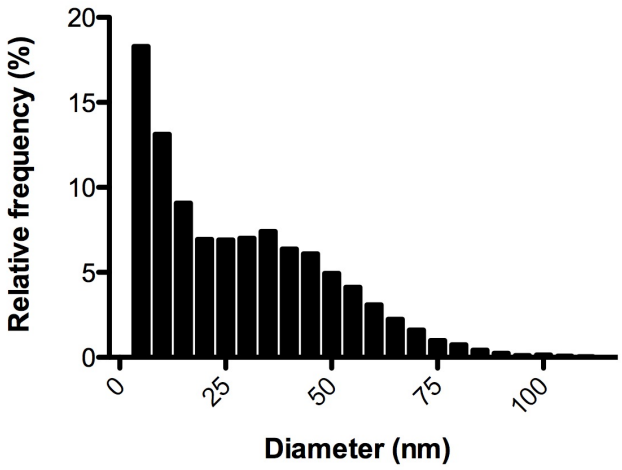

Figure 2. Histogram of equivalent spherical diameter of iron oxide nanoparticles in PVA matrix from TEM images.

Appendix V – Data for Iron Release and Mass Loss From PVA Iron Oxide Films

Table 1. Cumulative iron released from PVA iron oxide films as a percent of initial sample mass in EDTA solution

Time (days)	Average Fe release (%)	Standard deviation (%)
0	0	0
2.05	0.637	0.040
4.07	1.081	0.067
6.02	1.287	0.114
8.94	1.527	0.116
15.01	1.889	0.143
25.06	2.289	0.127
35.12	2.619	0.148
45.06	2.856	0.131
55.06	2.920	0.132
73.07	2.930	0.134
100.99	2.941	0.144

Table 2. Cumulative iron released from PVA iron oxide films as a percent of initial sample mass into HCl solution

Time (days)	Average Fe release (%)	Standard deviation (%)
0	0	0
3	0.074	0.006
4.00	0.093	0.006
6.00	0.124	0.009
9	0.153	0.010
15.07	0.192	0.012
25.16	0.239	0.013
35.06	0.276	0.014
45.07	0.313	0.016
54.91	0.346	0.018
73.09	0.391	0.020
102.03	0.451	0.024

Table 3. Cumulative iron released from PVA iron oxide films as a percent of initial sample mass into H_2O

Time (days)	Average Fe release (%)	Standard deviation (%)
0	0	0
25.13	0.008	0.001
73.05	0.014	0.002
101.98	0.020	0.003

Table 4. Mass lost of PVA iron oxide films in EDTA solution as percent of initial sample mass

PVA Iron Oxide			PVA		
Time (days)	**Average percent loss (%)**	**Standard deviation (%)**	**Time (days)**	**Average percent loss (%)**	**Standard deviation (%)**
0	0	0	0	0	0
2.05	-10.442	3.823	2.001	1.943	1.932
4.07	2.388	2.043	4.088	3.857	2.206
6.02	9.549	3.126	6.066	5.203	2.586
8.94	16.115	3.400	8.007	5.123	3.209
15.01	26.593	3.182	15.128	12.329	3.966
25.06	34.043	3.332	26.212	11.328	2.417
35.12	39.165	3.913	37.139	12.220	1.764
45.06	44.168	3.433	45.219	12.266	3.086
55.06	47.573	3.113	55.059	13.840	1.992
73.07	50.083	3.755	73.080	14.738	1.879
100.99	53.609	5.151			

Table 5. Mass lost of PVA iron oxide films in HCl solution as percent of initial sample mass

PVA Iron Oxide			PVA		
Time (days)	**Average percent loss (%)**	**Standard deviation (%)**	**Time (days)**	**Average percent loss (%)**	**Standard deviation (%)**
0.00	0.000	0.000	0.000	0.000	0.000
3.00	8.137	2.989	2.005	1.054	3.204
4.00	9.266	3.088	4.090	0.230	3.410
6.00	10.142	3.252	6.066	2.084	3.452
9.00	13.069	6.604	8.009	0.937	4.085
15.07	15.394	3.508	15.132	6.100	5.695
25.16	19.305	3.950	26.212	4.616	3.896
35.06	22.874	4.420	37.139	7.543	4.931
45.07	26.660	3.836	45.219	5.957	4.614
54.91	30.069	3.396	55.063	6.607	5.815
73.09	33.866	3.579	73.083	8.278	4.160
102.03	41.553	2.944			

Table 6. Mass lost of PVA iron oxide films in H_2O solution as percent of initial sample mass

PVA Iron Oxide			PVA		
Time (days)	**Average percent loss (%)**	**Standard deviation (%)**	**Time (days)**	**Average percent loss (%)**	**Standard deviation (%)**
0.00	0.000	0.000	0.000	0.000	0.000
25.13	-39.168	4.181	26.214	-9.508	4.540
73.05	-45.040	2.882	73.083	-3.849	3.977
101.98	-31.708	6.828			

Curriculum Vitae

A. Dawn Bannerman

UNIVERSITY EDUCATIONAL BACKGROUND

2013 - 2015 **Master of Engineering Science** (Candidate)
Biomedical Engineering Graduate Program
The University of Western Ontario, London, Ontario, Canada
Supervisor: Dr. Wankei Wan

2008 - 2012 **Bachelor of Engineering Science**
Biochemical Engineering
The University of Western Ontario, London, Ontario, Canada

SCHOLARSHIPS, HONOURS AND AWARDS

Dec. 2014 **Western Science Interdisciplinary Research Showcase: Materials and Biomaterials 2nd place award**
Institutional

May. 2014 **Ontario Graduate Scholarship QEII – Masters**
Provincial

Sept. 2013 **NSERC CGS Scholarship – Masters**
National

Apr. 2012 **Undergraduate Fourth Year Thesis 2nd prize**
Institutional

Nov. 2011 **Philip Nakahara MacLachlan Memorial Award**
Institutional

2012, 2011, 2009 **Dean's Honor List**
Institutional

2008 - 2012 **Continuing Scholarship**
Institutional

Sept. 2008 **Ontario Professional Engineers Foundation for Education Entrance Scholarships**
Institutional

PUBLICATIONS and PRESENTATIONS

A. Publications (1)

1. W. Wan, D. Bannerman, L. Yang, H. Mak. "Poly(Vinyl Alcohol) Cryogels for Biomedical Applications." Polymeric Cryogels. *Advances in Polymer Science. Vol 263.* Ed. O. Okay. (June 2014).

B. Poster Presentations (5) **presenter*

1. D. Bannerman*, J. Liu, W. Wan. A nano-on-micro degradable drug delivery system. Western Science Interdisciplinary Research Showcase. University of Western Ontario, London. (Dec. 2, 2014).

2. D. Bannerman*, J. Liu, W. Wan. A 'degradable' poly(vinyl alcohol) hydrogel. Canadian Biomaterials Society Meeting, Halifax, Nova Scotia. (June 4-7, 2014).

3. D. Bannerman*, A. Gholami, D. Small, W.K. Wan. Nano-on-Micro Bead Delivery System to Target Liver Cancer. London Health Research Day Conference, London, Ontario. (March 19, 2013).

4. D. Bannerman, A. Gholami*, D. Small, W.K. Wan. A Nano-on-Micro Bacterial Cellulose-Poly(vinyl alcohol) Delivery System for Therapeutics. Canadian Materials Science Conference, London, Ontario (June 6, 2012).

5. D. Bannerman*, A. Gholami, D. Small, W.K. Wan. A Nano-on-Micro Bacterial Cellulose-Polyvinyl(alcohol) Delivery System for Therapeutics. London Health Research Day Conference, London, Ontario (March 20, 2012).

TEACHING EXPERIENCE

Sept. 2014 – Dec. 2014 **Graduate Teaching Assistant**
Green Organic Chemistry
Department of Chemical and Biochemical Engineering
The University of Western Ontario, London, Ontario

Jan. 2014 – Apr. 2014 **Graduate Teaching Assistant**
Advanced Biomaterials Engineering
Biomedical Engineering Graduate Program and Department of Chemical and Biochemical Engineering
The University of Western Ontario, London, Ontario

Sept. 2013 – Apr. 2014 **Teaching Assistant**
Business for Engineers
The University of Western Ontario, London, Ontario

Sept. 2013 – Dec. 2013 **Graduate Teaching Assistant**
Green Organic Chemistry
Department of Chemical and Biochemical Engineering
The University of Western Ontario, London, Ontario

PROFESSIONAL MEMBERSHIPS

2014 **Canadian Biomaterials Society**
Student member